SELF-INDUCED FLAVOR CONVERSION OF SUPERNOVA NEUTRINOS:

Introducing a new approach

Ignacio Izaguirre

München 2017

Self-induced flavor conversion of supernova neutrinos:

Introducing a new approach

Dissertation
an der Fakultät für Physik
der Ludwig–Maximilians–Universität
München

vorgelegt von
Ignacio Izaguirre
aus Madrid

München, den 30.05.2017

Dissertation

an der Fakultät für Physik
der Ludwig-Maximilians-Universität München
vorgelegt von Ignacio Izaguirre
aus Madrid am 30. Mai 2017.

Erstgutachter: Dr. habil. Georg Raffelt

Zweitgutachter: Prof. Dr. Gerhard Buchalla

Tag der mündlichen Prüfung: 4. Juli 2017

Max-Planck-Institut für Physik,
München, den 30. Mai 2017.

Zusammenfassung

In der vorliegenden Dissertation untersuchen wir selbst-induzierte Neutrinooszillationen in Umgebungen hoher Neutrinodichte. In diesem Zusammenhang sind Kern-Kollaps-Supernovae das geeignetste Beispiel. Wir untersuchen die Entwicklung der Molekularstärke (mean field) des Neutrino-Flavors. Dazu verwenden wir den Dichtematrizen-Formalismus. Unter der Verwendung der linearisierten Bewegungsgleichungen führen wir eine multidimensionale Fouriertransformation durch, um eine Dispersionrelation für die Wellenzahl ($\mathbf{K}$) und Frequenz (Ω) der dynamischen kollektiven Flavormoden zu erhalten. Wir wenden diesen neuen Ansatz an, um die zeitliche und räumliche Flavor-Entwicklung der Neutrino-Feldstärke in Supernova-ähnlichen Szenarien zu untersuchen. Wir folgern, dass exponentiell wachsende Lösungen (Instabilitäten) "verbotenen" Regionen bzw. Lücken in der ($\mathbf{K}$, Ω)-Ebene der Dispersionsrelation entsprechen. Falls die Anfangsbedingungen des Systems eine Frequenz im Bereich einer solchen Lücke vorgeben, wird das System einem exponentiellen räumlichen Wachstum unterliegen. Analoges gilt für das zeitliche Wachstum, falls die Anfangsbedingungen einen Wellenvektor im Bereich einer Lücke vorgeben. Für den speziellen Fall der räumlichen Entwicklung eines stationären Systems folgern wir, dass Inhomogenitäten senkrecht zur Richtung des Wellenvektors keine Auswirkungen haben. Darüberhinaus kann die Flavor-Konversionsrate abhängig von der lokalen Winkelverteilung der von Neutrinos getragenen Elektronenleptonzahl proportional zur Neutrino-Neutrino-Wechselwirkungsenergie, gegeben durch $\mu = \sqrt{2}G_{\mathrm{F}}n_{\nu}$, sein. Letztere ist in Umgebungen hoher Neutrinodichte deutlich höher als die Vakuumoszillationsenergie, $\varpi = \Delta m^2/2E$, d.h. $\mu \gg \varpi$. Wir bezeichnen dieses Phänomen als schnelle Flavor-Konversion, die selbst bei verschwindendem ϖ auftritt. Abschließend halten wir fest, dass die Lösungen realer Szenarien von den Randbedingungen und/oder den Anfangsbedingungen abhängen; eine Fragestellung, die weiterführende Untersuchungen erfordert.

Resumen

En la presente tesis estudiamos las oscilaciones colectivas auto-inducidas en ambientes con una alta densidade de neutrinos. En este contexto, las supernovas son el ejemplo más ilustrativo. Bajo el marco proporcionado por el formalismo de la matriz de densidad, estudiamos la evolución del campo medio del flavor de los neutrinos. Usando las ecuaciones linearizadas de movimiento, llevamos a cabo una transformada de Fourier multidimensional que nos lleva a una relación de dispersión para el número de onda ($\mathbf{K}$) y la frecuencia (Ω) de los modos dinámicos de flavor colectivo. Utilizamos este nuevo enfoque para estudiar la evolución espacial y temporal del flavor del campo de neutrinos en escenarios que simulan las condiciones presenstes en supernovas. Concluimos que las soluciones run-away (inestables) corresponden a regiones "prohibidas" o huecos en la relación de dispersión en el plano ($\mathbf{K}$, Ω). Si las condiciones iniciales del sistema imponen una frecuencia dentro de la zona prohibida, el sistema experimentará un crecimiento exponencial en su evolución espacial. Por otro lado, si las condiciones iniciales del sistema imponen un vector de onda dentro de la región prohibida, el sistema sufriráun crecimiento exponencial en su evolución temporal. Para el caso particular de la evolución espacial de un sistema estacionario, concluimos que las inhomogeneidades en las direcciones perpendiculares a la dirección de propagación son inofensivas. Además, dependiendo de las distribuciones angulares locales del número de electrones transportado por los neutrinos, la tasa de conversión del flavor puede ser proporcional al energía de interacción entre los neutrinos, $\mu = \sqrt{2}G_{\rm F}n_\nu$, que es mucho mayor que la energía de oscilación de vacío ($\varpi = \Delta m^2/2E$) en estos ambientes densos ($\mu \gg \varpi$). Nos referimos a este fenómeno como la conversión rápida de flavor, y se produce incluso para el límite ϖ tendiendo a cero. Finalmente, señalamos que las soluciones que tienen lugar en un escenario real dependen de las condiciones de contorno y/o condiciones iniciales, un tema que requiere más estudio.

Abstract

In this thesis, we study self-induced neutrino flavor conversion in environments where neutrinos are dense. In this context, core-collapse supernovae are the most illustrative examples. Under the framework provided by the density matrix formalism, we study the evolution of the mean field of the neutrino flavor. Using the linearized equations of motion, we carry out a multidimensional Fourier transform which leads us to a dispersion relation for the wave number ($\mathbf{K}$) and frequency (Ω) of the dynamical collective flavor modes. We use this novel approach to study the spatial and temporal flavor evolution of the neutrino field in supernova motivated scenarios. We conclude that run-away solutions (instabilities) correspond to "forbidden" regions or gaps in the dispersion relation in the ($\mathbf{K}$,Ω) plane. If the initial conditions of the system impose a frequency within the gap, the system will undergo spatial exponential growth. On the other hand, if the initial conditions of the system impose a wave vector within the gap, the system will undergo a temporal run away. For the particular case of the spatial evolution of a stationary system, we conclude that inhomogeneities in the perpendicular directions are innocuous. Moreover, depending on the local angular distributions of the electron number carried by neutrinos, the flavor conversion rate can be proportional to the neutrino-neutrino interaction energy $\mu = \sqrt{2}G_{\rm F}n_{\nu}$, which is much higher than the vacuum oscillation energy $\varpi = \Delta m^2/2E$ in these dense environments $\mu \gg \varpi$. We refer to this phenomenon as fast flavor conversion which occurs even for vanishing ϖ. Finally, we point out that the actual solutions which take place in a real scenario depend on the boundary conditions and/or initial conditions, a topic which requires further study.

Acronyms

- **SM**: Standard model
- **CC**: charged current
- **NC**: neutral current
- **SN**: supernova
- **LESA**: lepton-emission self sustained asymmetry
- **SASI**: Standing Accretion Shock Instability
- **ELN**: electron lepton number
- **MA**: multi-angle
- **MAA**: multi-azimuthal-angle
- **MZA**: multi-zenith-angle

List of Publications

During my PhD, I have worked on different topics. This thesis is mainly based on the work presented in the following publications:

[1] S. Chakraborty, R. S. Hansen, I. Izaguirre and G. Raffelt, "*Self-induced flavor conversion of supernova neutrinos on small scales*," JCAP **1601** (2016) 028, arXiv:1507.07569.

[2] S. Chakraborty, R. S. Hansen, I. Izaguirre and G. Raffelt, "*Self-induced neutrino flavor conversion without flavor mixing*," JCAP **1603** (2016) 042, arXiv:1602.00698.

[3] S. Chakraborty, R. Hansen, I. Izaguirre and G. Raffelt, "*Collective neutrino flavor conversion: Recent developments*," Nucl. Phys. B **908** (2016) 366, arXiv:1602.02766.

[4] I. Izaguirre, G. Raffelt and I. Tamborra, "*Fast Pairwise Conversion of Supernova Neutrinos: A Dispersion-Relation Approach*," Phys. Rev. Lett. **118** (2017) 021101, arXiv:1610.01612.

I have also worked on other topics, which are not included in this thesis. These works are:

[5] B. Garbrecht and I. Izaguirre, "*Phenomenology of Baryogenesis from Lepton-Doublet Mixing*," Nucl. Phys. B **896** (2015) 412, arXiv:1411.2834.

[6] S. Chakraborty and I. Izaguirre, "*Diffuse neutrinos from extragalactic supernova remnants: Dominating the 100 TeV IceCube flux*," Phys. Lett. B **745** (2015) 35, arXiv:1501.02615.

[7] S. Chakraborty and I. Izaguirre, "*Star-forming galaxies as the origin of IceCube neutrinos: Reconciliation with Fermi-LAT gamma rays*," arXiv:1607.03361.

Contents

Chapter 1

Introduction

> I have done a terrible thing, I have postulated a particle that cannot be detected.
>
> *Wolfgang Pauli*

1.1 The "invisible" particle

The current knowledge on particle physics has been encapsulated in a very elegant theory called Standard Model (SM). This theory describes with exquisite simplicity phenomena that range from electroweak to strong gauge interactions. Moreover, the SM has been tested to a high accuracy with the currently available accelerators, and so far has shown a resounding success describing the microscopic interactions of elementary particles. Despite these great achievements, there are still some loopholes, some gaps that the SM has not been able to fill which have stimulated physicist's creativity to find physics beyond the SM. One of these limitations has to do with an elementary particle called *neutrino*.

In the early 1930's, the Austrian physicist Wolfgang Pauli was studying a nuclear reaction called β-decay. In this process, there was an apparent non-conservation of angular momentum and energy. To avoid this interpretation, he predicted an "invisible" particle, which could escape undetected and therefore conserve both angular momentum and energy. He referred initially to this particle as neutron, because it had no electric charge. After the discovery of the "real" neutrons in 1932, this particle was renamed as neutrino. Neutrinos have many particularities which make them unique: they do not have an electric charge, only interact weakly, and are extremely light. Detecting these elusive particles was not an easy task. Indeed, it took decades to get any experimental evidence of neutrinos. Since neutrinos have been established experimentally, they have raised some questions to the very foundations of the SM. Indeed, the

non-zero neutrino masses are currently one of the most conspicuous evidence that there must be physics beyond the SM. Neutrino masses are so small that for a long time they were thought to be zero. However, it was later established that neutrinos have tiny non-zero masses.

The laboratory used for this discovery was the heavens: cosmic rays, i.e., accelerated particles (mostly electrons, protons, and α particles) mainly originating outside the Solar System, impact with the Earth's atmosphere and produce neutrinos. When the neutrino flux was initially detected at the Super-Kamiokande detector, a difference was observed between the flux from the neutrinos coming directly from the sky (above the detector) and those which had traveled through the Earth (neutrinos coming from below the detector). This was very intriguing, because cosmic rays arrive isotropically at the Earth's atmosphere. This results led to the conclusion that neutrinos do not conserve flavor during their propagation. This was successfully explained by assigning neutrinos a mass, which induces flavor oscillation on neutrino propagation.

The concept of using the heavens as a laboratory to test fundamental physics is not a novel idea: the dynamics of celestial objects were used used to test Newtown's classical mechanics. Indeed, astrophysics is nowadays frequently used to test the properties of elementary particles and their interactions. Neutrinos are the perfect example: scientist have turned at the celestial objects to study these elusive particles. In this context, stars are extremely interesting neutrino laboratories because conditions inside this objects will never be reproduced in a terrestrial laboratory. Historically, the attention turned first to the closest star to Earth: the Sun. The Sun's interior consists of a hot plasma where nuclear reactions are constantly taking place. These reactions generate an enormous neutrino flux which can be measured on Earth. This flux, which had been theoretically predicted by John N. Bahcall, was first measured in the late 1960's. However, the electron neutrino flux measured was approximately a third of the expected one. This discrepancy received the name of solar neutrino problem. This mystery was solved with the inclusion of flavor oscillations on the flux, so that the missing electron neutrino flux had oscillated to the μ and τ flavors.

Nonetheless, even after the resolution the solar neutrino problem, the Sun continued to serve as a useful laboratory for neutrino physics. The physicists Mikheyev, Smirnov and Wolfenstein discovered that the dense matter present in the Sun's core produces an important effect on the neutrino dispersion relation, leading to visible effects in flavor oscillations. This phenomenon received the name of the MSW effect, and it is dominant for energies over 5 MeV.

In the light of the MSW effect, it is reasonable to think that, if the density is high enough, the neutrino background could also affect neutrino propagation. However, because neutrinos interact only through weak interactions, the conditions for this effect to take place must be extreme. Typical stars like e.g. the Sun are not suitable for it. Indeed, there are only two environments where these extreme densities are reached: a supernova (SN) core and the

Early Universe. Neutrinos thus play a dominant role in the SN and cosmic evolution. This thesis is focused on SNe, so we will turn our attention to these astrophysical objects.

1.2 Supernovae as neutrino laboratories

Core-collapse SNe represent one of the most energetic events in the cosmos. They consist of explosions which mark the violent death of massive stars ($M > 8M_{\odot}$) as they become unstable during the late phases of their evolution. Moreover, most of the SN's energy is released in the form of neutrinos, which make them very powerful neutrino sources. The interior of these objects is highly dense. Indeed, the neutrino density is high enough for neutrinos to start feeling each other's presence. The resulting equations are non-linear and produce umpteen interesting effects which have just recently begun to be explored. On top of that, neutrinos play a role in the dynamics of the SNe explosion, and indeed they are thought to be fundamental for the explosion to take place. Therefore, understanding the neutrino flavor evolution has not only implication for the emitted neutrino flux but also for the dynamics of the explosion itself. This elegant interplay makes SNe unique laboratories to study neutrinos.

Neutrino self-interactions

Neutrino-neutrino interactions or neutrino *self-interactions* cause the "background medium" to evolve along with the system under study. In other words, neutrino evolution feeds back unto itself. This makes the evolution to be of non-linear nature. This non-linearity introduces an enormous amount of complexity. Self-induced neutrino oscillations in a SN requires dealing with a seven-dimensional partial differential equation (one dimension for time, three dimensions for the position in space, three for the momentum). Moreover, the system is highly coupled, which requires keeping track of the countless local non-linear interactions between beams traveling in different directions while simultaneously paying attention to the evolution of the supernova. This problem is very hard to solve not only analytically but also numerically because its complexity is above current computational power.

The physicist's approach in such a situation is to decrease the complexity of the system by introducing assumptions or simplifications to reduce the problem to a level where it can be dealt with. The downside of this approach is that, if we simplify the system *too much*, the defining features of the problem might get lost. In the context of collective effects in SNe, many different simplifications were implemented. These simplifications ranged from geometry assumptions to stationarity. Thanks to these simplified toy models, several studies were conducted. However, it became apparent that some of these assumptions where too restrictive. Moreover, by means of the phenomenon of

spontaneous breaking of symmetry, it was understood that the solutions of the system do not necessarily inherit the symmetries of the original problem.

In the light of these results, it became clear that a new general approach was needed where the results are not adulterated by the assumptions made. This has been precisely the main task of the work presented in this dissertation. We have dropped many assumptions traditionally adopted when dealing with neutrino self-induced flavor conversion in SN, and we have developed a general approach to study these systems.

1.3 Outline of the thesis

This thesis is structured in the following manner: after the introductory chapter, we will give brief review on neutrino physics in Chapter 2. In Chapter 3 we give a glimpse of the physics of core-collapse supernovae, where we focus on these aspects were neutrinos play an important role. Chapter 4 introduces the theoretical framework to describe the neutrino field at the refraction level in highly dense environments. We will discuss the neutrino density matrix formalism and its advantages. We also introduce some interesting simplifications. We will particularize to the two flavor framework. We will also linearize the equation of motion (EOM), and we will explain the linearized stability analysis.

In Chapter 5, the plane wave solution will be developed, and then the general dispersion relation (DR) is introduced. We apply our formalism to the two neutrino beam toy model. The results will be used to explain the fundamental features of the dispersion relation (DR). More precisely, we will discuss the concept of "forbidden" regions and the implications for the stability analysis. The rest of this thesis is devoted to apply the developed mathematical framework in different SN inspired scenarios[1].

In Chapter 6 we will analyze the bulb geometry applied to a stationary scenario where there is an inhomogeneity in the perpendicular direction. The whole study is performed under the assumptions that the angular distribution for both neutrinos and antineutrinos are equal.

In Chapter 7, we will continue using the bulb geometry, but we will adopt the massless neutrino limit. Furthermore, we will no longer assume the same angular distribution for neutrino and antineutrinos. Furthermore, the whole analysis is performed in the limit where the neutrino masses are zero, i.e., the vacuum oscillation frequency $\varpi = \Delta m^2/2E$ is zero. The first part of this chapter is dedicated to analyze the so-called two neutrino bulb model, but still under the assumption of stationarity. Once this case has been discussed, we will drop the stationarity and study the spatial and temporal evolution of the neutrino field. For this study we will use the angular distribution obtained

[1] The reader familiar with the field might note that the structure of this thesis is essentially anti-chronological with respect to historical development of it. However, we believe that this structure follows a more logical development.

from a 1D neutrino driven core-collapse SN explosion simulation. In the last sections of this chapter we briefly discuss compact binary-merger remnants. More precisely, we will discuss the particularities of their emission spectra and their impact in the DR.

Finally, we discuss in Chapter 8 the recent progress made in this field and future challenges.

Chapter 2

Neutrino Physics

This whole thesis is dedicated to neutrinos and their behavior in dense environments. Therefore, it is imperative to start with a summary of neutrino physics. The present chapter is devoted to this end. As mentioned in the introduction, neutrinos are very special particles. Their weakly-interacting nature, their tiny masses, and their charge neutrality make them one of the most interesting particles of the Standard Model (SM). We will start the chapter studying the neutrino Lagrangian's structure and we will analyze the main characteristics of neutrino interactions. Then we will discuss the origin of neutrino masses and the nature of the mass term. The next section will be dedicated to explain neutrino flavor conversion, discussing its origin and its physical effects. We start discussing neutrino vacuum oscillations, and right after we will study neutrino oscillations in the presence of matter. In the last section, we will discuss the open questions in the neutrino field, explaining briefly the different experimental attempts to give answers to these open issues. We conclude with a summary.

2.1 Neutrinos in the Standard Model

As mentioned in the introduction, neutrinos were introduced as a "desperate"[1] solution for angular momentum and energy conservation in beta decay. These newly postulated particles were by definition fermions, and were very weakly coupled, which in modern language can be more precisely formulated by saying that they only undergo weak interactions. This last statement means that they are a singlet to the $SU(3)$ color group or, in other words, they do not participate in the strong interactions. Furthermore, neutrinos have no electric charge.

There are three families or flavors of neutrinos: ν_e, ν_μ, and ν_τ, with the corresponding antiparticles: $\bar{\nu}_e$, $\bar{\nu}_\mu$, and $\bar{\nu}_\tau$. All three flavors interact in reactions

[1] Pauli's words were "verzweifelter Ausweg", which translate to "desperate way out".

mediated by $W^{\pm}$ bosons. These are referred to as charged current (CC) interactions. On the other hand, neutrinos can also interact in processes mediated by the Z^0 boson. These are named neutral current (NC) interactions. From this last kind of interactions, the decay $Z^0 \to \nu_a \overline{\nu}_a$ is particularly interesting. The importance of this process relies on the fact that it can be used to infer the number of active, light neutrino species. This number is determined from the number of kinematically allowed channels, which, from the measurement of the Z^0 boson decay width, is determined to be (2.992 ± 0.007) [8], which agrees with the three active neutrino model.

As we have already stated, neutrinos undergo weak interactions. These types of interactions are described by the symmetry group $SU(2)_L \times U(1)_Y$. The term of the Lagrangian density responsible for the weak interactions is

$$\mathcal{L} = -\frac{g}{2\sqrt{2}} J^{\mu}_{\mathrm{CC}} W_{\mu} - \frac{g}{2\cos(\theta_{\mathrm{W}})} J^{\mu}_{\mathrm{NC}} Z_{\mu} + h.c., \tag{2.1.1}$$

where θ_{W} is the Weinberg angle, g in the coupling constant for the $SU(2)_L$ group, and J^{μ}_{NC}, J^{μ}_{CC} are the neutral and charged weak currents, respectively. They can be explicitly written as

$$J^{\mu}_{\mathrm{CC}} = 2(\overline{\nu_{eL}}\gamma^{\mu} e_L + \overline{\nu_{\mu L}}\gamma^{\mu}\mu_L + \overline{\nu_{\tau L}}\gamma^{\mu}\tau_L) + \text{quark terms} \tag{2.1.2}$$

$$J^{\mu}_{\mathrm{NC}} = 2(g^{\nu}_L \overline{\nu_{\alpha L}}\gamma^{\mu}\nu^{\alpha}_L + g^{l}_L \overline{l_{\alpha L}}\gamma^{\mu} l^{\alpha}_L + g^{l}_L \overline{l_{\alpha R}}\gamma^{\mu} l^{\alpha}_R) + \text{quark terms}, \tag{2.1.3}$$

where $g^{l}_R = \sin^2(\theta_W)$, $g^{l}_L = -1/2 + \sin^2(\theta_W)$ and $g^{\nu}_l = 1/2$. The lower index L refers to the left-handed projections, which are given by the left-handed chirality operator $P_L = (1 - \gamma_5)/2$. Conversely, $P_R = (1 + \gamma_5)/2$ is the right-handed chirality operator, which is responsible for the terms with lower index R. By carefully inspecting these two currents, we realize the very distinctive feature of weak interactions: they only affect left-handed chiral neutrinos.

For energies below the mass of the gauge bosons M_Z and M_W ($\sim$80 and $\sim$91 GeV, respectively), the NC and CC interactions can be described by an effective Lagrangian. Under this description, the interactions are depicted by four-point interactions given by the effective operator

$$\mathcal{L}_{\mathrm{eff}} = -\frac{G_{\mathrm{F}}}{\sqrt{2}} J^{\mu\dagger}_{\mathrm{CC}} J_{\mu\mathrm{CC}} - 2\frac{G_{\mathrm{F}}}{\sqrt{2}} J^{\mu\dagger}_{\mathrm{NC}} J_{\mu\mathrm{NC}}, \tag{2.1.4}$$

where G_{F} is the Fermi constant, defined as $G_{\mathrm{F}} = \sqrt{2}g^2/(8M^2_W)$. From this operator we can infer the key feature of the weak interactions: the interaction strength is proportional to the Fermi constant, which in turn is inversely proportional to the squared mass of the W boson m_W. Because this mass is heavy, the Fermi constant is extremely small, with a value of $G_{\mathrm{F}} = 1.166 \times 10^{-5}$ GeV^{-2}, and thus makes the weak interactions indeed *weak*.

2.2 Neutrino masses

Neutrinos were postulated as massless particles. However we know that at least two neutrinos have a mass different from zero, as a we will discuss in the

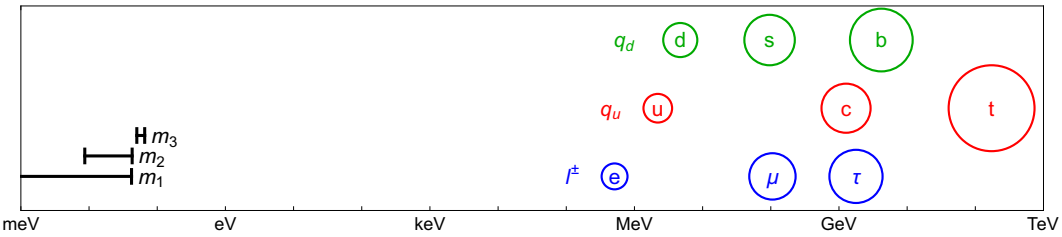

Figure 2.1: Schematic representation of the masses of the elementary particles of the SM, where the charged leptons are plotted in blue, up-type quarks are plotted in red, and down-type quarks are plotted in green. Neutrino mass eigenstates are plotted in gray. For simplicity, we have chosen the normal ordering, a scheme that is explained in the next section. There is a gap of six orders of magnitude between m_e and the domain where the neutrino masses are located.

next section. Moreover, these masses are confined to the sub-eV range. This is a fundamental characteristic of neutrinos, because their light masses make them unique and different from all other elementary fermions.

All particles of the SM acquire their mass term from the Higgs mechanism [9]. This seems unlikely to be the origin of the neutrino masses, because their small values would require extremely small Yukawa couplings $\mathcal{O}(10^{-12})$, which seems to go against the naturalness principle. Furthermore, there is another hint for this hypothesis. It can be inferred from Figure 2.1. In this figure, we have displayed the masses of the particles of the SM. The gap between the masses of all other particles with respect to neutrinos, of six orders of magnitude in a logarithmic plot, is also pointing to a different origin for the neutrino masses. There are a hand full of mechanisms proposed for the origin of the neutrino mass term. One of the most common ones is the See-saw Mechanism (see Reference [10] for a review) or very recently it has been proposed that neutrino masses emerge from a topological formulation of the gravitational anomaly [11].

Regardless of the exact origin of the mass term, there is a fundamental question to be addressed. The question refers to the nature of the neutrino mass term. As we have already mentioned, neutrinos have no charge. Therefore, they are suitable to be their own antiparticles, or in other words, they can have a Majorana mass term. We will explain now this point in more detail.

The easiest mechanism to provide a mass for neutrinos is extending the SM by introducing the right handed counterparts for neutrinos ν_R. These particles, usually referred as *sterile neutrinos* are a singlet to all interactions in the SM, including weak interactions. We will discuss these particles in more detail in Section 2.4. The inclusion of sterile neutrinos is referred to as the *minimally extended SM*, and in this model we can write a Dirac mass term for neutrinos such as

$$\mathcal{L}_{\mathrm{D}} = -m(\overline{\nu_R}\nu_L + \overline{\nu_L}\nu_R). \tag{2.2.1}$$

On the other hand, for neutrinos, due to their lack of electric charge, it is also possible to construct a mass term containing only left-handed fields. This mass term is

$$\mathcal{L}_{\mathrm{M}} = -\frac{1}{2} M(\overline{\nu_L^C}\nu_L + \overline{\nu_L}\nu_L^C), \tag{2.2.2}$$

and is the so-called *Majorana* mass term. The ν_L^C is the charge conjugated neutrino field, and the factor $1/2$ is introduced to account for the double counting of degrees of freedom. This mass term violates lepton number by two units. Of course, the question of neutrinos being Majorana or Dirac particles only makes sense under the condition that the neutrino masses are non-zero, because for the massles limit there is no distinction between chirality and helicity.

Because neutrino masses are not zero, it becomes very relevant to determine the exact nature of the mass term, since it is crucial in situations where lepton number violation plays a role. One of these situations is the neutrinoless double beta decay. Another example is a theory called Leptogenesis, which has been proposed to explain the baryon asymmetry of the universe. Nonetheless, it is also fair noticing that for neutrino oscillations, which will be the topic of our next section, the nature of the mass term does not play a role whatsoever.

2.3 Neutrino oscillations

2.3.1 Neutrino masses and mixing angles

Up to this point, we have highlighted two very important aspects of neutrino physics. Firstly, we have discussed the neutrino interactions and how they are solely sensitive to the weak interaction. Secondly, we have established that neutrinos have mass and will therefore propagate in their mass eigenstates. The crucial point is however that these mass eigenstates are not the same as the interactions eigenstates. This is the origin of a very interesting phenomena known as neutrino oscillations. This very same phenomenon happens for quarks. However, it is quite different in the neutrino case. Unlike in the quark sector, the misalignment between the mass and the weak eigenvalues is very significant, leading to large mixing angles. The relation between the mass and the interaction bases can be expressed as

$$|\nu_\alpha\rangle = \sum_{k=1}^{3} U_{\alpha k}^* |\nu_k\rangle, \tag{2.3.1}$$

where the matrix U, which parametrizes the misalignment, is the Pontecorvo-Maki-Nakagawa-Sakata (PMNS) matrix [12]. It can be explicitly written as

$$U = \begin{pmatrix} 1 & 0 & 0 \\ 0 & c_{23} & s_{23} \\ 0 & -s_{23} & c_{23} \end{pmatrix} \begin{pmatrix} c_{13} & 0 & s_{13}e^{-i\delta_{CP}} \\ 0 & 1 & 0 \\ -s_{13}e^{i\delta_{CP}} & 0 & c_{23} \end{pmatrix} \begin{pmatrix} c_{12} & s_{12} & 0 \\ -s_{12} & c_{12} & 0 \\ 0 & 0 & 1 \end{pmatrix}, \tag{2.3.2}$$

where $c_{ij} = \cos(\theta_{ij})$ and $s_{ij} = \sin(\theta_{ij})$ are the sines and cosines of the mixing angles and δ_{CP} is the CP phase. We have deliberately left out the Majorana phase matrix because it does not play any role in the physical processes we are about to describe. We will discuss in more detail the Majorana phase in Section 2.4.

As we will discuss in the next section, from the current results of neutrino oscillation experiments, it is inferred that there are three neutrino species. Furthermore, at least two of them have a non-zero mass. In other words, there are a total of two mass differences. The mass eigenstates are distributed in the following way: two states are very close and form a doublet, whereas a third state is separated from the other two. Since all oscillation experiments are only sensitive to the squared mass difference, their ordering is uncertain. The lightest mass of the doublet is by convention named ν_1, while the other one is ν_2. Their mass difference is referred to as $\Delta m^2_{\text{sol}} = m_2^2 - m_1^2$, which was first detected in solar neutrino data. The sign of this mass difference it has been inferred due to the MSW effect, as we will explain in Section 2.3.3. The third neutrino mass state is referred to as m_3. The second mass squared difference is commonly known as the atmospheric mass difference since it was first measured in atmospheric neutrinos. It is defined as

$$\Delta m^2_{\text{atm}} = \left| m_3^2 - \frac{m_1^2 - m_2^2}{2} \right|. \tag{2.3.3}$$

The sign of this mass difference is currently unknown. This allows for two different setups. The two possibilities are named normal ordering (NO) and inverted ordering (IO). They are pictorially displayed in Figure 2.2.

Combining the latest results of solar, reactor, and long-baseline experiments the following parameters at 95% CL [14–16] are obtained:

$$\begin{aligned} \Delta m^2_{\text{atm}} &= (2.43^{+0.12}_{-0.13}) \times 10^{-3}\ \text{eV}^2, \\ \Delta m^2_{\text{sol}} &= (7.54^{+0.46}_{-0.39}) \times 10^{-5}\ \text{eV}^2, \\ \sin^2\theta_{12} &= (3.48^{+0.17}_{-0.34}) \times 10^{-1}, \\ \sin^2\theta_{23} &= (4.37^{+1.15}_{-0.44}) \times 10^{-1}, \\ \sin^2\theta_{13} &= (2.34^{+0.40}_{-0.39}) \times 10^{-2}. \end{aligned} \tag{2.3.4}$$

Besides the information about the neutrino mass differences obtained from the neutrino oscillation experiments, results from cosmology and from beta decay experiments can be used to obtain an upper bound for the absolute value of the neutrino masses. The most constraining limit is given by the

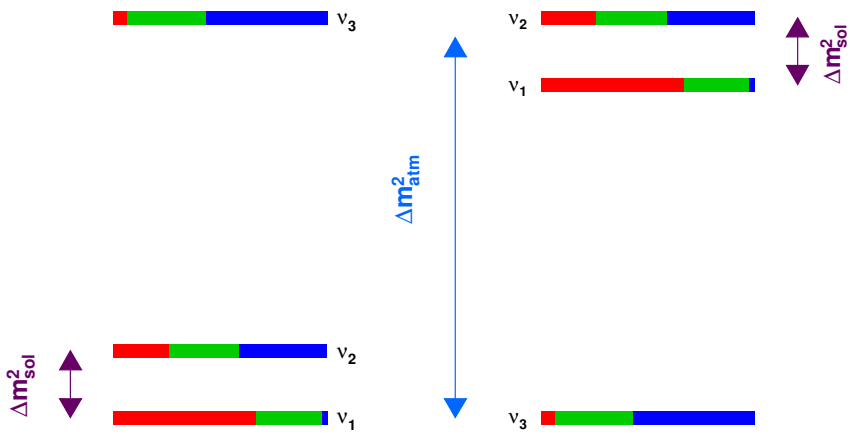

Figure 2.2: Schematic representation of the neutrino mass eigenstates [13]. The color represents the flavor content, red for the e flavor, blue for μ and green τ. The right column corresponds to the IO, and the left column to the NO.

Planck collaboration [17] and sets an upper bound on the sum of the neutrino masses of

$$\sum m_\nu < 0.23 \text{ eV}. \tag{2.3.5}$$

2.3.2 Vacuum oscillations

Neutrino oscillations are a quantum mechanical phenomenon which results from the mass and interaction bases misalignment. It was first proposed in the 1950's by the Italian physicist Bruno Pontecorvo, inspired by the CKM matrix of the quark sector. It took several years to obtain experimental evidence of this phenomena, whose first experimental success was the solution to the solar neutrino problem.

We will now discuss the physics of neutrino oscillations. As a starting point, we will remind the reader that neutrino mass states are eigenstates of the Hamiltonian

$$H|\nu_k\rangle = E_k|\nu_k\rangle, \tag{2.3.6}$$

where the energy eigenvalues are given by the dispersion relation

$$E_k = \sqrt{p^2 + m_k^2}. \tag{2.3.7}$$

On the other hand, the massive neutrino states evolve in time as plane waves, obeying a Schrödinger-like equation

$$i\partial_t|\nu_k\rangle = H|\nu_k\rangle, \tag{2.3.8}$$

where the eigenfunctions will be plane-waves of the form

$$|\nu_k(t)\rangle = e^{-iE_k t}|\nu_k\rangle. \tag{2.3.9}$$

Moreover, neutrinos produced in CC interactions are produced in flavor eigenstates. The time evolution of a flavor eigenstate is given by

$$|\nu_\alpha(t)\rangle = \sum_{k=1,2,3} U^*_{\alpha k} e^{-iE_k t}|\nu_k\rangle, \tag{2.3.10}$$

where $U^*_{\alpha i}$ are the matrix elements of the PMNS matrix. Using the unitarity of this matrix, we can rewrite Equation 2.3.10 as

$$|\nu_\alpha(t)\rangle = \sum_{\beta=e,\mu,\tau} \sum_k U^*_{\alpha k} e^{-iE_k t} U_{\beta k}|\nu_k\rangle. \tag{2.3.11}$$

We will now analyze the physics behind these equations. At an initial time $t = 0$, a neutrino is produced in a pure flavor eigenstate. This flavor eigenstate is a superposition of the propagation eigenstates, all of them propagating at different velocities. Therefore, after some time, there is a non-zero probability that when the neutrino interacts with a detector, the measured flavor has changed or *oscillated*. The transition probability is then defined as the probability of a neutrino of any flavor to have converted to another flavor, and is expressed as

$$P_{\nu_\alpha \to \nu_\beta} = |\langle \nu_\alpha | \nu_\beta \rangle|^2. \tag{2.3.12}$$

For the sake of simplicity, we will consider the two flavor toy model to discuss neutrino oscillations. In this scenario, there are two mass eigenstates $\nu_{1,2}$ and the 2×2 mixing matrix can be written as

$$U = \begin{pmatrix} \cos\theta & \sin\theta \\ -\sin\theta & \cos\theta \end{pmatrix}, \tag{2.3.13}$$

with the mixing angle θ and only one mass splitting $\Delta m^2 = m_2^2 - m_1^2$. The equations simplify very conveniently if we are dealing with ultrarelativistic neutrinos. In that case, we can use the approximation $E_k = \sqrt{p^2 + m_k^2} \simeq p + m_k^2/2p$. Furthermore, we can use $E = |\vec{p}|$, and therefore $E_k - E_j \simeq \Delta m^2_{kj}/2E$. With this taken into consideration, the transition probability can be written as

$$P_{\nu_\alpha \to \nu_\beta} = |\langle \nu_\alpha | \nu_\beta \rangle|^2 = \tfrac{1}{2}\sin^2(2\theta)\left[1 - \cos\left(\frac{\Delta m^2 L}{2E}\right)\right]. \tag{2.3.14}$$

Furthermore, for $\beta = \alpha$, we obtain the survival probability, which is obtained from Equation 2.3.10 using the unitarity of the transition probability, so that

$$P_{\nu_\alpha \to \nu_\alpha} = |\langle \nu_\alpha | \nu_\alpha \rangle|^2 = 1 - \sin^2(2\theta)\sin^2\left(\frac{\Delta m^2}{4E} L\right). \tag{2.3.15}$$

We will now analyze these expression in some detail. First of all, we see that the oscillation amplitude is proportional to $\sin^2(2\theta)$, which in turn depends on

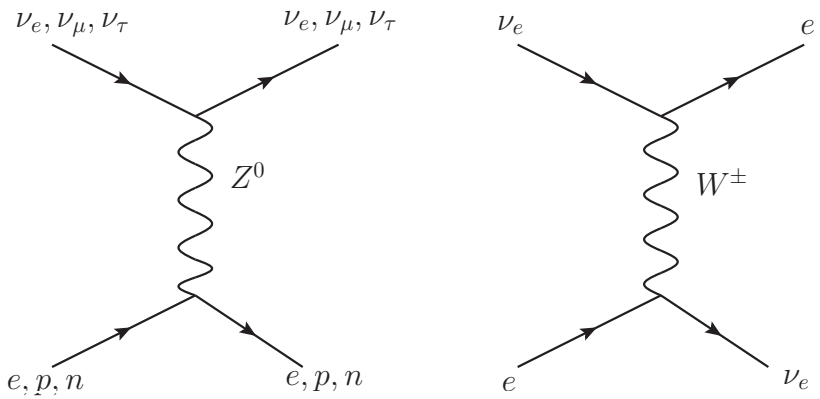

Figure 2.3: The two types of interactions neutrinos can have with matter. At low energies, the gauge bosons are too heavy to be produced as real particles and they can be integrated out. The cross-section of these processes varies roughly with the square of the energy at the center of mass, as inferred from Equation 2.1.4. The NC interaction (left diagram) interacts with all neutrino flavors, whereas the CC interaction (right diagram) requires the scattering on a charged lepton of the same flavor. This is actually what defines the flavor of a neutrino, since NCs do not distinguish between flavors.

the mixing angle θ. Nonetheless, for the amplitude we will have the "octant degeneracy", because the angles θ and $\pi/2 - \theta$ are indistinguishable. This feature does not hold for neutrino matter oscillations that we will discuss in the next Section. Moreover, the probability depends on three parameters: the energy, the mass difference and the baseline. We now define the oscillation length as

$$\lambda_{\text{osc}} = \frac{4\pi E}{\Delta m^2} = 2.47 \text{ m } \left(\frac{E}{\text{MeV}}\right)\left(\frac{\text{eV}^2}{\Delta m^2}\right). \tag{2.3.16}$$

The oscillation length depends on two parameters: the neutrino mass difference and the neutrino energy. Therefore, the interplay of these two parameters will determine the scale where neutrino oscillations produce measurable effects.

2.3.3 Neutrino oscillations in matter

It is a common phenomenon that particles, while traveling in a medium, change their characteristics. One example are photons traveling in plasma, where they acquire an effective mass and longitudinal polarization modes. Neutrino oscillations are also affected when traveling through dense matter, and due to these effects they can undergo resonant flavor conversion. This phenomena is known as the Mikheyev, Smirnov, and Wolfenstein (MSW) effect [18, 19].

The origin of the matter effects in neutrino oscillations is the potential induced by the matter field. In Figure 2.3 we show the neutrino interactions in matter. From this figure we can infer that NC interactions are universal,

in the sense that all neutrino flavors will undergo it in the same way. On the other hand, in SN type scenarios, the CC interactions only affect ν_e because for the temperatures and the chemical potentials in these environments there are no μ or τ. Therefore, when neutrinos travel through dense stellar matter, they acquire an effective matter potential given by

$$V_m^{\rm CC} = \sqrt{2} G_{\rm F} N_e, \tag{2.3.17}$$

where N_e is the electron number density of the medium. The NC interactions will of course produce a matter potential. However, this potential is equal for all neutrino flavors, meaning that the neutrino oscillations remain unaffected.

The Schrödinger equation for plane waves will now be of the form,

$$i\partial_t |\nu_\alpha\rangle = (H_0 + H_I)|\nu_\alpha\rangle, \tag{2.3.18}$$

where the H_I is caused by the matter potential mentioned above. For the sake of simplicity, we will consider a two flavor example, where we only have electron neutrinos ν_e and ν_x, where $x = \mu$ or τ. With the shift introduced by the matter field, the time evolution equation can be written as

$$i\partial_t \begin{pmatrix} \nu_e \\ \nu_x \end{pmatrix} = \begin{pmatrix} -\frac{\Delta m^2}{4E}\cos(2\theta) + A_m^{CC} & \frac{\Delta m^2}{4E}\sin(2\theta) \\ \frac{\Delta m^2}{4E}\sin(2\theta) & -\frac{\Delta m^2}{4E}\cos(2\theta) - A_m^{CC} \end{pmatrix} \begin{pmatrix} \nu_e \\ \nu_x \end{pmatrix}, \tag{2.3.19}$$

where $A_m^{\rm CC} = V_m^{\rm CC}/4E$. Equation 2.3.19 is not diagonal. However, we can diagonalize the Hamiltonian using the following transformation

$$\begin{pmatrix} \nu_A^m \\ \nu_B^m \end{pmatrix} = \begin{pmatrix} \cos(\theta_m) & -\sin(\theta_m) \\ \sin(\theta_m) & \cos(\theta_m) \end{pmatrix} \begin{pmatrix} \nu_e \\ \nu_x \end{pmatrix}, \tag{2.3.20}$$

where the $\nu_{A,B}^m$ are the so-called propagation eigenstates. On the other hand, the matter mixing angle θ_m is

$$\sin^2(2\theta_m) = \frac{\left(\frac{\Delta m^2}{2E}\right)^2 \sin^2(2\theta)}{\left[\frac{\Delta m^2}{2E}\cos(2\theta) - \sqrt{2} G_{\rm F} N_e\right]^2 + \left(\frac{\Delta m^2}{2E}\right)^2 \sin^2(2\theta)}. \tag{2.3.21}$$

This angle will be maximal if the terms between the square brackets in the denominator of this equation cancel. This condition can be written as

$$n_e^{\rm res} = \frac{\Delta m^2 \cos(2\theta)}{2\sqrt{2} E G_{\rm F}}, \tag{2.3.22}$$

and its referred to as the MSW resonance condition. For $n_e^{\rm res}$ given by Equation 2.3.22, the matter mixing angle will acquire a value of $\theta_m = \pi/4$, leading to a maximum flavor conversion.

In many astrophysical environments the matter density will vary spatially. For instance, the density inside stars decreases as a function of the radius. In

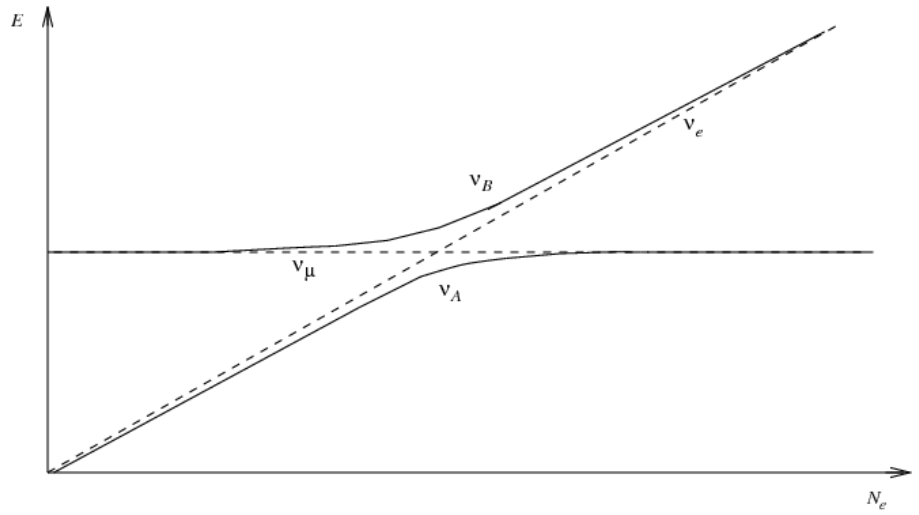

Figure 2.4: The evolution of the mass eigenstates as a function of the matter density and the energy. In regions where the density is very high neutrino propagation and flavor eingestates are the same. As neutrinos move outwards from the Sun, they will go to regions of lower matter density. The MSW condition $N_e = N_e^{\text{res}}$ is reached at the point where the energy gap for ν_A-ν_B is minimal.

order to explain how this affects the flavor conversion in a more intuitive way, we will use Solar Neutrinos as an illustrative example. The Solar Neutrino evolution as they travel through the Sun is represented in Figure 2.4, which are produced in the Sun's core due to nuclear reactions. In these deep Solar layers, the matter density is extremely high, such that $N_e \gg N_e^{\text{res}}$. Under this condition, the mixing angle is almost zero, and all the produced ν_e are almost eigenstates of ν_B, i.e., the propagation base. In other words, the electronic matter drags neutrinos onto the propagation basis.

The produced neutrinos will then propagate adiabatically through the Sun. In this context, adiabatic propagation means that the Solar density is slowly changing, or, in other words, the variation scale is of roughly the wave length in matter. Under these circumstances, the propagation eigenstates become eigenstates of the Hamiltonian. As neutrinos travel out of the Sun, the matter density will decrease, eventually reaching the condition $N_e = N_e^{\text{res}}$. At this point the energy gap between ν_A and ν_B is minimal.

Neutrinos will continue their adiabatic propagation, and by the time neutrinos have escaped the Sun, the propagation base will coincide with the mass base. Furthermore, no oscillations occur between the Sun and the Earth since neutrinos are already in the state of propagation in the vacuum.

This is the most outstanding feature of the MSW effect: despite of a very small mixing angle, the achieved flavor conversion is very significant. Thanks to the MSW effect, the Solar Neutrino data has been used to determine the sign of Δm^2_{sol}. Therefore, when we talk about the neutrino mass ordering

problem, we refer always to the sign of Δm^2_{atm}.

2.4 Open questions

Neutrino phenomenology is at the present time a very exciting field due to the numerous open questions that remain to be settled. Although we have mentioned some of them during the present chapter, we will now explain them in some detail, and we will mention some experiments designed to settle these issues.

CP phases

The CP-phase of the PMNS matrix allows for the possibility of CP violation, which is an intrinsic effect of the three-flavor scheme. Measuring the CP phase is extremely challenging since it requires a new generation of accelerator experiments with very long baselines [20], which are currently in the design phase.

Absolute masses

The order of magnitude of the mass differences inferred form the neutrino oscillation experiments gives us very little information about the absolute values of the masses. Fortunately, cosmology provides us with a bound on absolute neutrino masses. More specifically, the constraint refers to the sum of the three masses. This limit is inferred from structure formation, where neutrinos with a large mass would produce an excessive clustering. We refer to Reference [21] and references therein for a review.

On the other hand, the end point of beta decay can also be used to determine the absolute masses of neutrinos. The problem of this approach is that the sensitivity needed to observe the signal is beyond current detectors. In the near future, the KATRIN experiment is expected to improve the current bounds [22].

Majorana or Dirac

As we have already pointed out, another open question is the nature of the mass term. Because of the neutrinos's lack of charge, they are the only fundamental fermions of the SM that could have non-zero Majorana mass terms. This can be proved experimentally by measuring a neutrinoless double beta decay $(\beta\beta)_{0\nu}$. This process, which can be written as $(A, Z) \to (A, Z - 2 + e^- + e^-)$, if detected, would be a hint to probe that they behave like Majorana particles. Additionally, if neutrino are Majorana particles, that would imply the inclusion of two additional CP phases in the PMNS matrix, such that we add a term of

the form

$$U_{CP}^{M} = \begin{pmatrix} e^{i\alpha_1} & 0 & 0 \\ 0 & e^{i\alpha_2} & 0 \\ 0 & 0 & 1 \end{pmatrix} \tag{2.4.1}$$

to Equation 2.3.2. As we have already mentioned, these phases play no role on neutrino oscillations, but have an impact in lepton-number violating processes such as neutrinoless double beta decay.

Reactor anomalies

The three-flavor neutrino scheme has been very successful in the last decades explaining with great accuracy the observations of the oscillation measurements of solar, atmospheric and reactor neutrino experiments. However, there are some reactor experiments that cannot be explained with a three neutrino model. They are called reactor anomalies (see Reference [23] for a review). Until now it is unclear what is the exact origin of these anomalies [24].

The inclusion of a fourth species with a mass in the eV range seems to explain some of these anomalies, which some authors have interpreted as a hint towards the existence of a light *sterile neutrino* in the eV range.

Sterile neutrinos

By carefully examining the structure of the weak interactions, it becomes evident that a chiral right-handed neutrino would be a singlet for all fundamental interactions, thereby it is commonly referred to as *sterile neutrino*. A sterile neutrino would be extremely interesting for many different reasons. It could be responsible for the dark matter content of the universe, responsible for the smallness of the masses of the active neutrino species or the key ingredient to explain the current matter-antimatter asymmetry through the so-called *Leptogenesis*. Furthermore, if the sterile neutrino has a mixing with the active ones, it could be resonantly produced in the interior of heavily dense astrophysical objects such as core-collapse SNe. In such a situation, the produced sterile neutrino could escape the SN without interacting, thereby generating a new cooling channel. This could have a deep impact on the stellar evolution and on the physics of the core-collapse SNe.

2.5 Summary

Neutrinos are unique particles of the SM. They only interact weakly and gravitationally, and their lack of other interactions make them extremely difficult to be observed. There are also strong evidences of at least two neutrinos having non-zero masses. This is currently the strongest evidence of physics beyond the SM, since neutrino masses require new physics and brings up very interesting questions. Moreover, there are some indications for the neutrino mass

term having a completely different origin than the mass terms of all other SM particles. On top of that, neutrinos are the only fundamental neutral fermions, which makes them suitable for being Majorana particles, or in other words, being their own antiparticles.

The mass and interaction bases misalignment is also a very interesting feature of neutrinos. Although this is not exclusive for neutrinos, it is unique the large mixing angles between them. This translates in very rich phenomenology, where neutrino oscillations play a fundamental role. At the present time, there are many unresolved questions about neutrino physics. However, we are currently in a very exciting time for neutrino phenomenology. Because of the theoretical open questions we have addressed, there are plenty of experiments in the coming years designed to give answers to these questions.

Thanks to this great effort, in the near future we will (hopefully) be able to reveal the nature of these evasive, yet fascinating particles.

Chapter 3

Core-collapse supernovae

In this chapter, we will give a brief summary of the underlying physics of core-collapse SNe. As we will explain through the next pages, these astrophysical objects are unique “laboratories" to study neutrino properties. Furthermore, neutrinos play a fundamental role in the SN explosion dynamics. This interplay can be used to gain a deeper understanding of neutrino self-interactions. For these reasons, it is crucial to understand the basics of the core-collapse SN explosions. Although this subject alone would be enough to fill a complete dissertation, in this chapter we will simply sketch the fundamentals of it, explaining the different stages of the SN explosion and paying special attention to those aspects where neutrinos play an important role. We will also study the characteristics of the emitted neutrino flux, discussing its origin, the different phases, and spectral features. Since there is few experimental information available, we will also discuss the status of core-collapse SN simulations, with some interesting features that have shown up in state-of-the-art, three-dimensional runs. The experimental data of SN 1987A will also be discussed, and we will provide a brief prospect of future detection. We conclude with a summary.

3.1 Stellar evolution

One can think of stars as gravitationally regulated thermonuclear reactors. Among the many parameters that can be naively thought as crucial for the star’s evolution, such as the luminosity, composition or the temperature, the mass is the characteristic which plays the most fundamental role. More precisely, it is the star’s initial mass which will determine its evolution. Stars spend most of their life on the so called “main sequence", where the gravitational contraction is counteracted by the nuclear fusion of hydrogen atoms into helium. When hydrogen is exhausted at the star’s core, the star contracts, increasing the core’s temperature and therefore allowing for the next heaviest element, i.e., helium, to fuse. Meanwhile hydrogen continues to be converted

into helium in the outer layers of the star. If the star is massive enough, when the core runs out of helium, the core will contract once again and it will start "burning" carbon. Once carbon is fully consumed, for stars heavier than ten Solar Masses this process will happen again for silicon, producing iron.

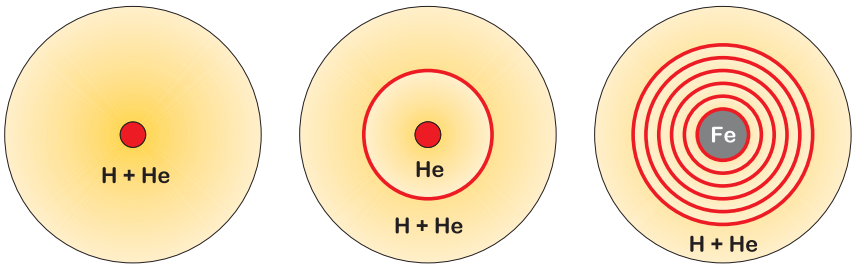

Figure 3.1: Schematic representation of stellar evolution [25]. The left panel shows the star in the main sequence, where the gravitational contractions is counteracted with hydrogen fusion. In the center panel, the star has exhausted the hydrogen in the core and helium is fused, although hydrogen still burns at the outer layers of the star. The right panel shows the "onion structure" that the star reaches in the last stage of evolution, with an inert iron core.

Iron is the end of the chain; more stable than all the neighboring elements of higher mass number, no nuclear energy can be released by iron fusion. The iron core is surrounded with an onion-like structure of heavier elements ordered according to their density, as pictured in Figure 3.1.

3.2 Core collapse

3.2.1 Collapse of the progenitor

After the silicon supply has been exhausted, the star will start the last stages of its life. The rest of the present chapter is devoted to explain the chain of events the star goes through upon this point. Figure 3.2 will serve as a storyline, since it shows the different stages, chronologically ordered, we are about to describe[1]. Once all the core's silicon is consumed, there is no further nuclear reaction taking place in the star's core. Therefore, the iron core will contract to counterbalance the gravitational force thanks to the pressure of the degenerate electron gas. Once the iron core has reached the Chandrasekhar limit, the pressure of the degenerate gas can no longer support the mass of the star. Once this point is reached, the internal balance is lost and inevitably the inner part of the star will start to collapse. This corresponds to the top-left panel of Figure 3.2.

Matter starts to free-fall at extremely high velocities (up to 1/3 of the speed of light) in the outer core, whereas the inner core will collapse at subsonic velocities. The increase in temperature and density will trigger photodisintegration

[1]For a recent review of this subject, we refer the reader to Reference [26].

through the process

$$\gamma + {}^{56}\text{Fe} \rightarrow 13\alpha + 4n - 124 \text{ MeV}. \tag{3.2.1}$$

Because this reaction is endothermic, it reduces electron pressure, converting thermal energy to rest-mass energy. The increase in pressure with rising density translates to a rise of the Fermi energy for the degenerate electrons, so electron capture via

$$e^- + \mathcal{N}(Z, A) \rightarrow \mathcal{N}(Z-1, A) + \nu_e, \tag{3.2.2}$$

becomes energetically favorable. The process described by 3.2.2 is called neutronization. At this stage these neutrinos escape the star without interacting.

3.2.2 Neutrino trapping

The star's density will increase along with the star's contraction. At a certain point, the environment is so dense that neutrinos, due to the large cross section of NC interactions with heavy nuclei, remain trapped, i.e., their diffusion time exceeds the time scale of the star's collapse. For 10 MeV neutrinos, this happens at densities of the order of 10^{12} g cm^{-3}. Therefore, after this density is reached, matter will become opaque to neutrinos. This stage corresponds to the second panel of Figure 3.2. The neutrinos trapped in the star's core become in thermal and chemical equilibrium with the surrounding matter through the reaction $p + e^+ \leftrightarrow n + \nu_e$. This results in the appearance of the so-called neutrino sphere, which will be described in the next section.

3.2.3 Core bounce and shock front formation

The collapse of the star will continue until the core reaches nuclear density (3×10^{14} g cm^{-3}), which is reached within milliseconds after neutrino trapping. At this stage, the nuclear pressure caused by nuclear repulsion forces induces a drastic change in the compressibility factor of the star's matter. This resistance against further compression will suddenly stop the in-fall of matter, changing abruptly from an implosion to an explosion, thus producing a shock wave. On the other hand, the neutrons and nuclei present in the core, i.e., behind the shock front begin to form the proto-neutron star through the neutronization process described by Equation 3.2.2, which causes the lepton number stored in the form of electrons to be converted into neutrinos. This core-bounce corresponds to the third panel of Figure 3.2. The produced shock wave will start traveling outside the iron core. Just behind the propagating shock-wave front there will be an extremely high production of electron neutrinos due to electron capture given by Equation 3.2.2. These produced neutrinos cannot escape from the interior of the collapsing star since the environment is neutrino-opaque. Nevertheless, the shock-wave continues to travel outwards from the star, and eventually reaches the point where matter is neutrino transparent.

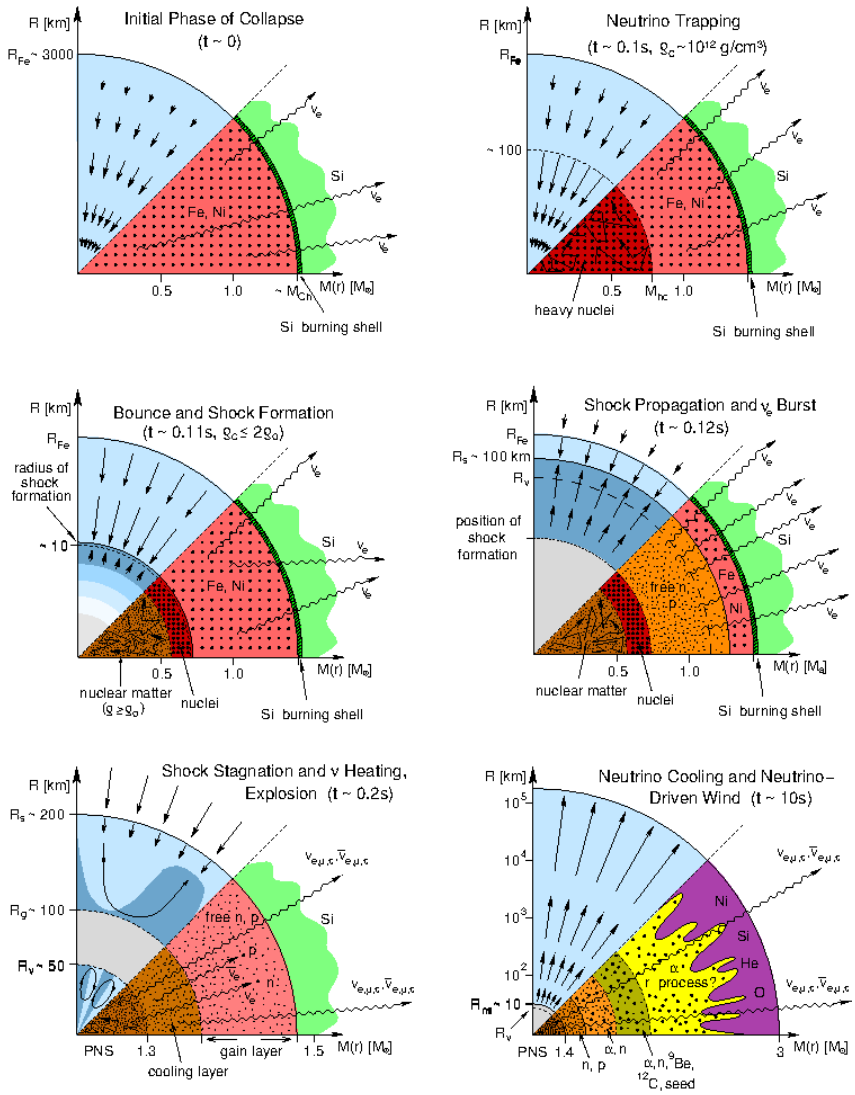

Figure 3.2: Schematic description of a core-collapse SN at different times after the initial phase of collapse [27]. The different phases of the collapse are labeled, showing for each of them the time after collapse and the density at the star's center. The vertical axis contains information about the radii, whereas the horizontal axis shows information about the masses. The first quadrant panels contain the dynamical information, with arrows representing the velocity vectors. The second quadrant provides information about the nuclear composition and the weak processes. $R_{\rm Fe}$ is the radius of the iron core, $R_{\rm S}$ is the radius of the shock front, R_ν is the radius of the neutrino sphere, $R_{\rm g}$ is the gain radius (the boundary between neutrino cooling and heating layers), and $R_{\rm ns}$ is proto-neutron star radius. The Chandrasekhar mass is $M_{\rm Ch}$.

When this point is reached, which corresponds to the forth panel of Figure 3.2, a very intense electron neutrino flux is emitted, which is referred to as *neutrino burst*.

Neutrino sphere

Meanwhile, deep inside the star's core, the trapped neutrinos remain in thermal and chemical equilibrium with the environment, at a temperature of order of tens of MeV. The region upon where neutrinos start to free-stream is known as *neutrino sphere*, which can be thought of as the neutrino equivalent of the photosphere for ordinary stars. Is it important to emphasize that in the highly dense environment of a SN's core the different neutrino species will have different interaction strengths, as we have discussed in Chapter 2. These differences of the interaction strengths mean that each neutrino species has a different neutrino sphere. More specifically, muon and tau neutrinos and their antiparticles decouple first and they will start to free stream at smaller distances from the star's center. Electron neutrinos and electron antineutrinos will decouple at different regions. More precisely, electron neutrinos will decouple at a higher radius because of the CC interactions. This will probe to be crucial when we discuss self-induced neutrino oscillations. In Figure 3.3 we have plotted the radius of the neutrino sphere for the electron flavor as a function of time.

3.2.4 Shock front stall and neutrino-induced revival

As the shock front propagates outwards, the high temperatures in the pre-shock environment causes the shock wave to practically disintegrate all heavy nuclei into free nucleons. This process consumes a lot of energy.

Due to these energy dissipating effects, the shock wave will lose momentum, leading to a stagnation at a distance of approximately 150 km from the star's center. However, this does not necessarily mean that the explosion does not succeed; numerical simulations show a revival of the shock-wave. The most plausible mechanism to revive the shock-wave and consequently to revive the explosion is energy transfer from the enormous neutrino flux coming form the emergent neutron star. For the neutrino-driven reignition mechanism, neutrinos will transfer energy to the shock-wave mainly through the reactions

$$\nu_e + n \to p + e^-, \tag{3.2.3}$$

$$\bar{\nu}_e + p \to n + e^+. \tag{3.2.4}$$

According to state-of-the-art simulations these interactions provide enough energy to restart the explosion. While the shock-wave is reheated, part of the mass of the shock wave will form and accretion flow that will feed the nascent proto-neutron star an generates a hot-mass mantle around the star's core. This situation is shown in the lower left panel of Figure 3.2. Once the SN shock front is re-accelerated the explosion can finally take place. The core's surrounding

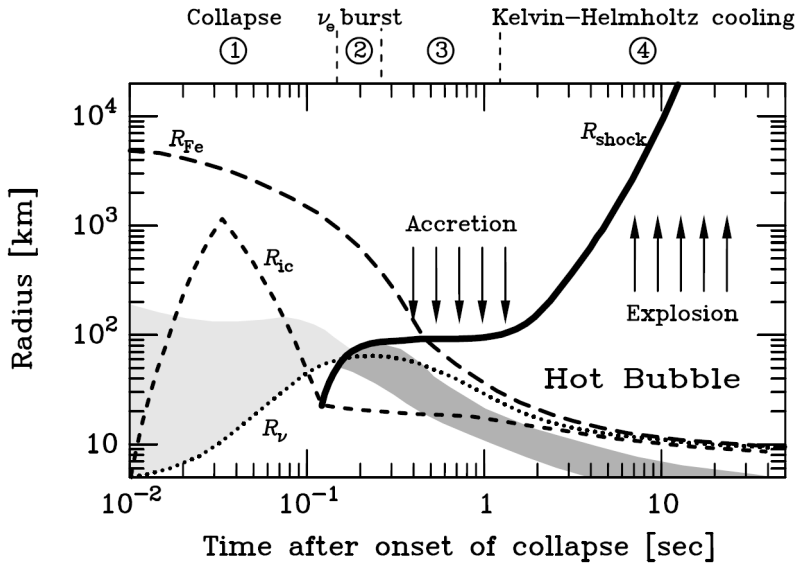

Figure 3.3: Schematic representation of the relevant radii of core collapse SN as a function of time [25]. The radii showed are: R_{Fe} is the iron core, R_{ic} is the inner core, and R_ν is the neutrino sphere for electron neutrinos, i.e., the radius from which electron neutrinos stream freely. The different phases of the neutrino emission are also shown. The neutrino sphere reaches its maximum radius during the very beginning of the accretion phase, where the high temperatures favor neutrino trapping. The cooling phase will decrease the core temperature and therefore neutrinos from deeper regions will be able to escape.

material is blasted away into the environment, leaving only a neutron star remnant.

3.2.5 Cooling phase and neutrino wind

The accretion phase of the nascent neutron star will continue for some time (from hundreds of milliseconds up to one second, depending on the progenitor mass) after the explosion has taken place. As soon as the accretion comes to an end, the newly formed neutron star will start the Kelvin-Helmholtz cooling phase. This phase corresponds to the lower-right panel of Figure 3.2. The proto-neutron star's hot interior will continue to radiate, i.e., it will continue to cool down through neutrino pair production with some diffusive losses. The temperature of the neutron star can go up to 50 MeV and the energy of the produced neutrinos reach up to 100 MeV. Nonetheless, these neutrinos will lose energy through a repeated absorption-emission cycle, so that the energy of the emitted ones will be 10–20 MeV.

Neutrino wind

The emitted neutrinos during the cooling phase will affect the cooler outer layers of the star. These neutrinos will transfer energy to the surrounding layers through the same mechanism described by Equation 3.2.3. This also generates a very slow outflow of mass from the newly born neutron star. This effect is known as neutrino wind. It is very important to understand the characteristics of the neutrino wind since it can alter the proton-to-neutron ratio in the star's surroundings. This affects the synthesis of heavy nuclei, a process known as nucleosynthesis.

3.3 Phases of neutrino emission

Up to the point where the star's core has contracted enough to ignite carbon combustion, the density is so high it is completely opaque to photons. Therefore, the only window to what happens to the star's guts are neutrinos. Moreover, they are the only efficient mechanism to cool the star; 99% of the SN's energy ($\sim 3 \times 10^{53}$ erg) is released as neutrinos. After the silicon has been completely consumed, there are no further nuclear reactions taking place in the star's core. Yet this does not mean that the neutrino emission stops. It is actually at this point that the emitted neutrino flux reaches its peak. In this section, we describe in detail the neutrino emission of core-collapse SNe, which is represented in Figure 3.4. The neutrino emission will be divided in three phases which are directly related to the physical processes described in the previous section.

3.3.1 Neutrino Prompt Burst

This phase corresponds to the left column of Figure 3.4. In this case, the emitted neutrinos come from the electron capture that we have discussed in Section 3.2.3. This is the shortest stage of neutrino emission, lasting around 10 ms, albeit it exhibits the highest luminosity, with a peak value of $\sim 10^{54}$ erg s^{-1}. The total energy released during this stages is $\sim 10^{51}$ erg and the average energy of the emitted neutrinos is ~ 10 MeV. The neutrino luminosity shows a sharpened peak, with a half width of around 10 ms. During this stage, there is a strong hierarchical neutrino spectrum, consisting almost entirely of electron neutrinos, with the other species only contributing negligibly. The neutrinos produced during this phase can undergo the MSW effect [29].

3.3.2 Accretion phase

Right after the neutrino burst comes the accretion phase. It corresponds to the center column of Figure 3.4. This is a comparatively longer stage, with

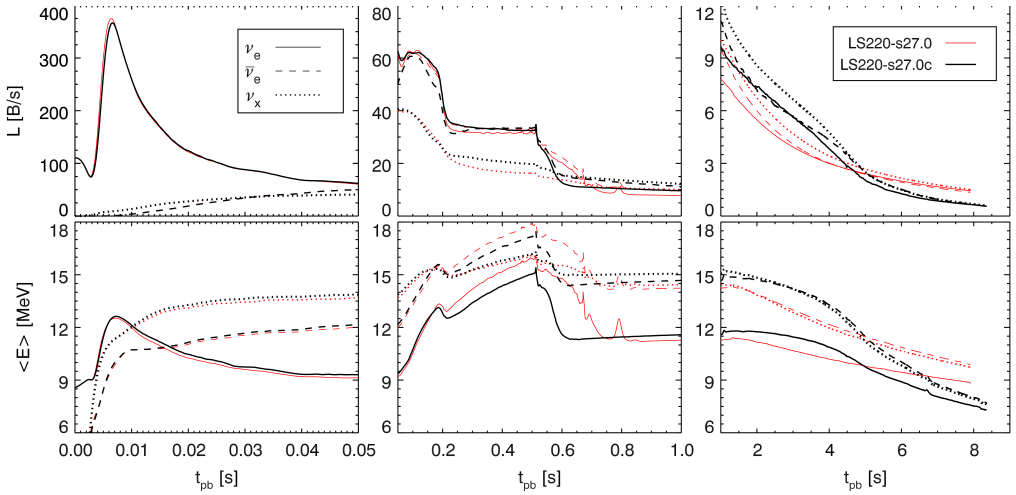

Figure 3.4: Schematic neutrino emission spectra from a SN with a progenitor mass of 27 $M_\odot$ as a function of time [28]. The first line is the neutrino luminosity, whereas the second line is the averaged neutrino energy. The luminosity is given in units of B/s = 10^{51} erg s^{-1}. The emission is divided in three phases as described in the text. Note that the scale of the vertical axis for the luminosity is different for the different phases due to the big differences between each phase. Electron neutrinos are plotted by solid lines, electron antineutrinos with dashed lines, and the rest of the neutrinos species with dotted lines. The black lines correspond to a 1D model without convection, whereas the the red lines correspond to a 1D model where convection effects are taken into account. In both cases the progenitor star has a mass of 27 $M_\odot$.

a duration of order of hundreds of milliseconds. The luminosity will be significantly lower than the neutrino burst, being typically $\sim 10^{49}$ erg s^{-1}. The outgoing flux is predominantly composed by ν_e and $\bar{\nu}_e$ fluxes, with a small excess of ν_e due to deleptonization. The spectra during this stage is specially sensitive to the progenitor's mass. It is during this stage where the neutrino self-induced flavor conversion is expected to occur.

3.3.3 Cooling phase

Lastly, the Kelvin-Helmholtz cooling phase takes place. It is shown in the right column of Figure 3.4. It is also the longest one, since it lasts about 10 seconds.The luminosity deceases rapidly, and the luminosity of all neutrino species are very similar (with differences of less than 10%). Therefore, it is important to consider the complete three flavor scheme when analyzing neutrino physics at this stage.

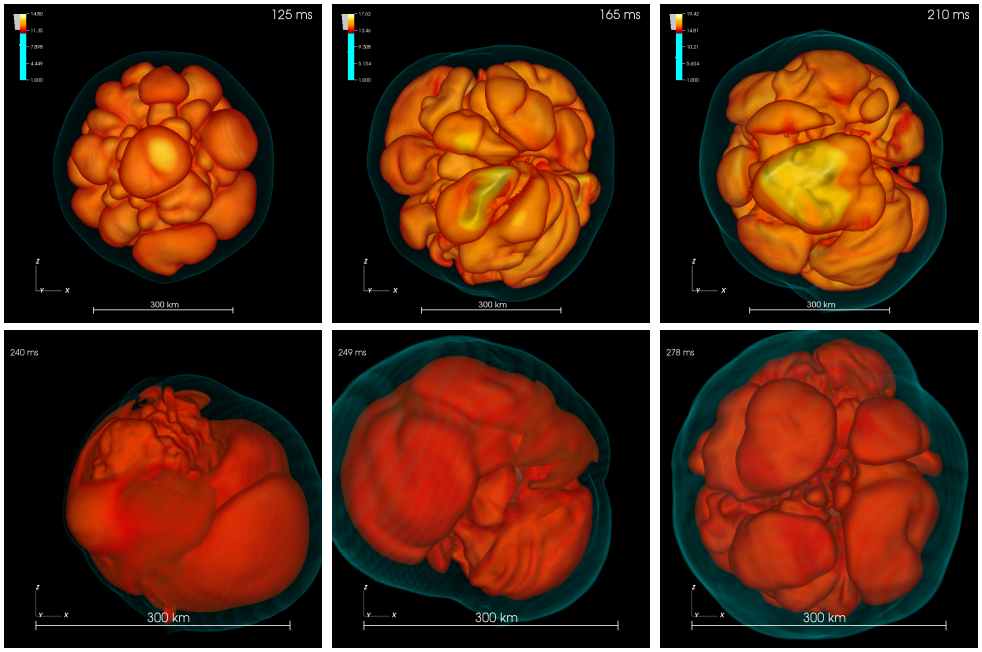

Figure 3.5: The upper row shows three post-bounce snapshots (125, 165, 210 ms p.b.) of a 3D simulation of an 11.2 $M_\odot$ star, whose postshock accretion flow is characterized by convection [30]. The lower row shows three snapshots (240, 249, 278 ms p.b.) from a 27 $M_\odot$ 3D simulation, where SASI alternates with convection-dominated periods [31]. Surfaces of constant entropy are displayed in yellow and red; the SN shock shown as a blue envelope. SASI sloshing or spiral motions show up by large-amplitude unipolar or dipolar deformations, whose orientation flips between the hemispheres on time scales of milliseconds. Figure adapted from Reference [28].

3.4 Core-collapse SNe numerical simulations

Unfortunately for this field, there is very limited experimental data for SN neutrinos, as we will discuss in the next section. Therefore, we must rely on the data provided by the numerical simulations to perform our calculations. The first simulations assumed a spherically symmetric geometry for the model, and therefore are referred as one dimensional (1D) models. Nonetheless, the current simulations are implemented on fully three dimensional (3D) models. Until now, collective oscillations have not been implemented in numerical simulations. There are some very interesting effects that have been identified in state-of-the-art simulations, which potentially could have an effect for the emitted neutrino signal and also for self-induced neutrino oscillations. For this reasons, we will proceed now to discuss them briefly.

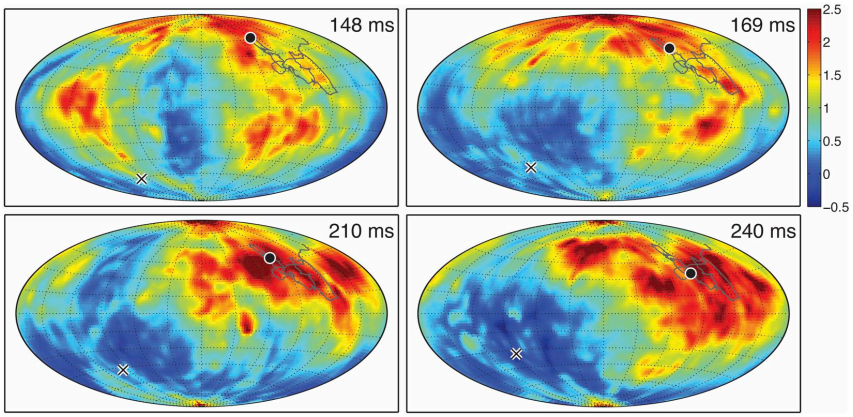

Figure 3.6: Schematic representation of the ν_e-$\bar{\nu}_e$ flux normalized by the average flux in all directions for different post-bounce times [30]. These results come from a 3D simulation of 11.2 $M_\odot$ progenitor. These figures show a dipole pattern, having an excess of ν_e in the northern hemisphere and an excess of $\bar{\nu}_e$ in the southern hemisphere. The black point shows the maximum of the dipole, and the cross the direction. The gray lines show the the path described by the dipole's maximum direction drift.

SASI

The results of 2D and 3D simulations have shown a new effect during the accretion phase of the shock wave. This effect is known as the Standing Accretion Shock Instability (SASI). It happens for stars with masses over $\sim 10\ M_\odot$, and consists on non-radial perturbations, mostly non-radial hydrodynamical instabilities. These perturbations do not allow the shock-wave front to retain an spherical shape and makes it vibrate in a dipolar motion. We show some snapshots of this effect in Figure 3.5. This effect was first noticed in a numerical simulation [32], and it was afterward analytically ratified [33]. This could potentially have an impact on the emitted neutrino spectrum by adding rapid oscillations to the fluxes [34, 35].

LESA

After performing state-of-the-art 3D simulations, including three-flavor neutrino transport, a new phenomena has appeared in the neutrino signal. This effect, known as lepton-emission self sustained asymmetry (LESA) [30], is a difference on the lepton number luminosity, i.e., the $\nu_e - \bar{\nu}_e$ luminosity, where there is a strong dipole asymmetry in the flux. This effect is shown in Figure 3.6.

The difference of the flux between the two hemispheres can be observed almost exclusively for the electron flavor, showing a difference up to 20% in the ν_e and $\bar{\nu}_e$ fluxes. The LESA effect takes place approximately 200 ms after the core's bounce, and shows a duration of about 100–150 ms during which

it remains remarkably stable. These effects seem to be a generic feature of the 3D models. Although the exact conditions for this instability to grow are still not understood, it arises from the combined effect of neutrino transport and multidimensional hydrodynamics. Even though it is still uncertain if the LESA phenomenon is a numerical artifact, if confirmed, would be extremely interesting. This would open the window for differences on the lepton number for different sectors (or different outgoing neutrino trajectories) of the SN, which can have very interesting applications.

3.5 SN 1987A

As we have discussed above, SNe emit a enormous flux of neutrinos during its collapse ($\sim 3 \times 10^{53}$ erg), this flux being as a first approximation isotropically distributed. Therefore, by simple geometric reasoning we can conclude that the flux will decrease with distance as $1/d^2$. Once again, the weakness of the neutrino coupling results in the fact that, with the current experimental sensitivities, we can only observe the neutrino footprint of SNe that are at distances less than few ~ 100 kpc.

Since the existence of the neutrino detectors, only one SN event has happened close enough to Earth to obtain a clear detection. This happened on the 23^{rd} of February of 1987, named SN 1987A. The progenitor star was located in the Large Magellanic Cloud, at a distance of approximately 50 kpc. The energies of the detected events lie in the range of tens of MeV.

At the time of SN 1987A, there were only three experiments with sufficient sensitivity to detect the emitted neutrino flux. These were Kamikande-II [36] and Irvine-Michigan-Brookhaven (IMB) [37], both of them water Cherenkov detectors, as well as the Baksan underground scintillation telescope [38]. In Figure 3.7 we show these experimental results.

Despite the reduced number of events, there are some interesting insights that can be extracted from this data. Besides information of the neutrino energies and the fluxes, the lack of a simultaneous γ-ray burst sets a constraint on the radiative decays of neutrinos [25]. Moreover, the time scale of the events (a few seconds) or, equivalently, the time scale of the cooling of the newly born neutron star can be used to constraint non-standard cooling channels created by theoretically proposed particles, such as sterile neutrinos or axions.

3.5.1 Future SN Neutrino detection

This leads one to wonder, how are the prospects of new data? There are different ways to predict the galactic SN rate, but the typical result is about three events per century [39]. In other words, every year there is a probability slightly above three percent of an event and after three years this probability rises to almost ten percent. Unfortunately, there has not been any events during the course of this work.

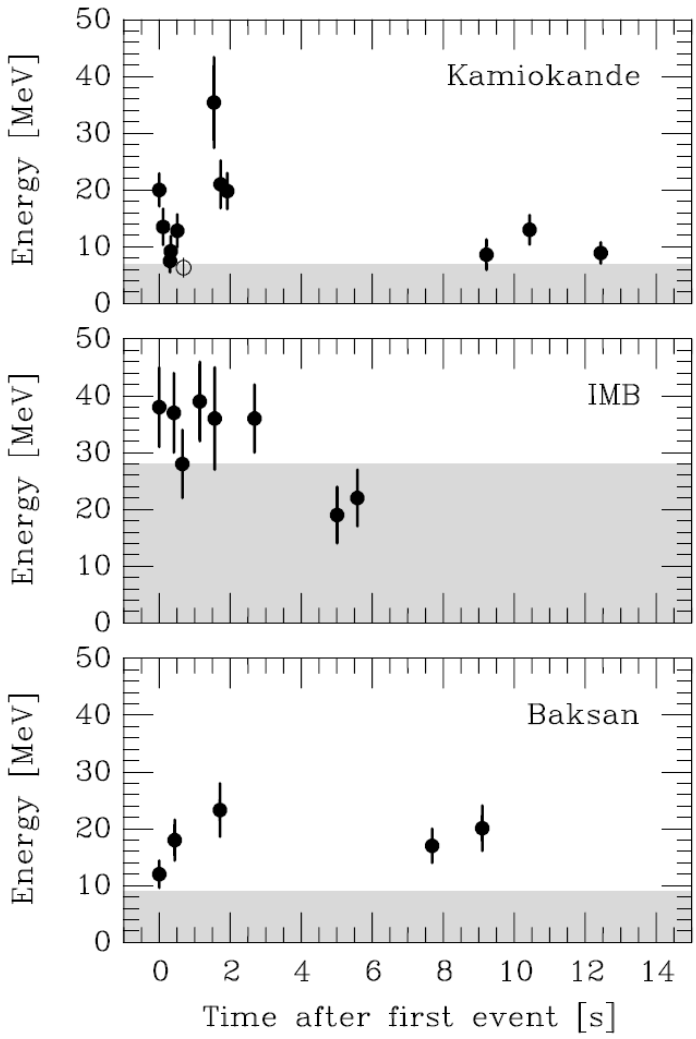

Figure 3.7: Measured neutrino signals from SN 1987A [25]. The upper, middle, and bottom panel shows the events measured by Kamiokande, IMB, and Baksan, respectively. The open dots of the Kamiokande detector are usually interpreted as background. The energies shown correspond to the secondary positrons, not the primary electron antineutrinos, produced through the process $\bar{\nu}_e + p \to n + e^+$. The clocks of the detectors are not synchronized. In the figure, the first detection in each experiment has been shifted to $t = 0$.

Nowadays, the detection possibilities for core-collapse SN neutrinos have been significantly improved, and in the event of a galactic SN, we would increase our statistics substantially when compared to the data collected from SN 1987A. For instance, the Super-Kamiokande detector is expected to detect a large number of events ($\sim 10^3$) for a core-collapse SN event at distances of around 10 kpc from Earth [40]. Moreover, other experiments such as SNO, KamLAND, LVD, MiniBooNE and Borexino could also detect signals,

although the number of events is expected to be significantly lower [41]. Moreover, the IceCube detector, an experiment located at the South Pole designed for detecting cosmic neutrinos, would detect a enormous increase in its background. This effect could be used to infer the SN luminosity curve. On the other hand, future proposed neutrino detectors like Hyper-Kamiokande and JUNO will extend our coverage and thereby increase the range of detection capabilities.

Another interesting feature of core-collapse SN neutrinos is that they decouple from the collapsing star long before photons do. Indeed, the neutrino flux of these events arrives at Earth several hours before the photon flux is observable. Therefore, if we are able to determine the direction of the incoming neutrino flux, we could direct in advance photon telescopes in order to have the best possible detection [41].

3.6 Summary

The conditions of a collapsing star, with extremely high densities, are the perfect environment for testing physics of weakly interacting particles such as neutrinos. At the same time, neutrinos play a fundamental role in SN physics. As discussed above, the neutrino reheating mechanism is believed to be responsible for a successful explosion to take place.

Neutrinos are in thermal and chemical equilibrium at the very core of the star. At some tens of kilometers from the star's center, neutrinos decouple from the plasma and begin to free-stream. This decoupling defines the neutrino sphere radius. The other crucial piece of information that we must keep in mind is that the densities are so high that the neutrinos can interact with themselves, so that these environments are suitable for self-induced neutrino oscillations.

However, there are still many questions to be answered in this field. One of the most urgent ones is that of neutrino flavor oscillations. Until now, simulations do not include neutrino flavor conversion. If flavor conversion indeed occurs, it might have an impact on the explosion mechanism. The reason for that is the non-linear nature of this phenomenon; its implementations would be highly costly in terms of computation power.

With respect to the emitted neutrino flux, we must again emphasize that it is divided into three phases: the prompt burst, the accretion phase flux, and the cooling-phase flux. The first phase emits exclusively electron neutrinos, and the second phase has a lower luminosity but emits many species obeying $F_{\nu_e} > F_{\bar{\nu}_e} > F_{\nu_x}(F_{\bar{\nu}_x})$. The last phase is the least luminous one, and all flavors are emitted equally. The energies of emitted neutrinos in all three phases are in the hundreds of MeV range

On the other hand, the neutrino signal coming from core-collapse SN can be very useful to study other theoretically proposed, weakly interacting particles, such as axions or sterile neutrinos. The idea is that such particles, if produced

in the core of the star, can provide an extra cooling channel. Unfortunately, some very interesting aspects of SN physics have not been covered in this chapter, such as nucleosynthesis, since it does not affect the neutrino signal. However, neutrinos can modify the amount of synthesized heavy nuclei.

The only experimental data, corresponding to SN 1987 A, sustains our basic theoretical understanding of core-collapse SNe explosions, but the statistics are too poor to extract precise information of the explosion mechanism. We are in desperate need for more events to investigate further all the proposed theoretical models.

Chapter 4

Kinematic equations for the neutrino field in dense media

In this chapter, we will develop the formalism to describe the kinematics of the neutrino field in a very dense medium. We will start by introducing the density matrix formalism, justifying its convenience and discussing its advantages. Then we will present the Boltzmann-like equation for the evolution of the neutrino ensemble and we will examine the different terms from the perturbative expansion. We will briefly study the two most common examples of dense environments: the Early Universe and the interior of a core-collapse SNe. Furthermore, we will discuss the consequences these environments impose on the equation of motion (EOM).

We will particularize the EOM for the SN case, and we will discuss the convenience of adopting a two flavor scheme. Under this assumption we will discuss how to change between the two neutrino mass orderings. The next section will be devoted to linearize the EOM and to introduce the concept of flavor instability. In this context, we will discuss the limit where neutrinos are massless. We conclude with a summary.

4.1 Density matrix formalism

We have devoted most of Chapter 2 to the study of neutrino oscillations in vacuum and in matter. Hitherto, the starting point has always been the Schrödinger equation. In other words, we have used the wave-function description for neutrinos. This approach is completely appropriate for the systems analyzed. Moreover, it features the advantage of being mathematically simple. However, this description ceases to be adequate when we confront the evolution of a neutrino field which is undergoing flavor mixing and simultaneously scattering with its environment. This is the typical situation in dense media, such as the interior of a collapsing star or at early stages of the universe's evolution.

In the context of dense environments, there is also another ingredient adding to the complexity of the problem. When the neutrino density is very high, neutrinos interact with the neutrino background, or, in other words, neutrinos undergo self-interactions. Under these circumstances the single-particle wave formalism is no longer an appropriate description. Instead, we have to find a framework that can account for all the effects mentioned above.

This is achieved using a mathematical framework known as density matrix formalism. We will now develop how to obtain the EOM under this framework, where we will essentially follow the discussion performed in Reference [42]. As a starting point, we will write down the momentum expansion of a left-handed neutrino field

$$\psi_L(x) = \int d\mathbf{p}(a_{\mathbf{p}}u_{\mathbf{p}} - b^\dagger_{-\mathbf{p}}v_{-\mathbf{p}})e^{i\mathbf{p}\cdot\mathbf{x}}, \tag{4.1.1}$$

where $d\mathbf{p} = d\mathbf{p}^3/(2\pi)^3$. Furthermore, $a_{\mathbf{p}}$ is the annihilation operator for negative-helicity neutrinos of momentum $\mathbf{p}$ and $b^\dagger_{\mathbf{p}}$ is the creation operator for positive-helicity antineutrinos. For a system of n flavors, $a_{\mathbf{p}}$ and $b^\dagger_{\mathbf{p}}$ are column vectors of components $a_i(\mathbf{p})$ and $b^\dagger_i(\mathbf{p})$, respectively. These operators satisfy the commutator relations $\{a_i(\mathbf{p}), a^\dagger_j(\mathbf{p}')\} = \{b_i(\mathbf{p}), b^\dagger_j(\mathbf{p}')\} = \delta_{ij}(2\pi)^3\delta^3(\mathbf{p}-\mathbf{p}')$. In the following, we will assume the massless limit, so that only left-handed interactions are present and right-handed fields can be neglected. However, in order to account for flavor mixing we need to include the neutrino mass matrix, which is non-diagonal in the interaction basis and allows for spin-flip reactions. Because these transition probabilities are proportional to the neutrino mass squared, they are small and can be neglected. These kind of effects in the SN context have been studied in References [43, 44][1].

We will now analyze the different combinations of the operators a and b. Combinations of the type $a^\dagger b^\dagger$ and ba violate lepton number by two units and correspond to creation and annihilation of neutrino pairs. These types of bilinears require an anisotropic environment and have been investigated in references [45–48]. Hence, the only bilinears necessary to describe the system are $a^\dagger a$ and $b^\dagger b$. Given an homogeneous neutrino ensemble, the system can be described by the $n \times n$ matrices

$$\begin{aligned}\langle a^\dagger_j(\mathbf{p})a_i(\mathbf{p}')\rangle &= (2\pi)^3\delta^3(\mathbf{p}-\mathbf{p}')\rho_{ij},\\ \langle b^\dagger_j(\mathbf{p})b_i(\mathbf{p}')\rangle &= (2\pi)^3\delta^3(\mathbf{p}-\mathbf{p}')\overline{\rho}_{ij},\end{aligned} \tag{4.1.2}$$

where $\rho(t, \mathbf{r}, E, \mathbf{v})$ essentially provide the classical phase-space densities. Note the inverted indexes in the r.h.s. of this equation. This is introduced to guarantee that both matrices transform equally under a unitary transformation of the from $\psi' = U^\dagger\psi U$. We can write explicitly these matrices as

$$\rho = \begin{pmatrix} \rho_{ee} & \rho_{e\mu} & \rho_{e\tau} \\ \rho_{\mu e} & \rho_{\mu\mu} & \rho_{\mu\tau} \\ \rho_{\tau e} & \rho_{\tau\mu} & \rho_{\tau\tau} \end{pmatrix}, \quad \overline{\rho} = \begin{pmatrix} \overline{\rho}_{ee} & \overline{\rho}_{e\mu} & \overline{\rho}_{e\tau} \\ \overline{\rho}_{\mu e} & \overline{\rho}_{\mu\mu} & \overline{\rho}_{\mu\tau} \\ \overline{\rho}_{\tau e} & \overline{\rho}_{\tau\mu} & \overline{\rho}_{\tau\tau} \end{pmatrix}. \tag{4.1.3}$$

[1]The authors of Reference [44] have claimed that, under some circumstances, these helicity flips can be resonantly enhanced.

The diagonal terms of this matrix are the occupation numbers of the flavor eigenstates, whereas the off diagonal ones represent the correlations between different flavors and therefore contain information about phases. In case we want to study the non-degenerate limit with pure states, this formalism is completely analogous to the single-particle wave function description used for the neutrino oscillations's discussion. However, when the coherence between flavors starts to play a role, the density matrix prescription will be the appropriate tool to study the flavor evolution of the neutrino field.

4.2 Generalized equations of motion

4.2.1 Liouville equation

We will now examine the EOM for the density matrix. The evolution of ρ and $\bar{\rho}$ is obtained as a perturbative expansion in the Heisenberg formalism, assuming the appropriate Hamiltonian of weak interactions. Considering up to the second order in the perturbation expansion, the EOM for the density matrix is

$$iv\partial\rho = [\mathrm{H}^{\mathrm{vac}}, \rho] + [\mathrm{H}^{\mathrm{ref}}, \rho] + \mathcal{C}(\rho), \tag{4.2.1}$$

where we have used the covariant notation such that $v\partial = v^{\mu}\partial_{\mu} = \partial_t + \mathbf{v}\cdot\nabla_{\mathbf{r}}$. Moreover, the four velocity vector is $v = (1, \mathbf{v})$. We will now explain the different terms of the r.h.s. of this equation.

Vacuum term

The first term on the r.h.s. is the term responsible for the vacuum oscillations. It is very familiar to us since it was the subject of study when we studied neutrino oscillations in Chapter 2. For the rest of the dissertation we will work in the weak-interaction basis, and in this basis this term is non-diagonal.

Refractive term

The second term in the r.h.s of Equation 4.2.1 is the *refractive potential* term. Because the refractive term comes from the first order of the perturbative expansion, it is proportional to G_{F}. This element receives contributions from two different terms, namely

$$\mathrm{H}^{\mathrm{ref}} = \mathrm{H}^{\mathrm{m}} + \mathrm{H}^{\nu\nu}. \tag{4.2.2}$$

H^{m} is the potential that describes the interaction of neutrinos with the surrounding matter. This is the term responsible of the already discussed MSW effect. There is a second contribution given by $\mathrm{H}^{\nu\nu}$. This term arises from the neutrino's interactions with the surrounding neutrinos, or, in other words, neutrinos interacting with each other. Therefore it is referred to as the self-interaction term. Furthermore, this term contains ρ and therefore makes the equations non-linear.

Collision term

The last term on the r.h.s. of Equation 4.2.1 is called the collision term. This term arises from the second order of the perturbative expansion, and therefore is proportional to G_{F}^2. This terms accounts for processes such as annihilations and momentum exchanging processes of neutrinos with either the leptonic and the neutrino background. In particular it contains the scattering processes with the medium of the form $\nu_{\mathbf{p}} X \to \nu_{\mathbf{p}'} X'$ (where X is a particle of the surrounding medium), production and absorption by CC processes of the type: $X \to X' \nu_{\mathbf{p}}$, $X \nu_{\mathbf{p}} \to X'$, and analogous processes for antineutrinos. Moreover, the NC pair processes $\nu_{\mathbf{p}} \bar{\nu}'_{\mathbf{p}} \to X X'$ and $X X' \to \nu_{\mathbf{p}} \bar{\nu}_{\mathbf{p}'}$ are also included in this term.

4.3 Two highly dense environments: The Early Universe and core-collapse SNe

The density matrix formalism will be very useful for two extreme environments: the Early Universe and the interior of core-collapse SNe. In both cases, these environments are the perfect laboratory to study flavor conversion under high-density conditions, involving refractive effects from charged leptons and collisional damping. Furthermore, the neutrino background is so dense that self-interactions occur and can play a crucial role in the evolution of the system. Moreover, the non-linear nature of this interaction translates on collective effects having unexpected and sometimes contraintuitive behaviors. We will now briefly describe the main characteristics of these two environments.

4.3.1 The Early Universe

The Early Universe is a textbook example of dense environment. This environment is, in a good approximation, spatially homogeneous. Moreover, in the Early Universe there were almost equal numbers of baryons and antibaryons with an asymmetry fixed by observations to be $\sim 10^{-10}$ as well as charge neutrality, so the matter refraction term can be neglected. Nonetheless, the self-interaction term will be very important because of the high densities. Unlike other environments, there is no predominant streaming direction, so neutrinos travel in all directions. Another crucial feature in this scenario is that, due to the temperatures and energies, in combination with the multi-directional flux, the collision term needs to be considered. This main effect of the collision term is to damp the off diagonal terms of the density matrix $\rho_{\mathbf{p}}$, which pushes the diagonal terms towards their equilibrium distributions.

4.3.2 Interior of core-collapse SNe

In the case of SNe, we will study the evolution of the neutrinos that have been emitted from the neutrino sphere and are streaming outwards from the star.

From Chapter 3 we know that the range of energies for these neutrinos is of the order of tens of MeV. In other words, the neutrinos under study will be affected only by forward scattering and the collision term can be safely neglected. It is of course true that inside the neutrino sphere collisions will play an important role, but for the purposes aimed in this dissertation, we will not have to worry about what happens inside the neutrino sphere. To sum up, among all terms on the r.h.s. of Equation 4.2.1, we are just left with $\mathrm{H}^{\mathrm{vac}}$ and $\mathrm{H}^{\mathrm{ref}}$.

Due to the current-current interactions that neutrinos experience, the direction of motion is a fundamental quantity, which is represented by the vector $\mathbf{v} = \mathbf{p}/|\mathbf{E}|$. Since we are working with ultrarelativistic neutrinos, the velocity vector will lie within the unit sphere, which implies $|\mathbf{v}| = 1$. In the following, we will use the so-called "flavor isospin convention", meaning that we will refer to antineutrinos as the negative E modes of the diagonal entries of the matrix of densities. In the free streaming regime, the system can be successfully described by means of a Liouville equation of the form [42]

$$iv\partial\rho = [\mathrm{H}^{\mathrm{vac}} + \mathrm{H}^{\mathrm{ref}}, \rho], \tag{4.3.1}$$

where the Hamiltonian matrix is

$$\mathrm{H}^{\mathrm{vac}} + \mathrm{H}^{\mathrm{ref}} = \frac{M^2}{2E} + \sqrt{2}G_{\mathrm{F}}\left(v\mathrm{N} + \int d\Gamma' vv'\rho'\right), \tag{4.3.2}$$

where the phase space integration explicitly is $\int d\Gamma' = \int_{\infty}^{\infty} dE' E'^2 \int d\mathbf{v}'/(2\pi)^{\mathbf{3}}$. The primed quantity inside the integrals refers to the energy-angle dependencies, so that $\rho' = \rho'(t, \mathbf{r}, E', \mathbf{v}')$. The first term in Equation 4.3.1 is the vacuum oscillation frequency, whereas the second term is the matter term. Moreover, N is the lepton current produced by the matter background, and it is explicitly written as $N_0 = \mathrm{diag}(n_e - n_{\bar{e}}, n_\mu - n_{\bar{\mu}}, n_\tau - n_{\bar{\tau}})$.

We have to pay special attention to the term inside the integral or the self-interacting term. First of all, the factor $vv' = (1 - \mathbf{v}\mathbf{v}')$ in the integration evidences the current-current nature of the weak interactions. On the other hand, in order to calculate this term, we have to integrate over all neutrino modes of the ensemble. This becomes evident after we substitute Equation 4.3.2 in Equation 4.3.1, which exposes the non-linearity induced by neutrino self-interactions.

4.4 Two flavor scheme

We will restrict the rest of the analysis to a two flavor scheme, where only the flavors ν_e and ν_x are considered, and ν_x is a linear combination of the μ and τ flavors. There are two main arguments supporting this choice. First of all, for the neutrino energies present in SN-type environments, the only mass difference capable of producing appreciable effects is the $\Delta m^2_{\mathrm{atm}}$, since for this mass difference we will have a $\lambda_{\mathrm{osc}} \sim 30$ km. Second, the neutrino

species contained in the linear combination x undergo the same interactions in matter as we have discussed in Chapter 2. This implies that these species have the same neutrino sphere and consequently the same angular distributions for neutrinos and antineutrinos. This point, as we will discuss in Chapter 5, plays a crucial role.

The physically motivated two-flavor scheme features the additional advantage that it reduces considerably the mathematical complexity of the equations. Under this paradigm we can use unitary two-dimensional flavor vectors to describe our system. The vector $\vec{B}$ points in the direction of the mass, and the vector $\vec{L}$ points in the direction of the weak interaction in flavor space. The relative angle between these two vectors is twice the vacuum mixing angle, i.e., 2Θ, which is a small quantity. The vacuum oscillation frequency will be denoted as ϖ, and is explicitly

$$\varpi = \frac{\Delta m^2_{\rm atm}}{2E} = 0.63 \text{ km}^{-1} \left(\frac{10 \text{ MeV}}{E}\right). \tag{4.4.1}$$

Therefore, in the following, we will label the neutrino modes using ϖ instead of the energy E. Using these vectors, the Hamiltonian of Equation 4.3.2 can be expressed as

$$\mathsf{H} = \frac{1}{2}\left(\varpi\vec{B} + v\Lambda\vec{L}\right)\cdot\vec{\sigma} + \sqrt{2}G_{\rm F}\int d\Gamma' vv'\rho', \tag{4.4.2}$$

where $\vec{\sigma}$ are the Pauli matrices

$$\sigma_x = \begin{pmatrix} 0 & 1 \\ 1 & 0 \end{pmatrix}, \quad \sigma_y = \begin{pmatrix} 0 & -i \\ i & 0 \end{pmatrix}, \quad \sigma_z = \begin{pmatrix} 1 & 0 \\ 0 & -1 \end{pmatrix}, \tag{4.4.3}$$

and we have used the Einstein summation convention for the product $v\Lambda = v_\mu\Lambda^\mu$, where $\Lambda^\mu = \sqrt{2}G_{\rm F}N_e^\mu$. Because the object of study is the SN interior, the four vector N_e^μ is the electron minus positron flux densities, since in these environments there are negligible amounts of any other charged lepton. This product expresses in a very intuitive way the effect of the matter background: it is a rotation of the flavor basis.

4.4.1 Mass Ordering

Although we have adopted the two-flavor scheme, there is still one neutrino mass difference in our equations. Moreover, as we have discussed in Chapter 2, the sign of this mass difference has not been measured so far. This implies that our equations are sensitive to the mass ordering. The EOM we have derived corresponds to the IO. Nevertheless, NO is also a physically motivated possibility, so the NO should also be studied. Therefore, our equations must be capable of being modified to include the NO case. We will now explain how to do so. Following the convention introduced in Chapter 2, the NO corresponds to a negative Δm^2, but we can also keep this parameter positive

if we introduce a minus sign in the r.h.s. of Equation 4.4.2. The change of IO to NO is achieved by changing $\vec{B} \to -\vec{B}$, and therefore our EOM are perfectly valid to study the NO case as well. Finally, we must point out that the ordering question is no longer relevant if we work under the assumption of ϖ equal to zero, i.e., the massless limit.

4.5 Linearization

As we have already pointed out, the main difficulty when dealing with neutrinos self-interactions is caused by the fact that neutrinos couple to all other neutrino modes. This effect makes the problem not only very challenging in computational terms, but also very difficult to grasp an intuition of the physics of the system. However, there is another approach to deal with these equations known as linearized stability analysis [49].

Before starting this discussion, it is very convenient to manipulate our equations to obtain more manageable expressions. First of all, we express the mean-field matrices in a normalized form

$$\rho = \frac{f_{\nu_e} + f_{\nu_x}}{2}\mathbb{1} + \frac{f_{\nu_e} - f_{\nu_x}}{2}\ \mathsf{S}, \tag{4.5.1}$$

with the matrix S defined as

$$\mathsf{S} = \begin{pmatrix} s & S \\ S^* & -s \end{pmatrix}, \tag{4.5.2}$$

where s is real and S is complex, and they fulfill the relation $s^2 + |S|^2 = 1$. Since we are in the two flavor scheme, this matrix structure can be expressed in a very intuitive manner by means of three dimensional flavor vectors, known as *polarization vectors*, which are explained in more detail in Appendix A. By analyzing Equation 4.5.1, it is easy to see that the first term is diagonal in flavor space. This means that this term is not affected by flavor oscillations. Therefore, when studying the flavor evolution of the system, we can simply ignore this term. For the term sensitive to flavor oscillations, we introduce the notation for the difference between the ν_e and ν_x distributions in the form

$$G = \sqrt{2}G_{\mathrm{F}} \times \begin{cases} f_{\nu_e}(E, \mathbf{v}) - f_{\nu_x}(E, \mathbf{v}), & E > 0 \\ -f_{\bar{\nu}_e}(E, \mathbf{v}) + f_{\bar{\nu}_x}(E, \mathbf{v}), & E < 0. \end{cases} \tag{4.5.3}$$

Now, using this definition, the EOM for the two-flavor scheme reduces to the form

$$iv\partial\ (G\mathsf{S}) = G[\mathsf{H}, \mathsf{S}], \tag{4.5.4}$$

and the Hamiltonian is explicitly

$$\mathsf{H} = \tfrac{1}{2}(\varpi\vec{B} + v\Lambda\vec{L}) \cdot \vec{\sigma} + \sqrt{2}G_{\mathrm{F}} \int d\Gamma' vv' G'\mathsf{S}'. \tag{4.5.5}$$

Homogeneous and stationary neutrino distribution

In a completely general approach, the neutrino distribution function G depends on the space-time coordinates. However, locally the changes in the neutrino field occur very fast compared to the local environment time scales. Therefore we can drop the space-time dependence of the function G, leaving only the energy and direction dependence, such that $G = G_{\omega,\mathbf{v}}$. The neutrino phase-space distributions $f_{\nu_e}(\omega, \mathbf{v})$ represent now the initially prepared system. The space-time evolution of the system is encoded in S given by Equation 4.5.2. Under these assumptions, Equation 4.5.4 is now

$$iv\partial\mathsf{S} = [\mathsf{H}, \mathsf{S}], \tag{4.5.6}$$

where the Hamiltionan matrix is the same of Equation 4.5.5.

4.5.1 Linearized stability analysis

Now that we have arrived at Equation 4.5.6 we can explain the linearized stability analysis approach. The idea is the following: we consider that the system is initially diagonal in flavor space, i.e., the non-diagonal terms S are zero. Now, since the length scale where oscillations occur is so fast compared to the MSW effect, we can safely neglect it. The idea is that the dense environment provides a large matter effect ($v\Lambda \gg \omega$). Under this condition, we can move to a co-rotating frame where $\vec{B}$ and $\vec{L}$ are collinear and take the mixing angle in matter to be infinitely small, so that flavor mixing plays no longer a role. This approximation becomes exact in the limit $\varpi \to 0$.

With these assumptions, and since we have considered initial, vanishing S elements, the only way to trigger flavor conversion is through the action of neutrino-neutrino interaction. The next step is indeed to study if self-interactions can develop a small initial perturbations to grow exponentially, i.e., to study if the system is unstable. This approach is referred to as linearized stability analysis. To this end, we adopt the limit

$$s = \sqrt{1 - |S|^2} = 1, \tag{4.5.7}$$

so that the EOM becomes

$$iv\partial S = (\varpi + v\Lambda + v\Phi)S - v \int d\Gamma' v' G'(S - S'). \tag{4.5.8}$$

Let's now carefully examine the linearized EOM. We have gained the advantage that, when studying the evolution of a given neutrino mode, it does no longer couple to all other modes. Furthermore, we can pull out from the integral the term proportional to vS, and defining the quantity

$$\Phi = \int d\Gamma G v, \tag{4.5.9}$$

which is a four vector that contains the information of the neutrino-neutrino refraction. This neutrino-induced term is analogous to the matter-induced refraction term Λ. Moreover, Φ contains a scalar component, expressed explicitly as

$$\Phi_0 = \sqrt{2}G_F[(n_{\nu_e} - n_{\bar{\nu}_e}) - (n_{\nu_x} - n_{\bar{\nu}_x})]. \tag{4.5.10}$$

By adopting this notation, the EOM will then look like

$$iv\partial S = \big[\varpi + v(\Lambda + \Phi)\big]S - v\int d\Gamma' v' G' S'. \tag{4.5.11}$$

where the factor $v(\Lambda + \Phi) = \Lambda_0 + \Phi_0 - \mathbf{v}(\mathbf{\Lambda} + \mathbf{\Phi})$ stands for the energy shift introduced by the matter *and* neutrinos. In fact, all the works in the linearized stability analysis literature are particular cases of Equation 4.5.11. The different studies consist basically of different assumptions for the neutrino energy and velocity distributions, the boundary and/or initial conditions, and asymmetries of the solutions.

Even though the linear approach is a very useful tool to analyze SN dynamics, one has to be aware of its limitations. When solving the system using the fully coupled EOM, the solutions can undergo instability enhancements due to non-linearities, as some authors have pointed out [50, 51].

4.5.2 Linearized equations in the massless limit

During the development of this thesis, we will find situations were the system exhibits very interesting solutions in the limit where neutrino masses are zero. In the language of linearized stability analysis, the massless limit corresponds to the vacuum oscillation frequency being zero, which makes the mass difference also zero. Therefore, it is very convenient to adapt the linearized EOM given by 4.5.11 to the limit $\varpi \to 0$, such that

$$iv\partial S = (\Lambda + \Phi)S - v\int d\Gamma' v' G' S'. \tag{4.5.12}$$

From this equation, we can infer another consequence of adopting the massless limit: there is no longer an energy E dependence in the EOM, but rather the neutrino modes are entirely described by the velocity $\mathbf{v}$ or, more precisely, its associated angle. Furthermore, the same applies to neutrinos and antineutrinos, so the only relevant quantity we need to care about is the angle distribution of the electron lepton number (ELN) carried out by neutrinos, which we parametrize as

$$G_{\mathbf{v}} = \sqrt{2}G_{\mathrm{F}}\int_0^\infty \frac{dEE^2}{2\pi^2}[f_{\nu_e}(E,\mathbf{v}) - f_{\bar{\nu}_e}(E,\mathbf{v})]. \tag{4.5.13}$$

4.6 Summary

We have introduced the density matrix formalism to study the flavor conversion of the neutrino field in dense media. We have also extended the perturbative equation for the interaction of the neutrino field. We have then studied the most illustrating examples of dense environments. The first one, the Early Universe, has the particularity that besides the neutrino self-interaction effects, neutrino collision terms have to be taken into account and produces flavor decoherence. We have also discussed the core-collapse SN case, where the refraction term will be dominating, and therefore we can neglect the collision terms.

We have then particularized our analysis to the Liouville equation, since it provides a description of the neutrino field at the refraction level. Moreover, we have assumed a two flavor scenario, since it simplifies the equations but still captures the important physics of our system.

Because of the non-linear nature of the equations makes them very difficult to solve, we have proceeded to linealize the EOM, and we have explained the linearized stability analysis approach. In the last section of the present chapter we have developed the linearized EOM for the massless limit and we have introduced the definition of electron number density carried by neutrinos.

Chapter 5

Dispersion Relation

At the end of Chapter 4 we arrived at a linearized equation of motion (EOM) for the neutrino field in the forward-scattering regime. Unfortunately, it is almost impossible to solve this seven-dimensional problem without making further simplifications. To this end, as a next step, we apply a Fourier transform to the EOM, which will lead us directly to the dispersion relation. In the rest of this chapter we will study in more detail the implications of the dispersion relation, using the two neutrino beam example as a benchmark. We will start with a very simple setup, and we will be gradually adding more elements until we arrive at the asymmetric colliding neutrino beam example. During the study of this example we will encounter for the first time fast flavor conversion phenomenon, where the growth rate of the flavor conversion is proportional to the neutrino-neutrino interaction. Moreover, we will use the colliding beams setup to understand the insights of the dispersion relation, and to that end we will discuss the different forbidden bands or regions of the parameter space where we have only imaginary solutions or no solution at all. As we will see, the shape of these regions can be very different, and for different scenarios we will require different conditions to solve our system. We also discuss the necessity of dealing with the boundary conditions. We conclude the chapter with a summary.

5.1 Fourier Transform

At the end of last chapter we arrived at a linearized EOM for the flavor evolution in dense media. Although we have done several simplifications, the EOM is still not directly solvable. The problem with Equation 4.5.11 lies in the fact that we have to deal with a seven-dimensional phase-space (three spatial coordinates, three velocity components and time), which is not directly tractable. Therefore, we need to find a manner of reducing the dimensionality of the problem. Traditionally, this was achieved by assuming different symmetries in the system. These assumptions included stationarity, the use of spheri-

cal symmetry, or homogeneity in the perpendicular direction. However, this approach has the downside that these assumptions might induce unphysical results. There is another approach to achieve this goal. In order to solve the equation 4.5.11, we can use a plane wave ansatz of the form

$$S_{E,v} = Q_{v,E} e^{-i(\Omega t - \mathbf{K}\cdot\mathbf{r})}, \tag{5.1.1}$$

which can be expressed in a more compact way by introducing $K = (\Omega, \mathbf{K})$, and therefore $Kr = \Omega t - \mathbf{K}\cdot\mathbf{r}$. This corresponds to a Fourier transform (FT), which makes this system mathematically easier to work with. We are in the linearized regime, which also implies that the different Fourier modes are decoupled from each another. So, introducing the ansatz given by Equation 5.1.1 in Equation 4.5.11 and rearranging the terms, we obtain

$$(\Omega - \mathbf{v}\cdot\mathbf{K})Q = (\varpi + v(\Lambda + \Phi))Q - v\int d\Gamma' v' G' Q'. \tag{5.1.2}$$

From this point on, we will no longer write explicitly the dependencies on E and v. We have assumed that the matter potential Λ is not affected by the FT. In other words, we have assumed that the matter background is not space-time dependent on the scales considered, which is a very reasonable assumption. Additionally, Equation 5.1.2 can be expressed in a more compact form as

$$(vk - \varpi)\, Q = v\int d\Gamma' v' G' Q', \tag{5.1.3}$$

where we have introduced the four-vector $k = (\omega, \mathbf{k})$, whose components are

$$\omega = \Omega - \Lambda_0 - \Phi_0, \tag{5.1.4}$$

$$\mathbf{k} = \mathbf{K} - \mathbf{\Omega} - \mathbf{\Lambda}, \tag{5.1.5}$$

respectively. Note that ω is not the vacuum oscillation frequency, which is denoted by the parameter ϖ. It is important to highlight that the FT has simplified our EOM to the point where we are essentially left with an eigenvalue equation for the flavor modes. Instead of solving this equation directly, in the next sections we will manipulate it to get a deeper understanding of the physics governing the system.

5.2 Dispersion Relation

By carefully analyzing Equation 5.1.3, we observe that the r.h.s. corresponds to a four-vector, whose dependence is restricted to the mode p, but is independent of the neutrino phase-space variables. We will refer to this four-vector as a. In order to find the eigenvalues of the flavor field Q, we define the eigenfunction

$$Q = \frac{va}{\omega - \varpi - \mathbf{v}\cdot\mathbf{k}}, \tag{5.2.1}$$

which we introduce in both sides of equation Equation 5.1.3, leading us to

$$va = v \int d\Gamma' \; G' \; \frac{v'(v'a)}{\omega' - \varpi' - \mathbf{v}' \cdot \mathbf{k}}. \tag{5.2.2}$$

This equation can be rewritten in the form

$$v^\alpha \left(\eta_{\alpha\beta} - \int d\Gamma' \; G' \; \frac{v'_\alpha v'_\beta}{\omega' - \varpi' - \mathbf{v}' \cdot \mathbf{k}} \right) a^\beta = 0, \tag{5.2.3}$$

where we have used $\eta_{\alpha\beta} = \text{diag}(\,1, -1, -1, -1)$, the usual metric tensor. On the other hand, the quantity inside the brackets can be used to define the "polarization tensor" as

$$\Pi^{\mu\nu} = \eta^{\mu\nu} - \int d\Gamma \; G \; \frac{v^\mu v^\nu}{\omega - \varpi - \mathbf{v} \cdot \mathbf{k}}. \tag{5.2.4}$$

Equation 5.2.3 must be fulfilled for every mode of the neutrino field, i.e., for every $v = (1, \mathbf{v})$. However, as we have mentioned above, a does not depend on v, so we have found four linearly independent equations for the four unknown parameters $a^\mu = (a_0, \mathbf{a})$.

Nontrivial solutions exist only if the determinant of the 4×4 matrix vanishes. After dropping the primes from the integration variables, the determinant is

$$\left\| \eta - \int d\Gamma \, G \, \frac{v \otimes v}{\omega - \varpi - \mathbf{v} \cdot \mathbf{k}} \right\| = 0 \, . \tag{5.2.5}$$

Here, $v \otimes v$ is a 4×4 matrix with the components $v_\alpha v_\beta$, explicitly given by

$$v \otimes v = \begin{pmatrix} 1 & -v_x & -v_y & -v_z \\ -v_x & v_x v_x & v_x v_y & v_x v_z \\ -v_y & v_y v_x & v_y v_y & v_y v_z \\ -v_z & v_z v_x & v_z v_y & v_z v_z \end{pmatrix} . \tag{5.2.6}$$

For convenience, we will formulate this product using spherical coordinates, obtaining

$$v \otimes v = \begin{pmatrix} 1 & -\mathrm{s}_\theta \mathrm{c}_\varphi & -\mathrm{s}_\theta \mathrm{s}_\varphi & -\mathrm{c}_\theta \\ -\mathrm{s}_\theta \mathrm{c}_\varphi & \mathrm{s}^2_\theta \mathrm{c}^2_\varphi & \mathrm{s}^2_\theta \mathrm{s}_\varphi \mathrm{c}_\varphi & \mathrm{s}_\theta \mathrm{c}_\theta \mathrm{c}_\varphi \\ -\mathrm{s}_\theta \mathrm{s}_\varphi & \mathrm{s}^2_\theta \mathrm{s}_\varphi \mathrm{c}_\varphi & \mathrm{s}^2_\theta \mathrm{s}^2_\varphi & \mathrm{s}_\theta \mathrm{c}_\theta \mathrm{s}_\varphi \\ -\mathrm{c}_\theta & \mathrm{s}_\theta \mathrm{c}_\theta \mathrm{c}_\varphi & \mathrm{s}_\theta \mathrm{c}_\theta \mathrm{s}_\varphi & \mathrm{c}^2_\theta \end{pmatrix} , \tag{5.2.7}$$

where θ is the zenith angle, φ is the azimuth angle, and we use the notation $\mathrm{s}_\theta = \sin\theta$, $\mathrm{s}_\varphi = \sin\varphi$ and so on.

Notice that we have considered the contra-variant four-vector $a^\mu = (a_0, +\mathbf{a})$ as our set of unknown amplitudes to avoid any minus signs. Consequently, $v \otimes v$ is constructed from the covariant components, i.e., from $v_\mu = (1, -\mathbf{v})$, explaining the minus signs in the mixed space-time components of $v \otimes v$.

On the other hand, Equation 5.2.5 can be expressed in a more elegant way using the polarization vector introduced in equation 5.2.4, which lead us to

$$\Pi^{\mu\nu} a_\nu = 0, \tag{5.2.8}$$

which has non-trivial solutions whenever we fulfill the condition $\det[\Pi^{\mu\nu}] = 0$. Lets now carefully analyze the implications of Equation 5.2.8. This equation will give the values of the four-vector k which are compatible with plane-wave solution for the flavor modes of the neutrino field. In other words, it prescribes a relation for the wave number of the flavor modes with its frequency. It is therefore a **dispersion relation** (DR). Note that this relation refer to the wave number vector $\mathbf{k}$ and not uniquely to its module, so its direction dependent.

5.3 Axial symmetry

In order to apply our EOM to specific examples, we are compelled to introduce some simplifications by means of symmetry assumptions. The first step consist of considering that the neutrino velocity distribution is axially symmetric with respect to some direction. This assumption does not exclude that there are individual neutrinos going in other directions, but the ensemble as a whole moves in this direction. In the context of SNe environments, we can associate this direction with the radial one. From now on, we will refer to the direction of the neutrino flux as the z-direction. Therefore, the neutrino distribution function $G_{E,\mathbf{v}}$ depends exclusively on the parameter $v_z = \cos(\theta)$ and no longer on φ. Moreover, we assume that the matter distribution is also axially symmetric, although there might still be a non-vanishing current in the radial direction. We must however highlight that this assumption does not imply that the solution for S obeys the same symmetries: spontaneous breaking of these symmetries is indeed one of the defining features of this type of systems. In this situation there is no prior special direction in the x-y-plane, which is the transverse plane relative to the radial direction. However, axial symmetry is broken by those solutions which include a wave vector $\mathbf{k}_\perp$ in the transverse plane. Without loss of generality we take $\mathbf{k}_\perp$ to define what we call the x-direction. After this assumptions have been taken, the DR Equation is

$$\left\| \eta - \int d\Gamma \, \frac{G_{E,\theta}}{\omega - \varpi + \mathrm{c}_\theta \mathbf{k}_z + \mathrm{s}_\theta \mathrm{c}_\varphi \mathbf{k}_x} \begin{pmatrix} 1 & -\mathrm{s}_\theta \mathrm{c}_\varphi & 0 & -\mathrm{c}_\theta \\ -\mathrm{s}_\theta \mathrm{c}_\varphi & \mathrm{s}_\theta^2 \mathrm{c}_\varphi^2 & 0 & \mathrm{s}_\theta \mathrm{c}_\theta \mathrm{c}_\varphi \\ 0 & 0 & \mathrm{s}_\theta^2 \mathrm{s}_\varphi^2 & 0 \\ -\mathrm{c}_\theta & \mathrm{s}_\theta \mathrm{c}_\theta \mathrm{c}_\varphi & 0 & \mathrm{c}_\theta^2 \end{pmatrix} \right\| = 0 \,. \tag{5.3.1}$$

Moreover, this equation can be separated in two sets of independent equations, consisting of a 3×3 matrix

$$\left\| \begin{pmatrix} 1 & 0 & 0 \\ 0 & -1 & 0 \\ 0 & 0 & -1 \end{pmatrix} - \int d\Gamma \frac{G_{E,\theta}}{\omega - \varpi + \mathrm{c}_\theta \mathbf{k}_z + \mathrm{s}_\theta \mathrm{c}_\varphi \mathbf{k}_x} \begin{pmatrix} 1 & -\mathrm{s}_\theta \mathrm{c}_\varphi & -\mathrm{c}_\theta \\ -\mathrm{s}_\theta \mathrm{c}_\varphi & \mathrm{s}_\theta^2 \mathrm{c}_\varphi^2 & \mathrm{s}_\theta \mathrm{c}_\theta \mathrm{c}_\varphi \\ -\mathrm{c}_\theta & \mathrm{s}_\theta \mathrm{c}_\theta \mathrm{c}_\varphi & \mathrm{c}_\theta^2 \end{pmatrix} \right\| = 0\,, \tag{5.3.2}$$

whereas the second one is a linear equation

$$\left\| 1 + \int d\Gamma \frac{G_{E,\theta}\ \mathrm{s}_\theta^2 \mathrm{s}_\varphi^2}{\omega - \varpi + \mathrm{c}_\theta \mathbf{k}_z + \mathrm{s}_\theta \mathrm{c}_\varphi \mathbf{k}_x} \right\| = 0\,. \tag{5.3.3}$$

5.4 Homogeneous transverse direction

We now particularize Equation 5.3.1 for the case where the transverse direction is homogeneous, which mathematically can be also interpreted as taking k_x to be zero. In order words, we seek solutions that only vary in the z (radial) direction. In that sense, we are in a subset of solutions of the most general equation, but nonetheless very interesting from the physical point of view. Furthermore, the simplification of the denominator in the eigenvalue equations makes the problem more tractable mathematically speaking. Indeed, we can now perform all the $\int_{-\pi}^{\pi} d\varphi/2\pi$ integrations, such that

$$\frac{1}{2\pi}\int_{-\pi}^{+\pi} \mathrm{c}_\varphi^2 d\varphi = \frac{1}{2\pi}\int_{-\pi}^{+\pi} \mathrm{s}_\varphi^2 d\varphi = 1/2, \tag{5.4.1}$$

and $\int_{-\pi}^{+\pi} \mathrm{c}_\varphi d\varphi = 0$. It is important to highlight that the phase integrals are now redefined, being explicitly

$$\int d\Gamma = \int_{-\infty}^{+\infty} E^2 dE \int_{-1}^{+1} \frac{d\mathrm{c}_\theta}{(2\pi)^2}. \tag{5.4.2}$$

5.4.1 Axial-symmetric and axial-breaking equations

By performing the φ integrations, our problem reduces its complexity. Equation 5.3.2 reduces to a 2×2 matrix, and corresponds to the 00, $0z$, $z0$ and zz positions, being

$$\left\| \begin{pmatrix} 1 & 0 \\ 0 & -1 \end{pmatrix} + \int d\Gamma \frac{G_{E,\theta}}{\omega - \varpi + \mathrm{c}_\theta \mathbf{k}_z} \begin{pmatrix} 1 & -\mathrm{c}_\theta \\ -\mathrm{c}_\theta & \mathrm{c}_\theta^2 \end{pmatrix} \right\| = 0\,, \tag{5.4.3}$$

which only involve the coefficients a_0 and a_z. In other words, this is the equation corresponding the axially symmetric solutions. On the other hand, the second, scalar Equation 5.3.3 reduces to

$$1 + \frac{1}{2}\int \frac{G_{E,\theta}\ \mathrm{s}_\theta^2}{\omega - \varpi + \mathrm{c}_\theta \mathbf{k}_z} = 0, \tag{5.4.4}$$

where the solutions are proportional to the coefficients a_x and a_y, or, equivalently, to c_φ and s_φ. Therefore, this solution corresponds to the axially breaking one.

At this point, it is very convenient to introduce dimensionless quantities which have been used in the literature of this field because they simplify our equations in a very convenient manner. First of all, the neutrino-neutrino interaction strength is given by

$$\mu = \sqrt{2} G_{\mathrm{F}} \ (n_{\nu_e} + n_{\bar{\nu}_e}). \tag{5.4.5}$$

On the other hand, the neutrino asymmetry is defined as

$$\epsilon = \int d\Gamma \ G, \tag{5.4.6}$$

and the neutrino flux is

$$\phi = \int d\Gamma \ G \ v, \tag{5.4.7}$$

In terms of this newly introduced variables, the axially symmetric, perpendicularly homogeneous scenario implies that the neutrino-neutrino current can be expressed as

$$\Phi = (\Phi_0, 0, 0, \Phi_z) = \mu(\epsilon, 0, 0, \phi), \tag{5.4.8}$$

where ϕ measures the lepton flux in the radial direction.

5.5 Eigenvalue equations

Using these definitions, we can now rewrite the eigenvalue equations for Equation 5.4.3 and Equation 5.4.4, arriving at

$$I_1^2 = (I_0 - 1)(I_2 + 1), \tag{5.5.1}$$

$$I_2 - I_0 = 2, \tag{5.5.2}$$

where the first equation is obtained by solving the 2×2 determinant of Equation 5.4.3. The integral terms I_n are defined as

$$I_n = \int d\Gamma \ G_{E,v} \ \frac{v^n}{w + q - \varpi/\mu}, \tag{5.5.3}$$

where we have introduced the variables w and q, which correspond to a dimensionless frequency and a dimensionless wave number, respectively. They are defined as

$$w = \frac{\omega - \Lambda_0 - \Phi_0}{\mu}, \tag{5.5.4}$$

$$q = \frac{K - \Phi - \Lambda}{\mu}. \tag{5.5.5}$$

We also introduce the parameter $\bar{\lambda} = \lambda + \mu\epsilon$, which will be specially useful in for the stationary case i.e. for the case $\Omega = 0$.

5.5.1 Massless limit

As we will later discuss, the situation where the neutrinos are massless ($\varpi = \Delta m^2/2E = 0$) has very interesting features. Therefore, we will introduce some definitions for this special case. For instance, the neutrino distribution function depends only on the angle and we use the dimensionless form

$$G_v = \frac{1}{n_{\nu_e} + n_{\bar{\nu}_e}} \int_0^\infty \frac{dE\ E^2}{(2\pi)^3} \int_{-\pi}^{+\pi} d\varphi \left[f_{\nu_e}(E, v) - f_{\bar{\nu}_e}(E, v) \right]. \tag{5.5.6}$$

The eigenvalue equations are the same ones as in the previous section. Nonetheless, the integral terms are now

$$I_n = \int_{-\infty}^{+\infty} dv G_v \frac{v^n}{w + q}, \tag{5.5.7}$$

where w no longer depends on ϖ. On the other hand, the neutrino asymmetry and flux in this limit are

$$\epsilon = \int_{-1}^{+1} dv\ G_v = \frac{n_{\nu_e} - n_{\bar{\nu}_e}}{n_{\nu_e} - n_{\bar{\nu}_e}} \quad \text{and} \quad \phi = \int_{-1}^{+1} dv\ v\ G_v = \frac{\langle v_{\nu_e} \rangle n_{\nu_e} - \langle v_{\bar{\nu}_e} \rangle n_{\bar{\nu}_e}}{n_{\nu_e} - n_{\bar{\nu}_e}}. \tag{5.5.8}$$

Let's now analyze the structure of these equations. First of all, the distribution function g_v in the integral expressions 5.5.7 will be provided by the physical setup that we want to explore. Once we have the g_v function, the idea is to seek for the pairs of (w, q) points for which the Equations 5.5.1 are satisfied. If there is a pair of real values of (w, q) that solves the eigenvalue equation, we can assert that the system is stable, and that any perturbation can trigger flavor instability. However, nothing prevents that for some region of the parameter space, the solutions imposed by the eigenvalue equations require a w or a q with an imaginary part. In these cases, the system will be unstable, and small perturbations can trigger flavor conversion.

In order to discuss the physics contained in these equations in a more intuitive way, we proceed to apply them to a toy model which will help us to explore all the useful information contained in such simple equations.

5.6 The two neutrino beam model

As mentioned above, in order to extract the maximal amount of information from the DR, we will discuss a very interesting toy model, which consists of two infinitely long colliding beams. Both beams contain left and right moving neutrinos and antineutrinos. We can see in Figure 5.1 a pictorial representation of the system. The main advantage of this toy model is that is analytically solvable [2], which has motivated a wide variety of studies [52–55].

The road map to understand the physical implications of the DR is the following: we will start with the most easy example, consisting of two frontally

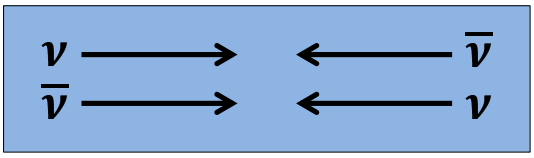

Figure 5.1: Pictorical representation of colliding beams of neutrinos and antineutrinos [2]. The system is initially homogeneous, and is infinite in all directions. The normalized neutrino flux is $1 + a$, and the antineutrino one is given by $1 - a$, with $-1 \leq a \leq 1$. The upper beam has a normalized strength of $1 + b$, whereas the lower beam has $1 - b$, where the parameter b parametrizes the left-right asymmetry.

colliding beams. We will consider inhomogeneities in the perpendicular direction, but assuming that the system is spatially stable. This translates into the fact that we can label the inhomogeneities using their wave vectors. Moreover, we will strict our study to the time evolution of the system. As a first step, we consider the maximally asymmetric case, which consist of only two modes, and then we will allow for asymmetries, which translates in adding two extra modes for a total of four.

The next step will be to consider a laterally homogeneous case, but with the two beams colliding with an angle. As a last step, we will consider the same setup, but for the first time we will also consider the spatial evolution in our equations. This will lead us, for the first time, to a full DR relation, and allow us to plot the instabilities regions in the ω–k_z plane.

5.6.1 Two colliding beams

As stated above, we will start with the simplest example consisting of a one-dimensional system of two colliding beams. This is pictorially represented in Figure 5.1. For this first configuration we will strictly study the temporal evolution of the system. By doing so, we implicitly assume that the system is spatially stable, and therefore the spatial modes can be described by the wave vectors k, which are, according to our assumptions, *real* numbers. On the other hand, in order to make this example more intuitive, we will be use three-vector notation. The EOM for this is

$$\Omega\, Q_i = \left[\varpi_i + \mathbf{v}_i \cdot \mathbf{k} + \mu \sum_{j=1}^{N} (1 - \mathbf{v}_i \cdot \mathbf{v}_j)\, g_j \right] Q_i - \mu \sum_{j=1}^{N} (1 - \mathbf{v}_i \cdot \mathbf{v}_j)\, g_j Q_j \,. \tag{5.6.1}$$

Because we are dealing with a discrete system, we have replaced our integrals with summations. This is the nicest features of the neutrino beam example; the discreteness of the velocity distributions translates to analytically solvable equations and thus makes this system very useful to understand the underlying physics. Another highly useful feature of this system is that,

due to the discrete nature of the system, we can write the EOM in a matrix form, so that

$$\Omega \begin{pmatrix} R \\ \bar{L} \\ L \\ \bar{R} \end{pmatrix} = \left[\begin{pmatrix} \varpi + k & 0 & 0 & 0 \\ 0 & -\varpi - k & 0 & 0 \\ 0 & 0 & \varpi - k & 0 \\ 0 & 0 & 0 & -\varpi + k \end{pmatrix} + \lambda \; + 2\mu \begin{pmatrix} l + \bar{l} & -\bar{l} & -l & 0 \\ -r & r + \bar{r} & 0 & -\bar{r} \\ -r & 0 & r + \bar{r} & -\bar{r} \\ 0 & -\bar{l} & -l & l + \bar{l} \end{pmatrix} \right] \begin{pmatrix} R \\ \bar{L} \\ L \\ \bar{R} \end{pmatrix}, \tag{5.6.2}$$

where the factor factor of two arises from the current-current term $(1 - \mathbf{v}_i \; \mathbf{v}_j)$, which is 2 for opposite velocities, and zero for parallel ones.

Two modes

We will start discussing the case where we only have right-moving neutrinos and left-moving antineutrinos, i.e., $\bar{r} = l = 0$. This setup corresponds to the maximal left-right asymmetry. We also introduce the parameter a, defined in the range $-1 \leqslant a \leqslant 1$, which will determine the neutrino-antineutrino asymmetry of the example, such that $r = (1 + a)$ and $\bar{l} = -(1 - a)$. In the language of the previously introduced matrix, will mean that the EOM reduce to a 2×2 matrix of the form

$$\Omega \begin{pmatrix} R \\ \bar{L} \end{pmatrix} = \left[\begin{pmatrix} \varpi + k & 0 \\ 0 & -\varpi - k \end{pmatrix} + \begin{pmatrix} -1 + a & 1 - a \\ -1 - a & 1 + a \end{pmatrix} \right] \begin{pmatrix} R \\ \bar{L} \end{pmatrix}. \tag{5.6.3}$$

Let's now examine this equation carefully. The wave number k, which is by definition a real quantity, appears in the diagonal entries of the matrix, always with the same sign as the vacuum oscillation frequency ϖ. The reason for it can be inferred from Equation 5.6.2. The wave number appears in the equations under the term $\mathbf{v} \cdot \mathbf{k}$. This term is positive, i.e. $+k$, for right moving neutrinos (vacuum frequency $+\varpi$), and negative $(-k)$ for left-moving antineutrinos (vacuum frequency $-\varpi$). Therefore, for the left moving antineutrinos, this product will have a negative sign, and, according to our introduced convention, antineutrinos have negative ϖ. So, in essence, k is playing the same role ϖ is. This motivates us to introduce the parameter $\widetilde{\varpi}$ defined as

$$\widetilde{\varpi} = \varpi + k. \tag{5.6.4}$$

Using this parameter, when solving Equation 5.6.3, we arrive at the following eigenvalue equation

$$\Omega = 2a\mu \pm \sqrt{(2a\mu)^2 + \widetilde{\varpi}(\widetilde{\varpi} - 4\mu)}. \tag{5.6.5}$$

If we set $\widetilde{\varpi}$ to zero, the solutions obtained are purely real. For a non-zero $\widetilde{\varpi}$, the eigenfrequencies have a imaginary part for

$$1 - \sqrt{1 - a^2} < \frac{\widetilde{\varpi}}{2\mu} < 1 + \sqrt{1 - a^2}, \tag{5.6.6}$$

where the k modes can be positive and negative. However, we have defined μ to be positive, which means that $\widetilde{\varpi} > 0$ or, equivalently, $k > -\varpi$. The imaginary part is maximal for $\mu = \widetilde{\varpi}/(2a^2)$, and is

$$\mathrm{Im}(\Omega_{\max}) = \widetilde{\varpi}\sqrt{\frac{1}{a^2} - 1}. \tag{5.6.7}$$

This equation shows very interesting features. First of all, if we return to the homogeneous case ($k = 0$), the growth rate is proportional to ϖ, which is the usual behavior in the context of linearized stability analysis. On the other hand, if we remain the inhomogeneous case ($k \neq 0$), but we set the vacuum oscillation frequency to zero ($\varpi = 0$), the imaginary part is not zero, as one would expect. On the contrary, the instability growth rate has a maximum value, which occurs for $\tilde{\omega} = 2\mu$, given by

$$\mathrm{Im}(\Omega_{\max}) = 2\mu\sqrt{1 - a^2}. \tag{5.6.8}$$

In other words, the maximum growth rate is proportional to μ, i.e., to $\sqrt{2}G_{\mathrm{F}}n_\nu$. This unprecedented behavior receives the name *fast flavor conversion*, since the neutrino-neutrino interaction strength can be much higher than ϖ. Finally, we must remark that this phenomenon vanishes in case we go to the symmetrical configuration, i.e., with the parameter a being $+1$ or -1.

Four modes

As a next step, we will extend the previous example by adding two degrees of freedom. In other words, we won't be considering the most asymmetric scenario but we study the case where there are both neutrinos and antineutrinos moving right and left. Analogously to the previous section, we will use the parameter a to measure the neutrino-antineutrinos asymmetry. Moreover, we introduce the parameter b, defined on the range $-1 \leq b \leq 1$ to denote the left-right symmetry. Using these parameters, the occupations can be written as

$$r = +\tfrac{1}{2}(1 + a)(1 + b), \tag{5.6.9a}$$
$$\bar{l} = -\tfrac{1}{2}(1 - a)(1 + b), \tag{5.6.9b}$$
$$l = +\tfrac{1}{2}(1 + a)(1 - b), \tag{5.6.9c}$$
$$\bar{r} = -\tfrac{1}{2}(1 - a)(1 - b). \tag{5.6.9d}$$

We can now rewrite the neutrino-neutrino refraction matrix from Equation 5.6.2 as

$$\mu \begin{pmatrix} 2(a-b) & (1-a)(1+b) & -(1+a)(1-b) & 0 \\ -(1+a)(1+b) & 2(a+b) & 0 & (1-a)(1-b) \\ -(1+a)(1+b) & 0 & 2(a+b) & (1-a)(1-b) \\ 0 & (1-a)(1+b) & -(1+a)(1-b) & 2(a-b) \end{pmatrix}. \tag{5.6.10}$$

From this equation, we can see that the case analyzed in the previous section corresponds to $b = 1$. However, for this more general case, we deal with 4×4 matrices. Therefore, the eigenvalue equation will be of quartic order, meaning that we can gain very few insights from the general solution. However, there are particular cases which can be very helpful to provide some understanding of the underlying physics. We start with the homogeneous case ($k = 0$). Moreover, we consider the left-right symmetric configuration, which means $b = 0$. In this limit, we obtain two eigenvalue equations given by

$$\Omega = a\mu \pm \sqrt{(a\mu)^2 + \varpi(\varpi - 2\mu)}, \tag{5.6.11a}$$

$$\Omega = 3a\mu \pm \sqrt{(a\mu)^2 + \varpi(\varpi + 2\mu)}. \tag{5.6.11b}$$

This symmetrical setup has been traditionally the object of study in the literature. The first solution corresponds to the usual flavor pendulum for IO, whereas the second corresponds to the symmetry breaking solution for NO. Both solutions have been studied in Reference [52]. Solutions with $k \neq 0$ have been discussed in References [1, 54], and will be the object of study in the next chapter. We now focus on the asymmetric ($b \neq 0$) scenario. Very interestingly, we find non-trivial solutions for the eigenvalue equations even in the massless limit, i.e., $\varpi = 0$, which are

$$\Omega = 2a\mu \pm (k - 2b\mu), \tag{5.6.12a}$$

$$\Omega = 2a\mu \pm \sqrt{(2a\mu)^2 + k(k - 4b\mu)}. \tag{5.6.12b}$$

These equations provide only real solutions in the case both b and k are zero. However, in the general case, the second equation can provide imaginary solutions under the condition $(2a)^2 < k(4b\mu - k)$. This condition can also be expressed as

$$b - \sqrt{b^2 - a^2} < \frac{k}{2\mu} < b + \sqrt{b^2 - a^2}. \tag{5.6.13}$$

Therefore, there are only unstable solutions if $a^2 < b^2$. In other words, the necessary condition for instability in the $\varpi = 0$ case is that the left-right asymmetry must exceed the neutrino-antineutrino asymmetry. For a given value of μ, the maximum growth rate is reached for $k = 2b\mu$, and is

$$\mathrm{Im}(\Omega_{\max}) = 2\mu\sqrt{b^2 - a^2}. \tag{5.6.14}$$

As happened in the previous case, the maximum growth rate is proportional to the neutrino-neutrino interaction strength μ, and it appears only for $k \neq 0$.

5.7 Intersecting beams

Hitherto, we have seen that an asymmetry is the triggering factor for fast flavor conversion, i.e., flavor conversion for $\varpi = 0$. However, for the one dimensional

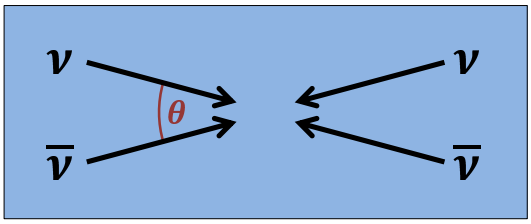

Figure 5.2: Two intersecting beams with of four modes [2]. The system is assumed to be homogeneous and the beams have a relative angle θ.

case, inhomogeneities are necessary in order to observe this phenomenon. The natural question to ask is whether it is possible to observe fast flavor conversion in a scenario where $k = 0$. In order to answer this question, we will proceed to analyze a two dimensional model. The idea is to extend the simple model we have already studied by considering that the two beams intersect with an angle θ. This model is pictorially displayed in Figure 5.2. This setup corresponds to the four modes case, with directions that intersect with an angle θ. In this situation we can have a velocity component in the perpendicular direction[1]. As stated above, this example is constructed assuming a homogeneous transverse direction or $k = 0$. By a careful examination of the symmetries of the system, we realize that we can obtain a more elegant analytical solution if we decompose the system in a symmetric and an asymmetric mode, which are defined as

$$A_\pm = \tfrac{1}{2}(L \pm R), \tag{5.7.1a}$$
$$\bar{A}_\pm = \tfrac{1}{2}(\bar{L} \pm \bar{R}), \tag{5.7.1b}$$

respectively. Thanks to these two newly introduced modes, we can massage Equation 5.6.2 and obtain two decoupled equations. The first one, corresponding to the symmetric mode, is

$$\Omega \begin{pmatrix} R \\ \bar{L} \end{pmatrix} = \left[\begin{pmatrix} \varpi + k & 0 \\ 0 & -\varpi - k \end{pmatrix} + \begin{pmatrix} -1+a & 1-a \\ -1-a & 1+a \end{pmatrix} \right] \begin{pmatrix} R \\ \bar{L} \end{pmatrix}, \tag{5.7.2}$$

and analogously for the asymmetric mode

$$\Omega \begin{pmatrix} R \\ \bar{L} \end{pmatrix} = \left[\begin{pmatrix} \varpi + k & 0 \\ 0 & -\varpi - k \end{pmatrix} + \begin{pmatrix} -1+a & 1-a \\ -1-a & 1+a \end{pmatrix} \right] \begin{pmatrix} R \\ \bar{L} \end{pmatrix}. \tag{5.7.3}$$

The asymmetric eigenvalue Equation 5.7.2 only provides real eingevalues when setting ϖ to zero. On the other hand, the asymmetric eigenvalue equation given by Equation 5.7.3 provides non-trivial imaginary solutions even in the $\varpi = 0$, such that

$$\Omega = \frac{a\mu(5 + \mathrm{c}_\theta)}{2} \pm \frac{\mu}{2}\sqrt{(1+\mathrm{c}_\theta)^2 a^2 - 8\mathrm{c}_\theta(1-\mathrm{c}_\theta)}, \tag{5.7.4}$$

[1]This system, as we will discuss in Chapter 7, can be related to a more SN-type scenario where neutrinos are emitted from a spherical surface.

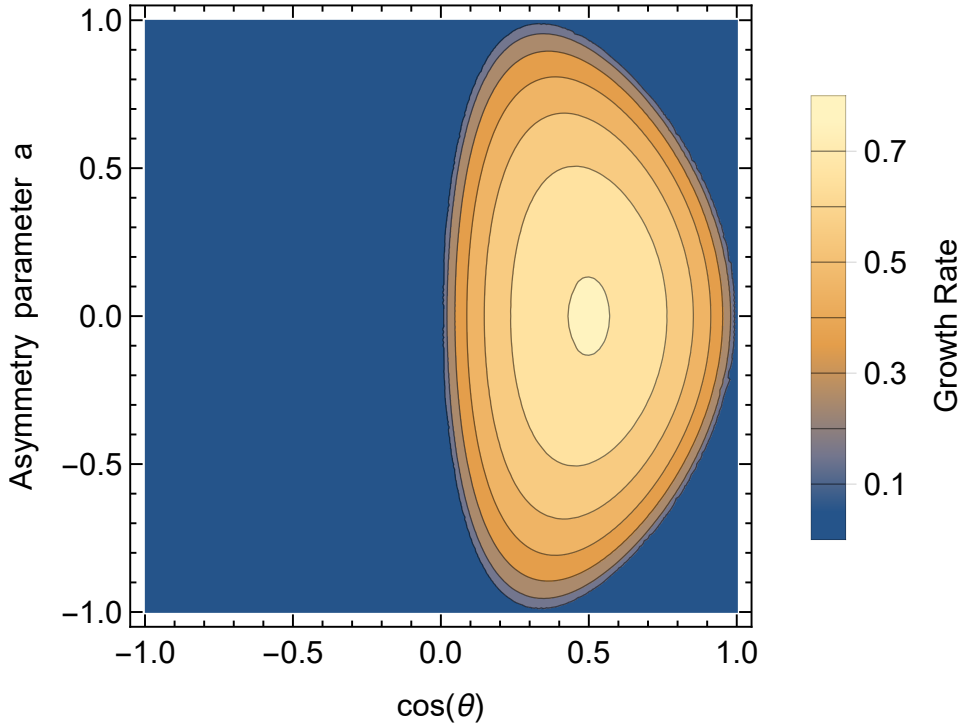

Figure 5.3: Contour plot of the growth rate given by Equation 5.7.4 as a function of the left-right asymmetry parameter a ($-1 < a < 1$) and $\cos(\theta)$ [2]. For this figure the mode occupations have been chosen to be left-right symmetric. The growth rate is shown in units of μ. Instabilities occur only for $\cos(\theta) > 0$, but are symmetric with respect the sign of a.

where $c_\theta = \cos(\theta)$. In Figure 5.3 we show a contour plot for the imaginary part of Ω as function of the asymmetry parameter a and the cosine of the intersecting angle $\cos(\theta)$. From the figure we can infer that the system is symmetric with respect to the parameter a, whereas there are only unstable solutions for positives vales of $\cos(\theta)$. The maximum growth rate is

$$\mathrm{Im}(\Omega_{\mathrm{max}}) = \mu/\sqrt{2}, \tag{5.7.5}$$

reached for $a = 0$ and $\cos(\theta) = 1/2$. Once again, this quantity is proportional to μ.

Figure 5.3 shows us under which circumstances the system will be unstable, but it does not provide information of how the system exactly behaves in the unstable regime. In order to gain a physical understanding of the system's behavior, we have numerically solved the system using the full non-linear equations. The result of this study is that the system shows the typical behavior of a flavor pendulum [52]: for a small perturbation, there is an exponential growth of the traversal component, followed by a flavor conversion given by $\nu_e\overline{\nu}_e \to \nu_x\overline{\nu}_x$ and then the opposite one $\nu_x\overline{\nu}_x \to \nu_e\overline{\nu}_e$.

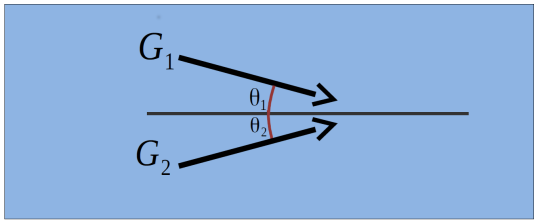

Figure 5.4: Two neutrino beam emission spectra from a SN disk.

5.8 Temporal and spatial evolution

Up to this point, we have constrained ourselves to the temporal evolution of the flavor field. At this level, we have already highlighted the crucial role that the angular distribution plays. However, we have neither considered spatial evolution nor have we considered the system's stability from the spatial standpoint. As we have already mentioned, the analyses described up to this point relies on the assumption that the system is spatially stable. This assumption is not physically justified, so our task is now to explore how the system behaves when we abandon it.

To this end, we have constructed the following example, where we have used the same geometry of the previous section. The novelty relies on the fact that we will study the evolution of the system in time *and* space. For the first time in this thesis, we will study the solutions of a full DR equation. The toy model used is a particular case of the intersecting beams scenario discussed in the last section. We will continue to assume the $\varpi = 0$ limit. This model is motivated by the SN-type scenarios that we will discuss in the next chapters. The model is pictorially displayed in Figure 5.4. The idea is that two neutrino beams are emitted from a disc, and interact at some distance from the disc. The velocities are defined with respect to angle with respect to the radial direction of the disk, c_1 and c_2. This translates to an angular distribution given by

$$G_{\mathbf{v}} = G_1\delta(\mathrm{c}_\theta - c_1) + G_2\delta(\mathrm{c}_\theta - c_2). \tag{5.8.1}$$

Fortunately for us, we have worked out the EOM for this specific situation, which led us to the eigenvalue equations given by Equation 5.5.1. For convenience, we will write them again here

$$I_1^2 = (I_0 - 1)(I_2 + 1), \tag{5.8.2}$$

$$I_2 - I_0 = 2. \tag{5.8.3}$$

Although the toy problem is rather simple, the DR obtained is complicated from the algebraic point of view. Indeed, there is little information we can extract from the analytical solution. Nevertheless, we can solve the DR for different examples and try to understand the physics of the system. The next section is devoted to this task.

Forbidden bands

To gain some understanding of the information contained in the DR, we have plotted the results provided by Equation 5.8.2 in Figure 5.5. More precisely, we have displayed the axially symmetric solutions. We have chosen this solution for simplicity since the axially breaking solution produces very similar results. Figure 5.5 shows the DRs hyperbolas in the ω–k_z plane. This figure will allow us to identify regions in the parameter space where there are no allowed frequencies, regions where there are not allowed wave number solutions, or both. Let's analyze carefully the four possible cases[2].

The panels on the left column correspond to $0 \leq \cos\theta_{1,2} \leq 1$ or, in other words, to forward-only emission. This is the assumption classically made for the bulb model, as we will explain in the next chapter. The panels on the right column correspond to forward and backward emission, which follows from the condition $\cos\theta_2 < 0$. Moreover, the panels in the upper row correspond to the case where both beams have an ν_e excess ($G_{1,2} > 0$), whereas the lower column shows the case where one mode has an $\bar{\nu}_e$ excess ($G_2 < 0$).

We will start analyzing left upper panel, i.e., the case where both beams are ν_e dominated ($G_{1,2} > 0$) and there is forward-emission only ($\cos\theta_{1,2} < 0$). In such case, we see that for the whole parameter space, there is always a real pair of $(\omega - k_z)$ values that fulfills the DR equation. In other words, no fast flavor conversion will ever occur. We shift now to the top-right panel, where both beams are ν_e dominated ($G_{1,2} > 0$) but we have backwards modes ($\cos\theta_2 < 0$). For this particular setup, the DR prescribes two parabolas of real ω and k_z, but there is frequency gap. This means that all spatial disturbances will propagate. However, if we impose as initial condition a value for the frequency from the forbidden gap, the system will undergo a spatially exponential growth. The red blob represents the modulus of the imaginary part of k_z for such a situation. The lower-right panel shows the situation where the forward mode ($\cos\theta_1 > 0$) has an $\bar{\nu}_e$ excess ($G_1 < 0$), whereas the backward mode ($\cos\theta_1 > 0$) an ν_e excess ($G_2 > 0$). In this case, there is a wave number gap. In other words, all temporal disturbances will propagate, but if we impose as initial condition a value for k_z from the gap, the system will undergo a temporal run away. The red blob shows the modulus of $\mathrm{Im}(\omega)$. Finally, for the lower-left panel, we have the situations where there are only forward modes ($\cos\theta_{1,2} < 0$), but one of the beams shows an $\bar{\nu}_e$ excess ($G_1 < 0$). In this situations, we can have a complex ω for a real k_z or a complex k_z for a real ω. Therefore, disturbances with k_z in the wave number gap will grow exponentially in time, whereas a real value for ω imposed at the boundary causes exponential spatial growth. These conclusions carry over to even more general $G(\theta)$, where the necessary condition for the gaps is wave number gap is that the ELN has to show a crossing from positive to negative intensities. This crossing generates a gap which, in turn, leads to

[2]A very similar four panel figure can be found in Reference [56], in the context of plasma physics.

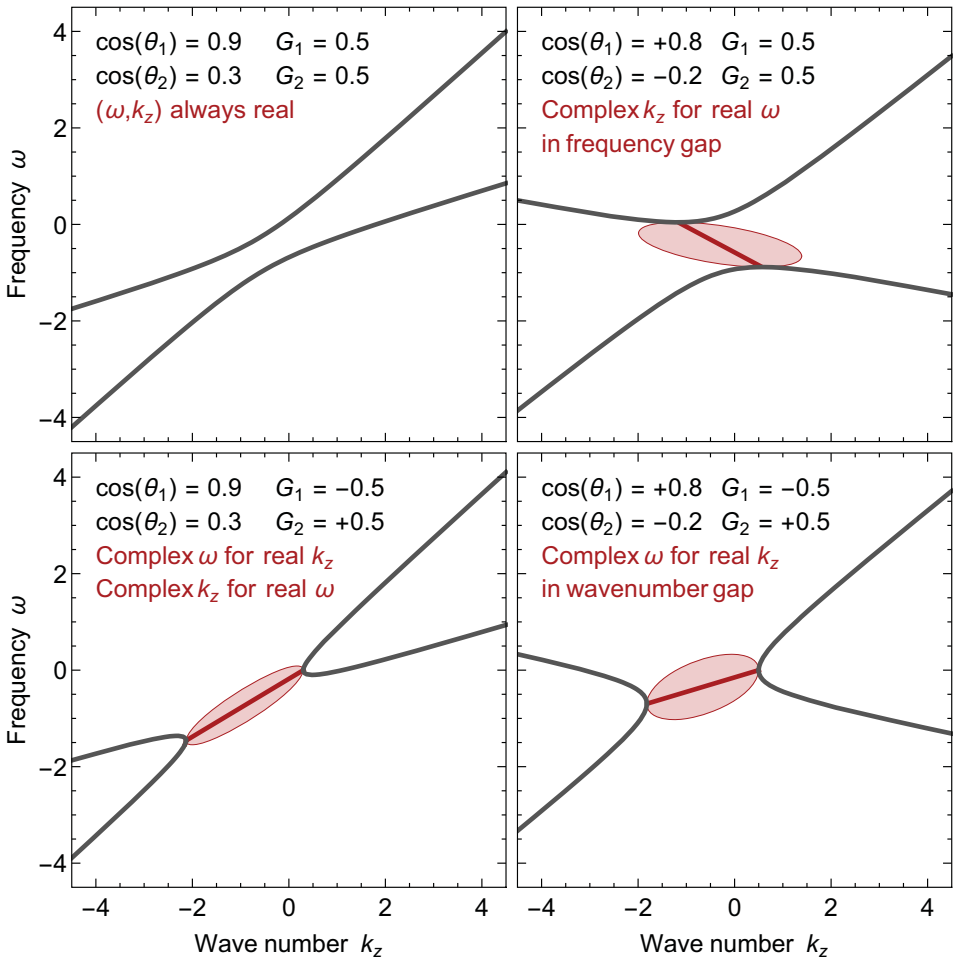

Figure 5.5: DRs for two colliding beams, non-stationary case [4]. The black lines are the hyperbolas obtained from Equation 5.8.2. The thick red lines are the real part of the frequency ω for real wave vector k_z or the real part of k_z for an imaginary ω. The red bubbles are the imaginary part of ω or k_z. The panels in the left column shows the configurations with only forward modes, and the panels in the right column shows the scenario with forward and backward modes. Moreover, the top row panels correspond to a ν_e excess scenario whereas the two bottom panels to a $\bar{\nu}_e$ excess in the forward mode scenario.

fast flavor conversion. We can trace an analogy between this effect and the spectral crossings in the traditional unstable modes [57, 58].

Let's now summarize the information contained in Figure 5.5. If the DR has no gaps, we can conclude that the system is stable. However, this not seem to be the generic case. Depending on the characteristics of the angular emission of the system, there can be regions where there are no allowed real frequencies, regions where there are not allowed real wave numbers, or both. Altogether, the DR will determine which solutions are compatible with the EOM, but not if these solution will indeed occur.

5.9 Boundary conditions

As we have discussed, having backward modes produces very interesting effects in our DR. The idea of having such modes in a SN-type scenario is not new: some authors have already proposed models with a backward flux [59,60]. The existence of such a flux immediately implies the necessity of having different boundary conditions in different spatial regions of the SN. Moreover, in a SN, the inward moving neutrinos come form NC scattering from the outward moving ones. This implies a flavor correlation between the inward and outward flow of neutrinos which goes beyond the prescription of the EOM.

Furthermore, we have studied that under certain circumstances, the DR shows ω gaps. In such a case, the spatial boundary conditions and their time variation are needed to understand the generic behavior of the flavor field. It is also possible that the collision term has to be included in the EOM to see which modes of the flavor field are actually excited, which would go beyond the forward-scattering description used in our analysis.

On the other hand, we have discussed that "crossings" in the ELN will result in a DR with a gap for the wave vector, and temporal instabilities, which depend in the initial conditions of the flavor disturbances. Furthermore, there could be the situation where there is both a gap for the wave vector and the frequency. In such a case we have the advantage that if the system is unstable on its space or on its time evolution would be sufficient for flavor decoherence.

5.10 Summary

The introduction of a multidimensional FT to solve the EOM has led us to an equation for the flavor modes where for every wave number there is an associated frequency. In other words, we have ended up with a dispersion relation for the flavor waves. We have developed the equations for a generic case where there is some axial asymmetry that we have arbitrarily named the z direction. Moreover, we have derived the equations for the axially symmetric and axially breaking cases. We have then particularized the equations for a

laterally homogeneous case and for the massless limit, and we have introduced some definitions that are frequently used in linearized flavor stability analysis.

The colliding neutrino beam model has been used as a toy model to understand the potential of the DR. To begin our analysis, we have assumed that the system is spatially stable, and we have focused on the study of the temporal evolution. For the first example, we have studied the two neutrino beam.

During the study of these models, we have encountered for the first time the fast oscillations i.e. flavor conversion modes whose growth rate is proportional to the neutrino interaction strength μ.

Fast oscillations

For the vast majority of the cases studied previously in the literature, the growth rate for the flavor instabilities is proportional to ϖ. However, by breaking the symmetry of the system, we see that the growth rate of the instability is proportional to μ. Moreover, dense environments are defined by the condition $\mu \gg \varpi$. For this reason, this type of instabilities are referred to as fast flavor conversion. To put numbers to these assertions , we will remind the reader that, for the case of neutrinos with an energy of $E = 12.5$ MeV, the vacuum oscillation frequency is $\varpi = 0.5\ \mathrm{km}^{-1}$, whereas the growth rate of "fast multiangle instabilities" is given by

$$\Phi_0 = \sqrt{2} G_{\mathrm{F}} (n_{\nu_e} - n_{\bar{\nu}_e}) = 6.42\ \mathrm{m}^{-1}\ \frac{n_{\nu_e} - n_{\bar{\nu}_e}}{10^{31}\ \mathrm{cm}^{-1}}, \tag{5.10.1}$$

where we have used natural units with $\hbar = c = 1$. In any case, in the real scenario there are indeed flavor oscillations due to neutrino masses and their mixing angles, so even if their are not the dominant source of self-induced flavor conversion there will nevertheless act as seed to self-induced neutrino oscillations even on the mean-field regime.

For the next step, we have dropped the assumption that the system is spatially stable and we have studied the spatial and temporal evolution of the two beam scenario. In other words, we have studied for the first time the full DR of the system. We have shown the four types of forbidden regions. For any physical scenario where self-induced neutrino flavor oscillations may occur, the resulting DR needs to be a linear combination of this four cases.

Finally, we have pointed out that the main limitation of the DR is that it does not determine which of the solutions will develop in a real scenario. In order to understand how the system behaves, it is unavoidable to deal with the boundary conditions.

Chapter 6

Particular case: non-homogeneity in the bulb model

In the present chapter, we discuss a particular case of the general equations discussed in Chapter 5. More precisely, we will apply the EOM to a toy model that mimics the environment present inside a core-collapse SN. The first step will consist of introducing the bulb geometry and adapt the EOM to this particular setup. We will assume that the system is stationary and we will restrict our study to the spatial evolution of the system. Furthermore, we will start by assuming the same angular emission distribution for all the neutrino species. The particularity of this study relies on the fact that we will consider inhomogeneities in the perpendicular direction, and we will study the effects these small scale perturbations can have in the flavor evolution of the neutrino flavor field in a SN-type scenario.

The main difficulty arises from the fact that the equations for this scenario are not analytically solvable. Therefore, we will start studying simplified models and we will gradually add complexity to the system until we reach a realistic setup. Using this approach will help us understand the role of the inhomogeneous modes in the perpendicular direction.

The first case analyzed is a one dimensional (1D) model, which will provide us a first glimpse of the effect of the small scale instabilities in the system. We then go a step forward in complexity and we study a two dimensional (2D) model. In the conclusions, we discuss our results and we study the impact of perpendicular homogeneities in a realistic SN scenario by plotting a footprint diagram, where we use the matter profile provided by a numerical core-collapse SN simulation. Finally, we discuss the validity of these results and the impact of the assumptions made.

6.1 Stationarity, same ν_e and $\bar{\nu}_e$ angular distribution

For a long period of time, the studies in neutrino self-induced flavor conversion have been performed under the assumption of stationarity. The justification for this assumption was the following: because ultrarelativistic neutrinos move at speeds very close to the speed of light, the traveling time of a neutrino emitted from the neutrino sphere to the outer space is of the order of 10^{-4} s. In this time scale, it is reasonable to expect that the SN environment has not changed, and therefore the stationarity is justified. However, this is not necessarily the case if the neutrino ensemble is unstable in its time evolution, i.e., if the system is in one of the forbidden bands described in Chapter 5.

Given that we are not in one of these regions, we can safely drop the time dependence of the equations and investigate the stability of the system on its spatial evolution. Furthermore, we will assume the same angular emission for all neutrino species. Although, as discussed in Chapter 3, this is not physically sustained, it has been assumed for a long time in the context of self-induced flavor conversion[1]. The present chapter is based on the results of Reference [1].

6.2 The bulb model

The first step for this discussion is to introduce the *bulb model* [61–63], which is a geometry that has been widely used in the context of core-collapse SN neutrino emission. As we will discuss, this geometry is physically well motivated. The basic geometry of the bulb model can be seen in Figure 6.1.

The main characteristic of the "Neutrino bulb model" is that neutrinos are isotropically emitted from a spherical surface of a given radius R. The zenith angle (θ_r) is described with the usual label $u = \sin^2\theta_r$, thus the isotropic "blackbody like" emission implies a uniform distribution over the interval, $0 \leq u \leq 1$. Similar to Reference [64], we stress that R is not the physical neutrino decoupling radius or neutrino sphere, but rather the radius of a hypothetical blackbody surface. The zenith angle distribution at the neutrino sphere is found to be forward peaked. In order to avoid the complication from the angular distribution of the spectrum, we define R such that the u distribution is uniform.

The direction perpendicular to the radial direction is labeled as $\mathbf{x}$, and the radial (v_z) and perpendicular ($\boldsymbol{\beta}$) velocities are related by $\mathrm{v}_z = \sqrt{1-\boldsymbol{\beta}^2}$. Therefore, $\mathbf{v}\cdot\boldsymbol{\nabla} \to \mathrm{v}_z\partial_z + \boldsymbol{\beta}\cdot\boldsymbol{\nabla}_{\mathbf{x}}$ and neglecting terms higher than $\mathcal{O}(\boldsymbol{\beta}^2)$ gives $(\mathbf{v}-\mathbf{v}')^2 \approx (\boldsymbol{\beta}-\boldsymbol{\beta}')^2$.

We re-scale our variables by going to a "co-moving" coordinate frame such that the angular scale remains fixed, i.e., $\boldsymbol{\beta} = \frac{R}{r}\boldsymbol{\beta}_a$ and $\mathbf{a} = \frac{R}{r}\mathbf{x}$. $\mathbf{v}$ is defined

[1] In the next chapter we will investigate the case where the different neutrino species have different angular distributions.

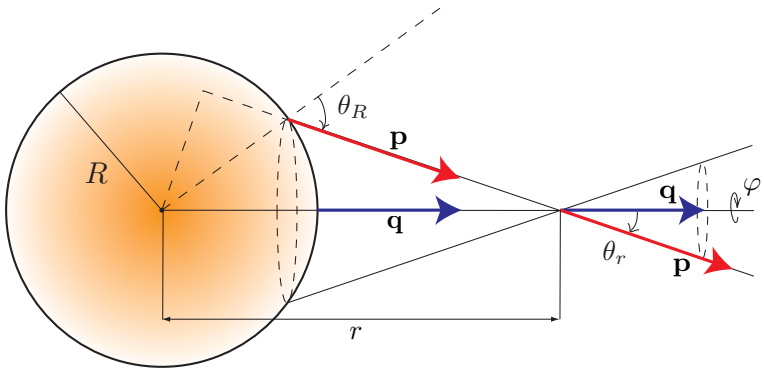

Figure 6.1: Geometric layout of the neutrino bulb model emission [28]. Neutrinos are emitted half-isotropically from the surface of the neutrino sphere. The θ_r is defined between the neutrino's trajectory and the radial directions at the radius r.

as a 2D vector with $0 \leq |\mathbf{v}| \leq 1$. This variable $\mathbf{v}$ is related to the usual u as $\mathbf{v}^2 = u$. In the new variables, therefore $\boldsymbol{\beta} \cdot \boldsymbol{\nabla}_{\mathbf{x}}$ becomes $\boldsymbol{\beta}_a \cdot \boldsymbol{\nabla}_{\mathbf{a}}$. Moreover, some of the factors R/r can be reabsorbed in the definitions of μ and λ such that

$$\lambda = \sqrt{2} G_{\mathrm{F}} (n_e + n_{\bar{e}}) \frac{R^2}{r^2} \quad \text{and} \quad \mu = \sqrt{2} G_{\mathrm{F}} (n_{\nu_e} + n_{\bar{\nu}_e}) \frac{R^2}{r^2}. \tag{6.2.1}$$

Another advantage of using this geometry becomes noticeable as soon as we move to reference frames at large distances with respect to the neutrino sphere, i.e., in situations where $R \ll r$. In this limit, we can use the so-called *long distance approximation*, which consists of

$$v_z = (1 - (R/r)^2 \beta_a^2)^{-1/2} \approx 1 + \frac{1}{2} (R/r) \beta_a. \tag{6.2.2}$$

6.3 EOM adapted to the stationary bulb model

The linearized EOM for the setup described above is [1]

$$\begin{aligned} i(\partial_z v_z + \boldsymbol{\beta} \cdot \boldsymbol{\nabla}_{\mathbf{a}}) \, S_{t,\mathbf{x},\varpi,\mathbf{v}} = \big(\varpi + \bar{\lambda} - \mu \, \boldsymbol{\epsilon}_1 \cdot \mathbf{v}\big) \, S_{t,\mathbf{x},\varpi,\mathbf{v}} \\ - \mu \int d\Gamma' \, \tfrac{1}{2} (\mathbf{v} - \mathbf{v}')^2 \, g_{\varpi',\mathbf{v}'} S_{t,\mathbf{x},\varpi',\mathbf{v}'} \,, \end{aligned} \tag{6.3.1}$$

where the effective matter term is defined as $\bar{\lambda} = \lambda - \mu\epsilon$, with

$$\epsilon = \int d\Gamma \, g_{\varpi,\mathbf{v}} \quad \text{and} \quad \boldsymbol{\epsilon}_1 = \int d\Gamma \, g_{\varpi,\mathbf{v}} \, \mathbf{v} \,. \tag{6.3.2}$$

Here, ϵ represents the "asymmetry" between neutrinos and antineutrinos. The second term, $\boldsymbol{\epsilon}_1$, represents a neutrino current which exists if their distribution is not isotropic and not symmetric between neutrinos and antineutrinos. Moreover, $\int d\Gamma' = \int_0^{+\infty} d\varpi' \int d\mathbf{v}$ and the velocity integration $d\mathbf{v}'$ is over the unit sphere. Because the neutrino speed obeys $|\mathbf{v}| = 1$, we have written, for later convenience, the current-current velocity factor in the unusual form $(1 - \mathbf{v} \cdot \mathbf{v}') = \frac{1}{2}(\mathbf{v} - \mathbf{v}')^2$.

We now multiply both sides of Equation 6.3.1 by $1/v_z$ and apply the long distance approximation explained in last section, expanding the equation up to order $\mathcal{O}(\beta^2)$. We then re-label our variables[2] and denote the radial direction z as t, and we arrive at the following linearized EOM

$$i(\partial_t + \mathbf{v} \cdot \boldsymbol{\nabla}_{\mathbf{x}})\, S_{t,\mathbf{x},\varpi,\mathbf{v}} = \left(\varpi + \tfrac{1}{2}\bar{\lambda}\mathbf{v}^2 - \mu\, \boldsymbol{\epsilon}_1 \cdot \mathbf{v}\right) S_{t,\mathbf{x},\varpi,\mathbf{v}} - \mu \int d\Gamma'\, \tfrac{1}{2}(\mathbf{v} - \mathbf{v}')^2\, g_{\varpi',\mathbf{v}'} S_{t,\mathbf{x},\varpi',\mathbf{v}'}\,. \tag{6.3.3}$$

This equation corresponds to Equation 6 of Reference [65], but with the additional term describing the self-induced inhomogeneities. Moreover, we have also found the additional term $\mu\boldsymbol{\epsilon}_1 \cdot \mathbf{v}$ which is unavoidable in a non-isotropic system, irrespective of the question of homogeneity. This neutrino flux term is missing in Reference [65]. The presence of this term modifies the eigenvalue equation for a non-isotropic system. Moreover, since we are not in the limit $\varpi \to 0$, our equations are sensitive to the neutrino mass ordering. During our stability analysis we will be solving the equations for $-\infty < \lambda < +\infty$ and $-\infty < \mu < +\infty$. Physically, positive λ and μ correspond to NO and negative λ and μ to IO.

6.3.1 Oscillation eigenmodes

As we have stated, we restrict this study to the spatial (that we have renamed the temporal coordinate for convenience) evolution of the system. Therefore, in order to find unstable modes, we seek solutions of our linearized EOM of the form $S_{t,\mathbf{k},\varpi,\mathbf{v}} = Q_{\Omega,\mathbf{k},\varpi,\mathbf{v}} e^{-i\Omega t}$, leading to an EOM in frequency space of the form

$$\left(\tfrac{1}{2}\bar{\lambda}\,\mathbf{v}^2 + \bar{\mathbf{k}} \cdot \mathbf{v} + \varpi - \Omega\right) Q_{\Omega,\mathbf{k},\varpi,\mathbf{v}} = \mu \int d\varpi' \int d\mathbf{v}'\, \tfrac{1}{2}(\mathbf{v} - \mathbf{v}')^2\, g_{\varpi',\mathbf{v}'}\, Q_{\Omega,\mathbf{k},\varpi',\mathbf{v}'}\,. \tag{6.3.4}$$

Eigenvalues $\Omega = \gamma + i\kappa$ with a positive imaginary part represent unstable modes with the growth rate κ.

[2]The reason for this change is to use the same notation adopted in other works on this topic.

6.3.2 Monochromatic and isotropic neutrino distribution

For the examples studied, we will consider monochromatic neutrinos with fixed energy. Assuming that the energy and velocity distribution factorize, we may write the spectrum in the form

$$g_{\varpi,\mathbf{v}} = h_{\varpi}\, f_{\mathbf{v}}\,. \tag{6.3.5}$$

The monochromatic energy spectrum is

$$h_{\varpi} = -\alpha\,\delta(\varpi+\varpi_0) + \delta(\varpi-\varpi_0)\,, \tag{6.3.6}$$

meaning that we have α antineutrinos (frequency $\varpi = -\varpi_0$) for every neutrino ($\varpi = \varpi_0$). The spectral asymmetry is $\epsilon = 1-\alpha$.

We will consider isotropic velocity distributions which, in addition, are uniform, corresponding to blackbody-like angular emission in the SN context. In this case, $f_{\mathbf{v}} = 1/\Gamma_{\mathbf{v}}$, where $\Gamma_{\mathbf{v}}$ is the volume of the velocity phase space. The eigenvalue equation (6.3.4) finally simplifies to the form in which we will use it,

$$\left(\tfrac{1}{2}\bar{\lambda}\,\mathbf{v}^2 + \mathbf{k}\cdot\mathbf{v} + \varpi - \Omega\right) Q_{\Omega,\mathbf{k},\varpi,\mathbf{v}} = \mu \int d\varpi'\, h_{\varpi'}\, \frac{1}{2\Gamma_{\mathbf{v}}} \int d\mathbf{v}'\,(\mathbf{v}-\mathbf{v}')^2\, Q_{\Omega,\mathbf{k},\varpi',\mathbf{v}'}\,. \tag{6.3.7}$$

We now consider systematically different cases of velocity distributions.

6.4 One Dimensional scenario

This scenario corresponds to the same colliding beams toy model discussed in Section 5.6. We will use this example once again because of its simplicity. This model will allow us to obtain a first glimpse of the effects that small scale instabilities introduce in the system.

6.4.1 Single angle ($|v| = \pm 1$)

The first system we analyze is the single angle case, a nomenclature which refers to the zenith-angle distribution of neutrinos. Single angle means that the neutrino velocity distribution adopts the value $|v| = 1$. In our first 1D case this means we consider two colliding beams with v = 1. Matter effects can be rotated away. The eigenfunction $Q_{\Omega,k,\varpi,v}$ now consists of four discrete components. We denote these four amplitudes with the complex numbers R for right-moving ($v = +1$) neutrinos ($\varpi = +\varpi_0$), $\bar{R}$ for right-moving antineutrinos, and analogous L and $\bar{L}$ for left movers. Our master equation (6.3.7) then reads

$$\left[\begin{pmatrix} \varpi_0+k & 0 & -\mu & \mu\alpha \\ 0 & -\varpi_0+k & -\mu & \mu\alpha \\ -\mu & \mu\alpha & \varpi_0-k & 0 \\ -\mu & \mu\alpha & 0 & -\varpi_0-k \end{pmatrix} - \Omega\right] \begin{pmatrix} R \\ \bar{R} \\ L \\ \bar{L} \end{pmatrix} = 0\,. \tag{6.4.1}$$

The eigenvalues Ω are found from equating the determinant of the matrix in square brackets with zero. This condition can be written in the form

$$\left(\frac{1}{-k+\varpi_0-\Omega}-\frac{\alpha}{-k-\varpi_0-\Omega}\right)\left(\frac{1}{k+\varpi_0-\Omega}-\frac{\alpha}{k-\varpi_0-\Omega}\right)\mu^2=1\,. \tag{6.4.2}$$

This expression depends only on μ^2 and therefore yields identical eigenvalues for positive and negative μ, i.e., for both neutrino mass hierarchies. It is also even under $k\to -k$ as it must because the system was set up isotropically. The maximum growth rate that the eigenvalues of this equation provide is

$$\kappa_{\max}=\frac{2\sqrt{\alpha}}{1-\alpha}\,\varpi_0\,, \tag{6.4.3}$$

either for the homogeneous ($k=0$) and inhomogeneous ($k\neq 0$) case. Therefore, it is proportional to the vacuum oscillation frequency and not to k. The reason for that is that we are considering the symmetric configuration, as we have discussed in the previous chapter.

6.4.2 Multi-angle ($0\leq v\leq 1$)

For the next step, we want to study what is the impact of the matter or, more precisely, what is the impact of the multi-angle matter effect. Therefore, we drop the condition $|v|=1$ and instead we will integrate over the whole velocity interval $-1\leq v\leq 1$. The equations are now continuous in the velocity variable, leading us to

$$\left(\tfrac{1}{2}\bar{\lambda}\,v^2+k\,v+\varpi-\Omega\right)Q_{\Omega,k,\varpi,v}=\mu\int_{-\infty}^{+\infty}d\varpi'\,h_{\varpi'}\,\frac{1}{4}\int_{-1}^{+1}dv'\,(v-v')^2\,Q_{\Omega,k,\varpi',v'}\,. \tag{6.4.4}$$

Now, by carefully examining the r.h.s. of this equation it becomes clear that the v dependence of the equations terms is a linear combination of $A_0+A_1v+A_2v^2$. With this in mind, the appropriate ansatz to solve Equation 6.4.4 is

$$Q_{\Omega,k,\varpi,v}=\frac{A_0+A_1v+A_2v^2}{\frac{1}{2}\bar{\lambda}\,v^2+k\,v+\varpi-\Omega}, \tag{6.4.5}$$

Now, inserting this ansatz in both sides of Equation 6.4.4 we arrive at

$$\begin{aligned}A_0+A_1v+A_2v^2=\frac{\mu}{4}\int_{-\infty}^{+\infty}d\varpi'\,h_{\varpi'}\,\times\\ \int_{-1}^{+1}dv'\,(v'^2-2vv'+v^2)\,\frac{A_0+A_1v'+A_2v'^2}{\frac{1}{2}\bar{\lambda}\,v'^2+k\,v'+\varpi'-\Omega}\,.\end{aligned} \tag{6.4.6}$$

This equation consists essentially of three linearly independent equations, where each of them corresponds to the different powers of v. These equations will

be linear as a function of the parameters A_0, A_1 and A_2. We can write this equation in a compact form using matrices, obtaining

$$\left[1 - \begin{pmatrix} I_2 & 0 & I_4 \\ 0 & -I_2 & 0 \\ I_0 & 0 & I_2 \end{pmatrix}\right] \begin{pmatrix} A_0 \\ A_1 \\ A_2 \end{pmatrix} = 0, \tag{6.4.7}$$

where the I_n integrals are

$$I_n = \frac{\mu}{4} \int_{-\infty}^{+\infty} d\varpi \, h_\varpi \int_{-1}^{+1} dv \, \frac{v^n}{\frac{1}{2}\bar{\lambda}\, v^2 + k\, v + \varpi - \Omega} \,, \tag{6.4.8}$$

The main difficulty added in the multi-angle case is that we move from a discrete to a continuous system. Moreover, the transient equations like the ones given by Equation 6.4.8 are, in most cases, only analytically solvable when assuming limiting cases for some of the parameters. Therefore, we have to rely on numerical tools to study the system's evolution.

No matter effects ($\bar{\lambda} = 0$)

More useful information can be extracted by assuming there is no matter in the system, i.e., by setting $\bar{\lambda} = 0$, and study the equations to get a deeper understanding of the effects of the k modes *alone* before we include matter effects.

Homogeneous case ($k = 0$)

As a first example, we calculate the solution for the homogeneous case. In other words, we get rid of the inhomogeneities by setting $k = 0$. The peculiarity of the k modes is that they directly affect the denominator of Equations 6.4.8, and by setting them to zero, the integrals become analytically solvable. This gives us the opportunity to study how the matter potential affects the behavior of the solutions. This is a mathematically motivated study, with little interest from the point of view of a realistic physical setup. The integrals with an odd power of v will cancel. For even powers of v, we can analytically solve the integrals and obtain

$$I_n = \frac{\mu}{2n+1} \frac{(1+\alpha)\varpi_1 - (1-\alpha)\Omega}{\varpi_1^2 - \Omega^2}, \tag{6.4.9}$$

and the eigenvalue equation corresponds to

$$\det \left[\varpi_0^2 - \Omega^2 - \frac{\mu}{2} \begin{pmatrix} \frac{1}{3} & 0 & \frac{1}{5} \\ 0 & -\frac{2}{3} & 0 \\ 1 & 0 & \frac{1}{3} \end{pmatrix} \left[(1+\alpha)\, \varpi_0 + (1-\alpha)\, \Omega \right] \right] = 0 \,. \tag{6.4.10}$$

This determinant provides two sets of decoupled equations: one given by the middle entry $-2/3$ and another one given by the remaining 2×2 block. These

solutions are plotted in Figure 6.2. The positive values for μ correspond to NO, whereas the $\mu < 0$ results correspond to IO. These results are very similar to the three types of instabilities in the study of axial symmetry breaking solutions in SN [65]. The solution that only appears in the IO region is the Bimodal instability and corresponds to the flavor pendulum. It is given by the decoupled eigenvalue equation provided by Equation 6.4.10. The first of the instabilities in the NO region is the "multi-azimuthal angle" (MAA) instability. The third solution, which appears only in NO and for large μ is the "multi zenith angle" (MZA) instability.

Additionally, we have studied the same system using a set of discrete velocities, where the $v = \pm 1$ case is the simplest example with $n_v = 1$ bins. We count the number of bins in the range $0 < v \leq 1$. In other words, there is an equal number of bins for negative velocities and the total number doubles for our two frequencies ($\varpi = \pm\varpi_0$). Adding the values $v = \pm 1/2$ takes us to $n_v = 2$, shown in the second panel of figure 6.2. It reveals that the hierarchies are not symmetric ($\mu \to -\mu$ symmetry) if the velocity range is non-trivial and that there are indeed two normal-hierarchy solutions. Increasing the bin number n_v eventually emulates the results from the uniform v distribution. A fairly small number of velocity bins is enough to achieve good agreement.

Inhomogeneous case ($k \neq 0$)

We will now "switch on" the instabilities, i.e., were are going to study the case where $k \neq 0$. The integrals for this setup are analytically solvable and are given in Appendix B. In Figure 6.3 we have plotted the results of our analysis. The left column we only show the result for the MZA. For small k, the instabilities shift to the left and their shape is slightly altered. For large k, the shifting scales almost linearly with k. In other words, the instability curves are very similar as a function of μ/k. The right panels show the results for the MAA and the bimodal instabilities in the ($\mu < 0$) and ($\mu > 0$) regions, respectively. The behavior of these solutions with the variation of k is very similar to the one observed for the MZA instabilities.

Including matter effects ($\bar{\lambda} \neq 0$)

Including matter in our "multi-zenith-angle" case has the effect of introducing both $\bar{\lambda}$ and k in the denominator of the integrals of Equation 6.4.8. The equations for the homogeneous ($k = 0$) are still analytically solvable and can be found in Appendix B. Once the inhomogeneities are "switched on", the system can no longer be solved analytically and the solutions have to be found numerically. As we will see, the effect of $\bar{\lambda}$ is very similar to the effect introduced by k: the unstable regions will get "stretched" to a broader range of μ values.

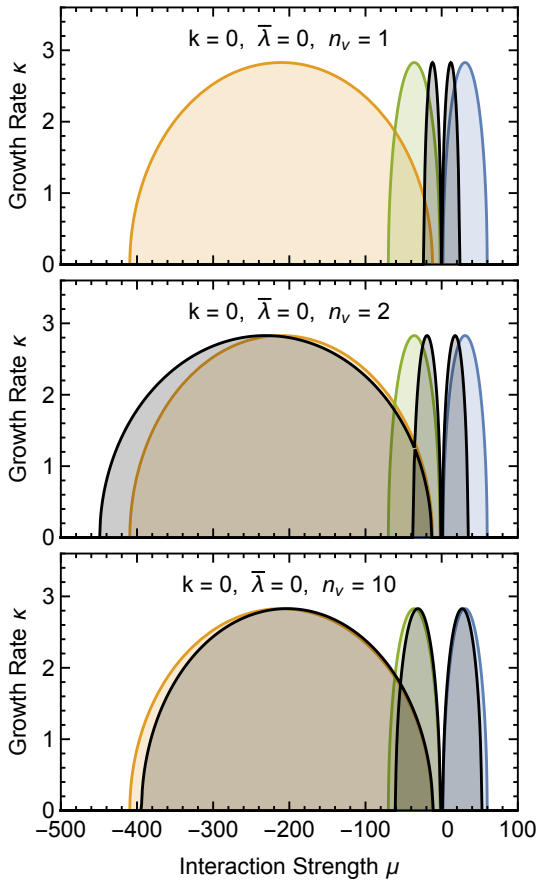

Figure 6.2: Growth rate κ for the unstable modes in the 1D multiangle case. k is set to zero, and $\alpha = 1/2$ obtained from Equation 6.4.10. The black lines represent the instability curves obtained using discrete beams, where the parameter n_v is the number of beams. With increasing number of beams, the discrete bins example recover a uniform distribution.

Homogeneous case ($k = 0$)

Let's begin with the homogeneous case ($k = 0$). The integrals $I_1 = I_3 = 0$, so the eigenvalue equation simplifies down to

$$\left[1 - \begin{pmatrix} I_2 & 0 & I_4 \\ 0 & -I_2 & 0 \\ I_0 & 0 & I_2 \end{pmatrix}\right] \begin{pmatrix} A_0 \\ A_1 \\ A_2 \end{pmatrix} = 0, \tag{6.4.11}$$

which lead to the following eigenvalue equations

$$(I_2 - 1)^2 = I_0 I_4, \tag{6.4.12}$$

$$I_2 = -1/2. \tag{6.4.13}$$

The results obtained from this equations are displayed in the contour plot of Figure 6.4. The results are plotted as a function of the effective matter density

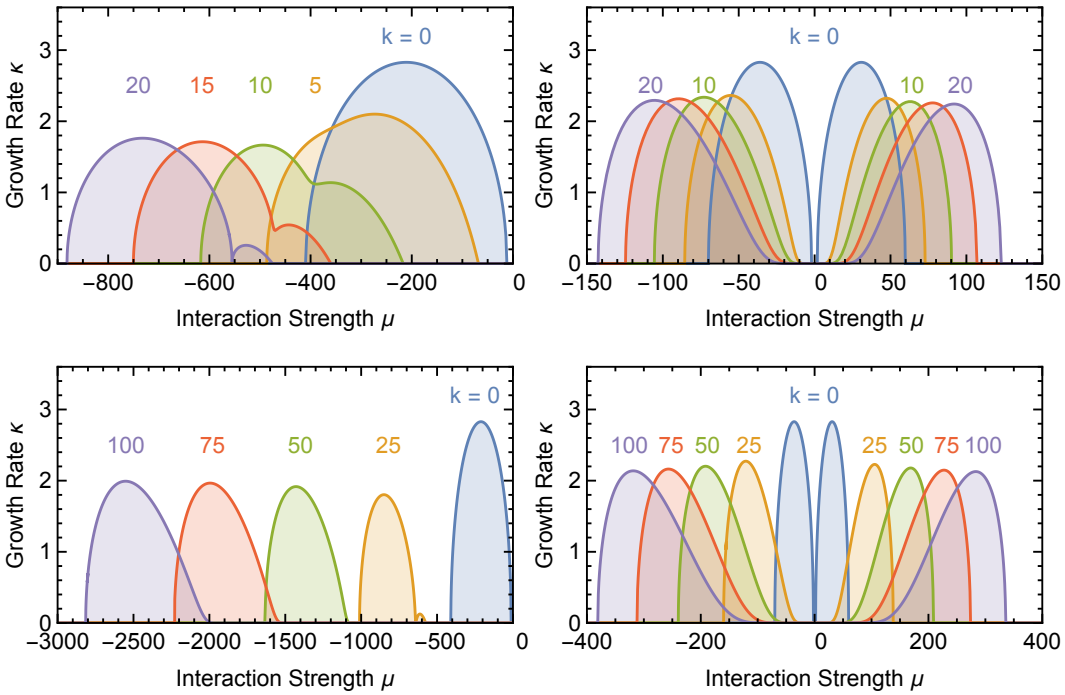

Figure 6.3: Growth rates κ for different k modes for the case without matter effects ($\bar{\lambda} = 0$). The curves are labeled with their wave number. The parameter α has been set to $\alpha = 1/2$. The left panels show only the MZA mode, in the right panels we show the MAA mode ($\mu < 0$) and the bimodal mode ($\mu > 0$). We can now see he effect of non-zero k: it shifts the curves to higher values of μ. For large k, the instability curves are similar as a function of μ/k.

$\bar{\lambda} = \lambda + \epsilon\mu$. Once again we assume $\alpha = 1/2$ and therefore $\epsilon = 1 - \alpha = 1/2$. The matter-free case ($\lambda = 0$) corresponds to the line $\bar{\lambda} = \mu/2$. The solutions shown in the upper panel are given by Equation 6.4.12 and correspond to the MZA ($\mu < 0$) and the bimodal ($\mu > 0$) instabilities. The solution in the lower panel is given by Equation 6.4.13, and correspond to the MAA instability. The effect of increasing $|\bar{\lambda}|$ is to shift the unstable solutions to regions of higher $|\mu|$. This creates a butterfly-shape in Figure 6.4.

Inhomogeneous case ($k \neq 0$)

Including matter in our multi-zenith-angle case has the effect of introducing both $\bar{\lambda}$ and k in the denominator of the integrals of Equation 6.4.8. As we have already discussed, there is a parallelisms in the way the system is affected when we add to the system inhomogeneities ($k \neq 0$) to the action of multi-matter effects ($\bar{\lambda} \neq 0$). The results are plotted in the butterfly diagram of Figure 6.5. This figure shows the $k = 0$ or homogenous case, which is the same information displayed in Figure 6.4 but in a logarithmic scale. Additionally, we have plotted the Fourier modes for $k = 0$, $k = 10^2$, $k = 10^3$ and $k = 10^4$, all of them labeled accordingly. Using the butterfly diagram given by Figure 6.5,

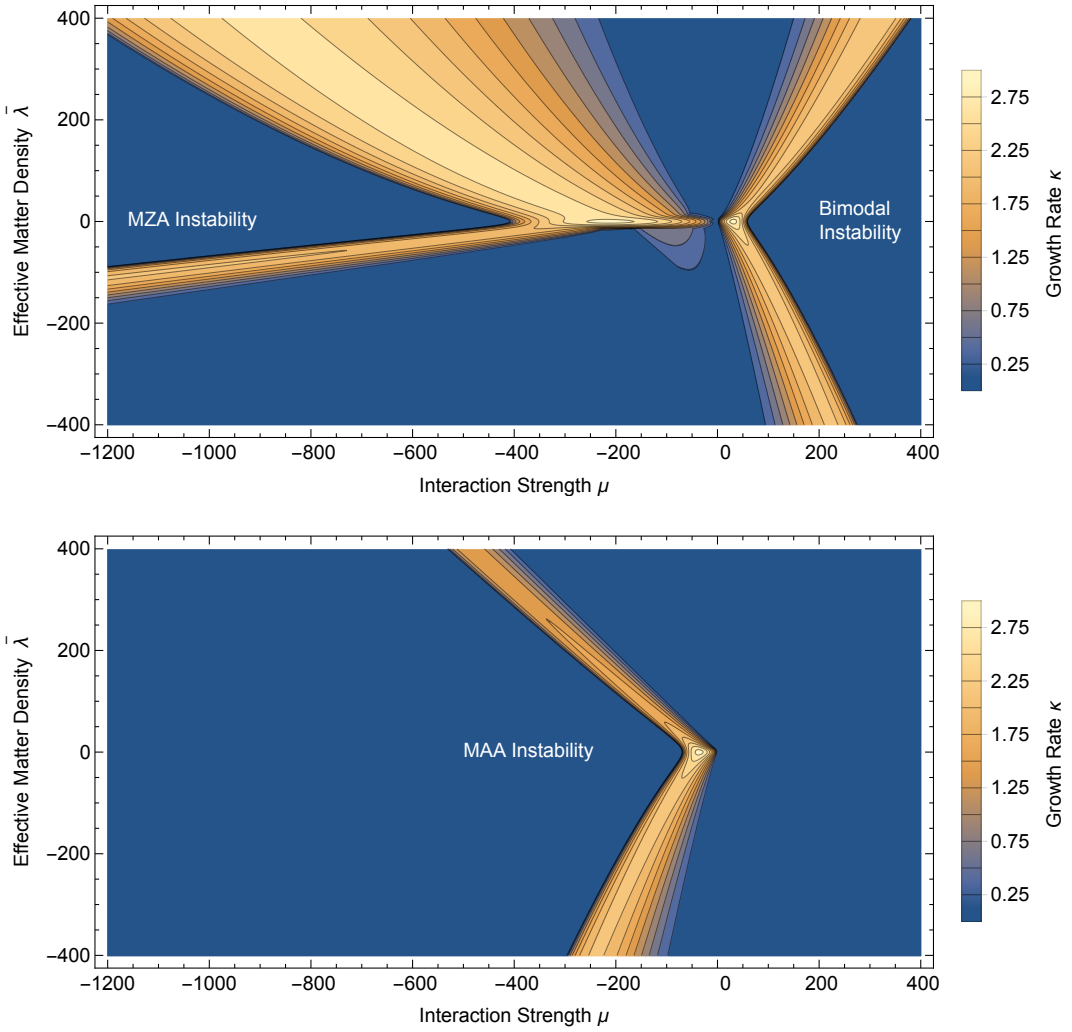

Figure 6.4: Growth rate κ of the 1D instabilities as a function of μ and $\bar{\lambda}$, assuming $\alpha = 1/2$. *Upper panel:* Equation (6.4.12) yields the bimodal instability for $\mu > 0$ and the multi-zenith-angle (MZA) instability for $\mu < 0$. *Lower panel:* Equation (6.4.13) provides the multi-azimuth-angle (MAA) instability for $\mu < 0$. Notice that $\mu > 0$ represents IO, whereas $\mu < 0$ represents NO.

we are now ready to asset the impact of the k modes in the system. Let's start by studying the two panels in the right column of the figure, which correspond to the second and third quadrants, i.e., the quadrants with $\mu > 0$. In essence, the small scale instabilities fill the space between the $k = 0$ or homogeneous solution footprints and the horizontal axis. The region above the homogeneous solution in the second quadrant and under the homogeneous solution remain stable. However, there is one caveat to this argumentation, which manifests itself in the upper panel. In this case, for large k modes, in the region where we have $k \sim \lambda$, there are "noses" which go beyond the homogeneous solution. The envelope of the noses exceeds slightly the $k = 0$ solution and expand to a region which was previously stable. The left column of the plot ($\mu < 0$) is a

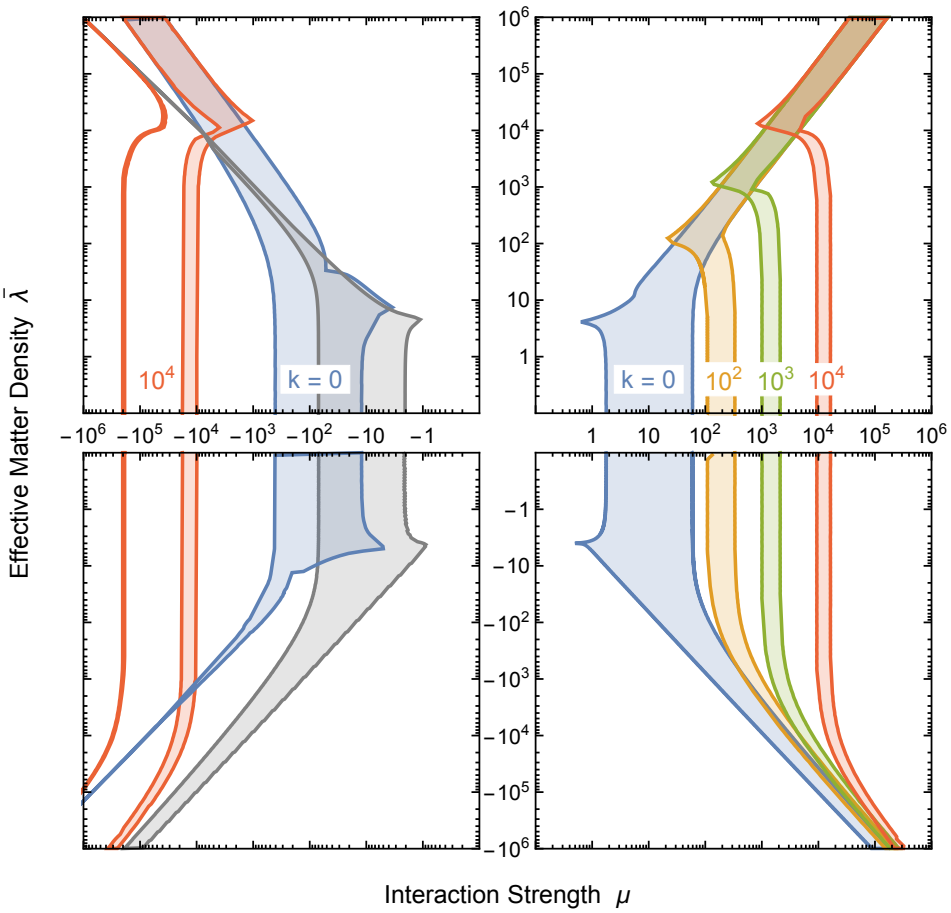

Figure 6.5: Butterfly diagram in the $\mu - \bar{\lambda}$ plane. The instabilities ($\kappa > 10^{-2}$) are plotted assuming $\alpha = 1/2$. The asymptotic behavior for large $\bar{\lambda}$ is explicitly derived in Appendix C.

bit more complicated because of the presence of two instabilities. In large k, the instabilities converge to the homogeneous solution in a crossed-over way. This effect is very clearly illustrated in the $k = 10^4$. In other words, the MZA and MAA are strongly mixed for large k.

Now that we have understood the physics of the one dimensional example, we will move on to a more realistic, two dimensional scenario. The way to proceed will be analogous to the one followed for the 1D example.

6.5 Two dimensional scenario

The two dimensional (2D) scenario can be understood as adding an additional degree of freedom to the two beam example. More precisely, we include the azimuth angle dependence in our EOM. By doing so, we restore the the traditional treatment of neutrinos streaming outside of the SN case. The radial evolution is parametrized by our time evolution, and the transverse directions

are enclosed in our spatial modes.

6.5.1 Single angle ($|\mathbf{v}| = 1$)

As in the 1D case, we start with the "single zenith angle case," meaning that the re-scaled neutrino speed within the transverse sheet is $|\mathbf{v}| = 1$. Moreover, the matter effect can be rotated away. Our velocity phase space is the unit circle, described by an angle variable φ which we can measure relative to $\mathbf{k}$. Because the system is initially prepared axially symmetric, the eigenvalues depend only on $k = |\mathbf{k}|$. The eigenvalue equation is now

$$(k\,c_\varphi + \varpi - \Omega)\,Q_{\Omega,k,\varpi,\varphi} = \mu \int_{-\infty}^{+\infty} d\varpi'\,h_{\varpi'}\,\frac{1}{2\pi}\int_{-\pi}^{+\pi} d\varphi'\,(1-c_\varphi c_{\varphi'}-s_\varphi s_{\varphi'})\,Q_{\Omega,k,\varpi',\varphi'}\,, \tag{6.5.1}$$

where $c_\varphi = \cos\varphi$ and $s_\varphi = \sin\varphi$. Exactly as we have done in previous cases, we notice that the r.h.s. of Equation (6.5.1) has the form $A_1 + A_\mathrm{c}\cos\varphi + A_\mathrm{s}\sin\varphi$, i.e., a superposition of three linearly independent functions on the interval $-\pi \leq \varphi \leq +\pi$. Therefore, the appropriate ansatz to solve this equation is

$$Q_{\Omega,k,\varpi,\varphi} = \frac{A_1 + A_\mathrm{c}c_\varphi + A_\mathrm{s}s_\varphi}{k\,c_\varphi + \varpi - \Omega}\,. \tag{6.5.2}$$

By inserting this form on both sides we arrive at three linearly independent equations, corresponding to the coefficients of the three functions 1, $\cos\varphi$ and $\sin\varphi$, which we express in a compact form as

$$\left[1 - \begin{pmatrix} I_1 & I_\mathrm{c} & 0 \\ -I_\mathrm{c} & -I_\mathrm{cc} & 0 \\ 0 & 0 & -I_\mathrm{ss} \end{pmatrix}\right] \begin{pmatrix} A_0 \\ A_\mathrm{c} \\ A_\mathrm{s} \end{pmatrix} = 0\,, \tag{6.5.3}$$

where the I_a are now defined as

$$I_a = \mu \int_{-\infty}^{+\infty} d\varpi\,h_\varpi \frac{1}{2\pi}\int_{-\pi}^{+\pi} d\varphi\,\frac{f_a(\varphi)}{k\,c_\varphi + \varpi - \Omega}\,. \tag{6.5.4}$$

Here, $f_1(\varphi) = 1$, $f_\mathrm{c}(\varphi) = \cos\varphi$, $f_\mathrm{cc}(\varphi) = \cos^2\varphi$, and $f_\mathrm{ss}(\varphi) = \sin^2\varphi$. The zero entries are due to the fact that the integrals with a single power of $\sin\varphi$ vanish when we integrate in the interval $(-\pi, \pi)$. We also note that $I_\mathrm{ss} = I_1 - I_\mathrm{cc}$, so we need only three different integrals.

Homogeneous ($k = 0$)

We will start with the homogeneous case ($k = 0$). This implies that the term proportional to c_φ is zero, and therefore we can perform all the φ integrals explicitly. Using the monochromatic spectrum given by Equation 6.3.6, the eigenvalues are

$$\det\left[\varpi_0^2 - \Omega^2 - \mu \begin{pmatrix} 1 & 0 & 0 \\ 0 & -\frac{1}{2} & 0 \\ 0 & 0 & -\frac{1}{2} \end{pmatrix} [(1+\alpha)\,\varpi_0 + (1-\alpha)\,\Omega]\right] = 0\,. \tag{6.5.5}$$

There are three independent equations in this case. The first one corresponds to the usual bimodal solutions, whereas the are the degenerate multi-azimuthal-angle (MAA) solutions which are unstable for negative μ (NO). these modes, the instability range is a factor of 2 larger.

Inhomogeneous ($k \neq 0$)

For the inhomoegeous case ($k \neq 0$), the integrals of Equation 6.5.4 are no longer so simple to solve. Instead, we obtain

$$I_a = \frac{\mu}{k}\int_{-\infty}^{+\infty} d\varpi\, h_\varpi F_a\left(\frac{\varpi-\Omega}{k}\right) \quad \text{where} \quad F_a(w) = \frac{1}{2\pi}\int_{-\pi}^{+\pi} d\varphi\, \frac{f_a(\varphi)}{\cos\varphi + w}\,. \tag{6.5.6}$$

With our monochromatic spectrum equation (6.3.6) we arrive at

$$I_a = \frac{\mu}{k}\left[F_a\left(\frac{\varpi_0-\Omega}{k}\right) - \alpha\, F_a\left(\frac{-\varpi_0-\Omega}{k}\right)\right]. \tag{6.5.7}$$

We define the auxiliary function of a complex argument w

$$s(w) = \sqrt{w-1}\sqrt{w+1}\,, \tag{6.5.8}$$

which, for complex numbers, is in general not equal to $\sqrt{w^2-1}$. We then find

$$F_1 = \frac{1}{s(w)}\,, \quad F_{\rm c} = 1-\frac{w}{s(w)}\,, \quad F_{\rm cc} = -w+\frac{w^2}{s(w)}\,, \quad F_{\rm ss} = F_1 - F_{\rm cc} = w - s(w)\,. \tag{6.5.9}$$

These expressions allow us to write the eigenvalue equations explicitly, involving only polynomials and square-root expressions. We now have three non-degenerate solutions, in contrast to the original 1D. One solution for $\mu > 0$ (IO) and two for $\mu < 0$ (NO). The solution given by the 2×2 ss-block equation leads to a much more complicated equation. This solution is explicitly

$$\begin{aligned}(1+\alpha)\varpi_0 - (1-\alpha)\Omega + \alpha\sqrt{-k-\varpi_0-\Omega}\sqrt{k-\varpi_0-\Omega} \\ -\sqrt{-k+\varpi_0-\Omega}\sqrt{k+\varpi_0-\Omega} = -\frac{k^2}{\mu}\,.\end{aligned} \tag{6.5.10}$$

This solution is a genuine result of the spatial 2D geometry with non-vanishing wave-vector $\mathbf{k}$. The eigenfunctions in this case are proportional to $\sin\varphi$ where φ is the angle between $\mathbf{k}$ and the velocity $\mathbf{v}$ of a given mode. We show contour plots of the growth rate κ as a function of μ and k for our usual example $\alpha = 1/2$ in Figure 6.6.

6.5.2 Multi-angle ($0 \leq v \leq 1$)

The last step in our road to understand the SN-type scenario is by promoting our 2D scenario into a "multi-zenith" angle case, i.e., by considering the velocities to vary in the disk given by $|\mathbf{v}| < 1$. The angle φ is

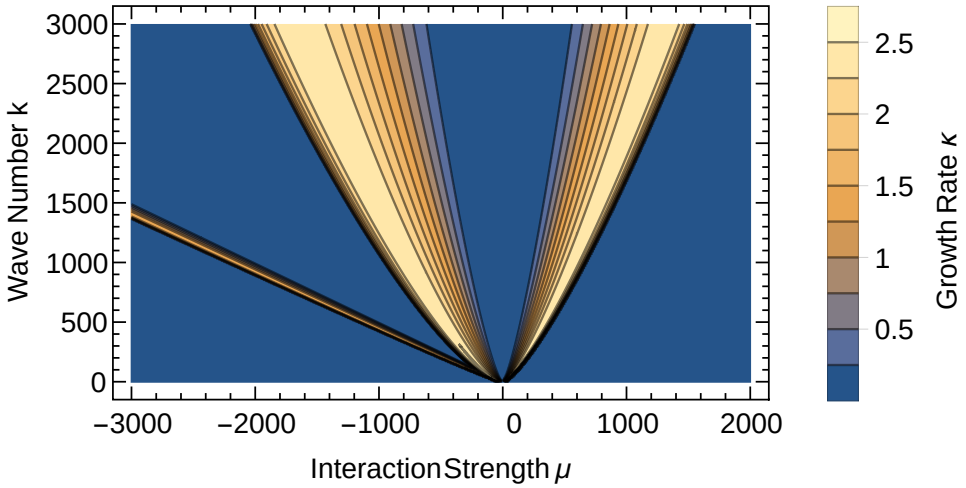

Figure 6.6: Growth rate for the 2D inhomoegeous ($k \neq 0$) case without matter effects ($\bar{\lambda} = 0$), using $\alpha = 1/2$. The two central solutions already appeared in the 1D case, where the unstable μ region scales as $k^{3/4}$. For the third solution, the unstable region for μ scales linearly with k. This third solution for $\mu < 0$ is a distinctive feature of the 2D configuration.

the angle between the velocity vector and the wave vector $\mathbf{k}$. Noting that $(1/\Gamma_{\mathbf{v}}) \int d\mathbf{v} = (1/\pi) \int_{-\pi}^{+\pi} d\varphi \int_0^1 dv\, v$, and the eigenvalue equation is now

$$\left(\tfrac{1}{2}\bar{\lambda}v^2 + k\, v\, c_\varphi + \varpi - \Omega\right) Q_{\Omega,k,\varpi,v,\varphi} =$$

$$\mu \int_{-\infty}^{+\infty} d\varpi'\, h_{\varpi'} \int_{-\pi}^{+\pi} \frac{d\varphi'}{\pi} \int_0^1 dv'\, v' \left[D_{v,v'} - vv'\, L_{\varphi,\varphi'}\right] Q_{\Omega,k,\varpi',v',\varphi'}\,, \quad (6.5.11)$$

where $L_{\varphi,\varphi'} = c_\varphi c_{\varphi'} + s_\varphi s_{\varphi'}$ and $D_{v,v'} = 1/2(v'^2 + v^2)$. The r.h.s. of this equation is now proportional to four linearly independent terms, namely A_0, $A_2 v^2$, $A_c \mathrm{c}_\varphi v$ and $A_s \mathrm{s}_\varphi v$. The appropriate ansatz for this equation is

$$Q_{\Omega,k,\varpi,v,\varphi} = \frac{A_0 + A_2 v^2 + A_c \mathrm{c}_\varphi v + A_s \mathrm{s}_\varphi v}{\frac{1}{2}\bar{\lambda} + kv\mathrm{c}_\varphi + \varpi - \Omega}. \quad (6.5.12)$$

As in the previous cases, we introduce this ansatz in both sides of Equation 6.5.11, and arranging the terms proportional to the coefficients, we obtain

$$\left[1 - \begin{pmatrix} I_3^1 & I_5^1 & I_4^c & 0 \\ I_1^1 & I_3^1 & I_2^c & 0 \\ -2I_2^c & -2I_4^c & -2I_3^{cc} & 0 \\ 0 & 0 & 0 & -2I_3^{ss} \end{pmatrix}\right] \begin{pmatrix} A_0 \\ A_2 \\ A_c \\ A_s \end{pmatrix} = 0, \quad (6.5.13)$$

where we have used that all terms proportional to $\int \mathrm{s}'_\varphi d\varphi'$ are zero. The integrals I_n^a are now defined as

$$I_n^a = \mu \int_{-\infty}^{+\infty} d\varpi\, h_\varpi \int_{-\pi}^{+\pi} \frac{d\varphi}{2\pi} \int_0^1 dv\, \frac{v^n\, f_a(\varphi)}{\frac{1}{2}\bar{\lambda}v^2 + k\, v\, c_\varphi + \varpi - \Omega}\,. \quad (6.5.14)$$

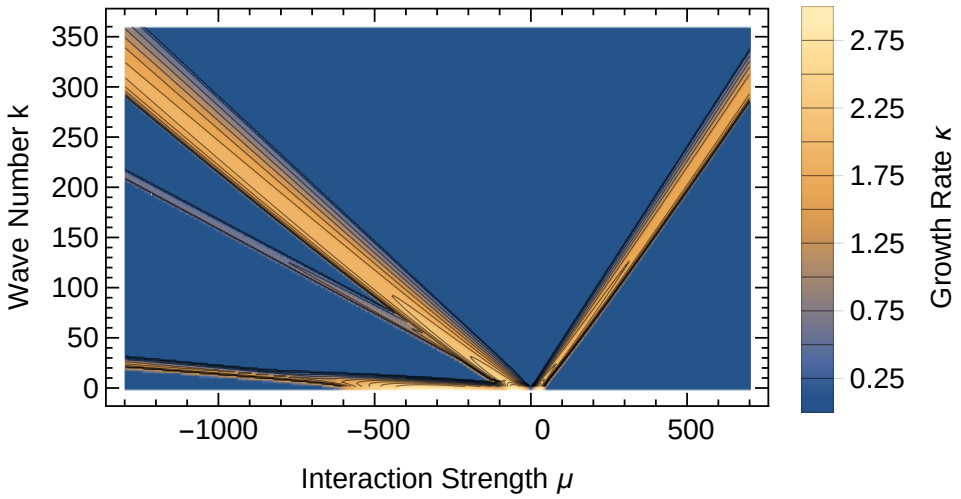

Figure 6.7: Growth rate for the 2D inhomoegeous case without matter effects ($\bar{\lambda} = 0$). The parameter α is set to $\alpha = 1/2$. This plot is the multiangle ($0 < |\mathbf{v}| < 1$) version of Figure 6.6. As we can see, there are three solutions now for the NO case ($\mu < 0$) plus the bimodal solution for the IO ($\mu > 0$) case. Unlike in the single angle case, the range of unstable μ for all four solutions grows linearly with k.

Here, $f_1(\varphi) = 1$, $f_c(\varphi) = \cos\varphi$, $f_{cc}(\varphi) = \cos^2\varphi$, and $f_{ss}(\varphi) = \sin^2\varphi$. We also note that $I_3^{ss} = I_3^1 - I_3^{cc}$.

Including matter effects ($\bar{\lambda} \neq 0$), homogeneous ($k = 0$)

Lets start with the homogeneous case ($k = 0$). For this situation, thee integrals $I_1 = I_3 = 0$, so that the Equation 6.5.13 reduces to

$$\left[1 - \begin{pmatrix} I_3 & I_5 & 0 & 0 \\ I_3 & I_5 & 0 & 0 \\ 0 & 0 & -I_3 & 0 \\ 0 & 0 & 0 & -I_3 \end{pmatrix}\right] \begin{pmatrix} A_0 \\ A_2 \\ A_c \\ A_s \end{pmatrix} = 0, \tag{6.5.15}$$

which lead to the following eigenvalue equations: the 2×2 block leads us two the eigenvalue equation

$$(I_2 - 1)^2 = I_1 I_5, \tag{6.5.16}$$

which gives us the MZA and the instabilities. Besides this equation, we have to degenerate equations of the form

$$I_3 = -1, \tag{6.5.17}$$

which will give us the MAA instability. The results obtained from these equations are displayed in the contour plot of Figure 6.8, where the growth rate κ

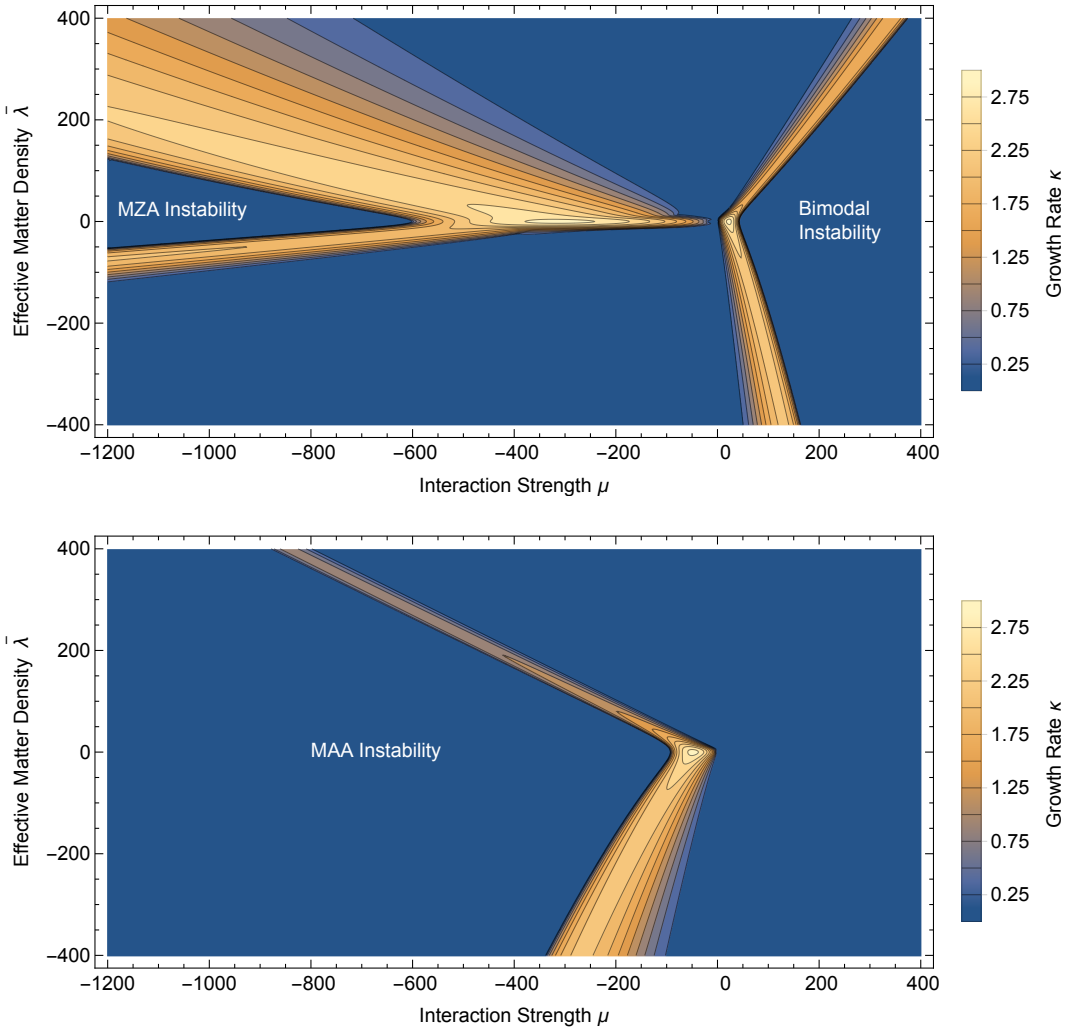

Figure 6.8: Growth rate κ of the 2D instabilities as a function of μ and $\bar{\lambda}$, assuming $\alpha = 1/2$. *Upper panel:* The Equation 6.4.12 yields the bimodal instability for $\mu > 0$ (IO) and the multi-zenith-angle (MZA) instability for $\mu < 0$ (NO). *Lower panel:* Equation 6.4.13 provides the multi-azimuth-angle (MAA) instability for $\mu < 0$. This figure is analogous to the corresponding 1D case shown in Figure 6.4.

is plotted as a function of the effective matter potential $\bar{\lambda}$ and the interaction strength μ. The results are very similar to the analogous 1D case (Figure 6.4). Again, for $\mu > 0$, we obtain the bimodal instability, and for $\mu < 0$, the MZA and MAA instabilities.

Inhomogeneous ($k \neq 0$) without matter ($\bar{\lambda} = 0$) case

Next we consider the case of $k \neq 0$ without matter. We may write the integrals of Equation 6.5.11 in the form

$$I_n^a = \frac{\mu}{k} \int_{-\infty}^{+\infty} d\varpi \, h_\varpi \, K_n^a \,, \quad \text{where} \quad K_n^a = \int_{-\pi}^{+\pi} \frac{d\varphi}{2\pi} \int_0^1 dv \, \frac{v^n \, f_a(\varphi)}{v \, c_\varphi + w}, \quad (6.5.18)$$

and we have introduced $w = (\varpi - \Omega)/k$. We find explicitly

$$K_1^1 = w + \frac{\sqrt{1-w}\sqrt{-w(1+w)}}{\sqrt{w}} \,, \quad (6.5.19a)$$

$$K_3^1 = \frac{2w^3}{3} + \frac{\sqrt{-w}\sqrt{1-w^2}\,(1+2w^2)}{3\sqrt{w}} \,, \quad (6.5.19b)$$

$$K_5^1 = \frac{8w^5}{15} + \frac{\sqrt{-w}\sqrt{1-w^2}\,(3+4w^2+8w^4)}{15\sqrt{w}} \,, \quad (6.5.19c)$$

$$K_2^{\mathrm{c}} = \frac{1}{2} - w^2 - \sqrt{-w^2}\sqrt{1-w^2} \,, \quad (6.5.19d)$$

$$K_4^{\mathrm{c}} = \frac{1}{4} - \frac{2w^4 + \sqrt{-w^2}\sqrt{1-w^2}\,(1+2w^2)}{3} \,, \quad (6.5.19e)$$

$$K_3^{\mathrm{cc}} = -w \left(\frac{1}{2} - w^2 - \sqrt{-w^2}\sqrt{1-w^2} \right) , \quad (6.5.19f)$$

$$K_3^{\mathrm{ss}} = \frac{w(3-2w^2)}{6} + \frac{\sqrt{-w}(1-w^2)^{3/2}}{3\sqrt{w}} \,. \quad (6.5.19g)$$

Notice that $K_3^{ss} + K_3^{cc} = K_3^1$.

With the help of these analytic integrals we can solve the eigenvalue equation numerically. The results are plotted in Figure 6.9. This figure shows a contour plot of the growth rate κ in the μ-k-plane. The 3×3 block in Equation 6.5.13 provides three different solutions, i.e., one for $\mu > 0$ (the usual bimodal solution in IO) and two solutions for $\mu < 0$ (NO). Furthermore, the 1×1 block provides an extra solution for $\mu < 0$. Figure 6.9 corresponds to Figure 6.6 in the single-angle case. We observe that in this case we have one more instability, which makes a total number of four instabilities for the 2D scenario. Moreover, the new solution appears only for $\mu < 0$ (NO).

Matter effects ($\bar{\lambda} \neq 0$) and inhomogeneities ($k \neq 0$)

Now, after having worked out all the intermediate steps, we are able to plot a butterfly diagram for the 2D model with matter ($\bar{\lambda} > 0$) and inhomogeneities ($k > 0$). We need to find the zeros of the determinant in Equation 6.5.11 and write the integrals in the form

$$I_n^a = \frac{\mu}{\bar{\lambda}} \int_{-\infty}^{+\infty} d\varpi \, h_\varpi \, K_n^a \,, \quad \text{where} \quad K_n^a = \int_{-\pi}^{+\pi} \frac{d\varphi}{2\pi} \int_0^1 dv \, \frac{v^n \, f_a(\varphi)}{v^2/2 + q \, v \, c_\varphi + w} \,, \quad (6.5.20)$$

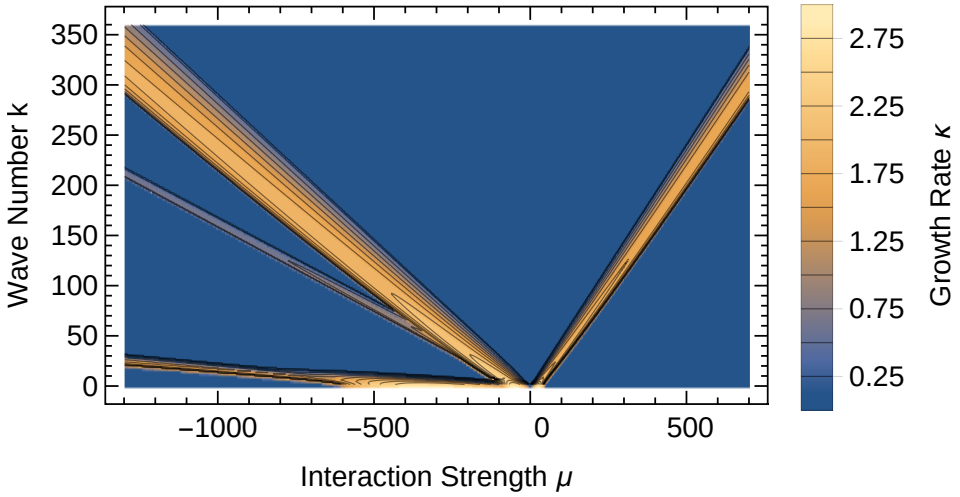

Figure 6.9: Growth rate for the 2D inhomoegeous case without matter effects ($\bar{\lambda} = 0$). The parameter α is set to $\alpha = 1/2$. This plot is the multiangle ($0 < |\mathbf{v}| < 1$) version of Figure 6.6. As we can see, there are three solutions now for the NO case $\mu < 0$) plus the bimodal solution for the IO ($\mu > 0$) case. Unlike in the single angle case, the range of unstable μ for all four solutions grows linearly with k.

with $q = k/\bar{\lambda}$ and $w = (\varpi - \Omega)/\bar{\lambda}$. These integrals can be solved analytically; we provide our results in Appendix B.

The results are shown in Figure 6.10. The results are very similar to the 1D case. However, there is a difference for the region $\mu < 0$. In this case, we have an extra solution. This extra solution merges with one of the others for $\bar{\lambda} \gg k$. Moreover, for large k, one of the solutions cease to produce unstable eigenvalues and we return to the three-solution framework. We also notice that the unphysical third quadrant shows more pronounced noses compared to the 1D solution.

Besides these technical details, the main message remains unaffected with respect to the 1D case. Again, the role of the small scale modes is to "fill" the space between the homogeneous solution and the horizontal axis, whereas the space between the $k = 0$ solution and the vertical axis remains to be free of instabilities.

6.6 Summary of the 2D analysis

We now try summarize the information about the effects of the k modes in the 2D scenario and try to assess the impact of the small scale inhomogeneities in a realistic SN scenario. To this end, we have plotted the footprint diagram [3] given in Figure 6.11. This figure essentially contains the information displayed in the

[3]There is detailed discussion about footprint diagrams in Appendix D

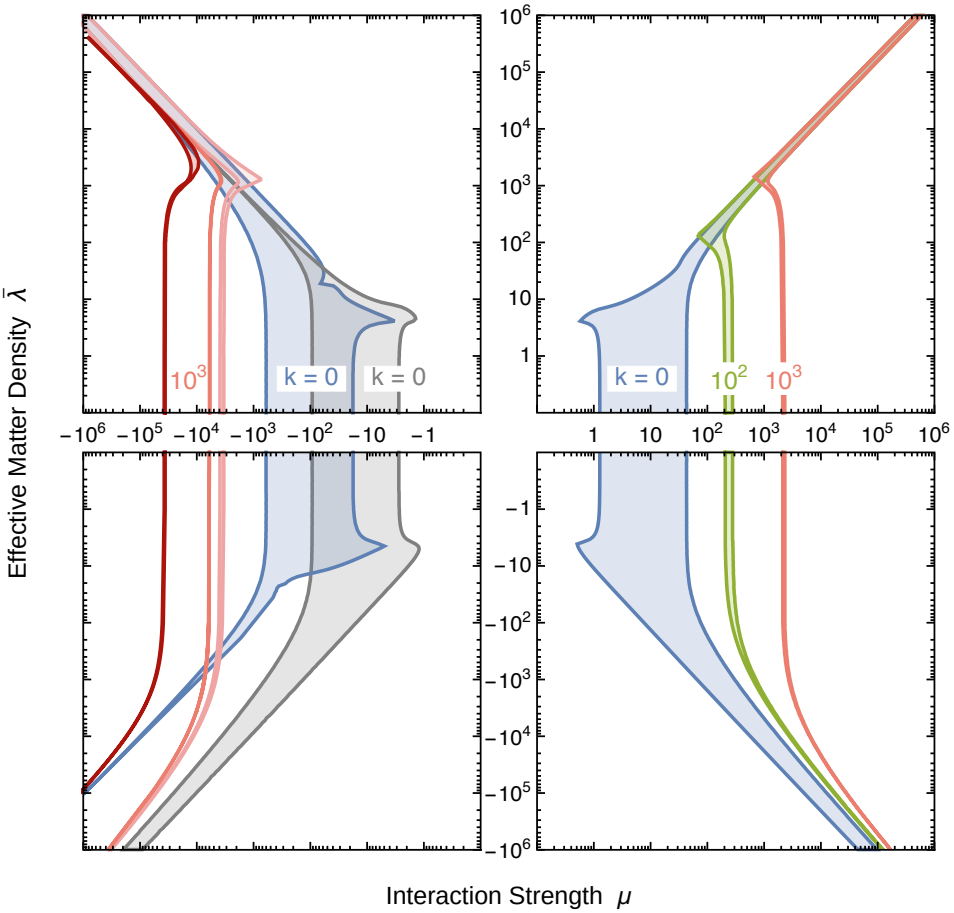

Figure 6.10: Footprint of the 2D instability region ($\kappa > 10^{-2}$) in the parameter space of $\mu - \lambda$. For this plot, we have assumed $\alpha = 1/2$. The different k modes are plotted in different colors. The asymptotic behaviors are explained in Appendix C.

third quadrant of Figure 6.10. Once again, the instability regions correspond to values of the growth rates $\kappa > 10^{-2}\varpi$. We have plotted as a solid red line, a possible SN matter density profile given by the simulation of a 15 $M_\odot$ progenitor, corresponding to electron density as function of radius. In this particular example, the density profile does not intersect with the instability footprint for radii below the shock wave. On the other hand, for larger radii, the density profiled crosses indeed the instability region for the $k = 0$ mode. We have also plotted the footprint for inhomogeneities with assumed wave-number $k = 10^2$ and $k = 10^3$, measured in units of the vacuum oscillation frequency ϖ. Note we are plotting the MAA instability, which is relevant for NO, non-zero k values lead to *two* unstable solutions, whereas for the bimodal instability there is only *one*. The full range of all k-values basically fills the entire region below the homogeneous $k = 0$ mode (blue shading) in this plot, i.e., the entire gray-shaded region is unstable. Meanwhile, the region above the blue-shaded part remains intact. The main conclusion that can be extracted from this

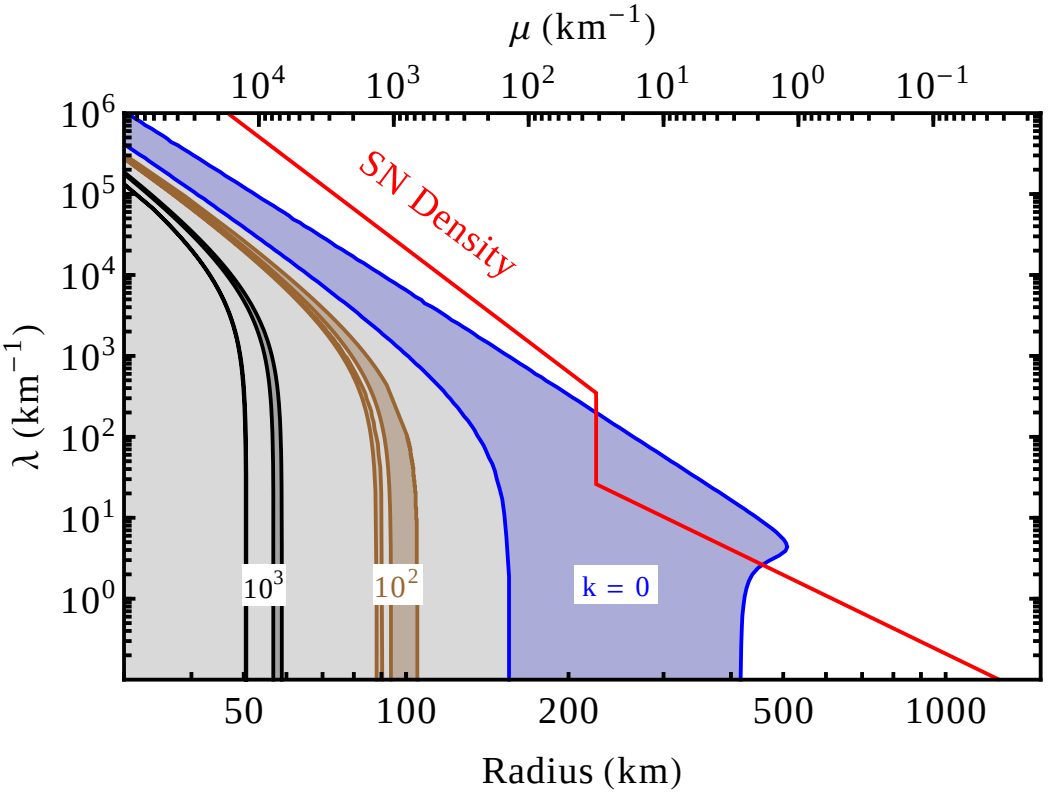

Figure 6.11: Footprint of the MAA instability region in the parameter space of effective neutrino density $\mu = \sqrt{2}G_{\rm F}n_{\nu_e}(R/r)^2$, where R is the neutrino-sphere radius, and matter density $\lambda = \sqrt{2}G_{\rm F}n_e(R/r)^2$ for the schematic SN model described in the text [1]. The neutrino density decreases $\propto r^{-4}$, so we can plot the distance to the center of the SN in the x axis. The SN matter profile is taken from the simulation of 15 $M_\odot$ progenitor at $t = 200$ ms after the core bounce [66]. The sharp density drop is the shock-wave front. The $k = 0$, i.e., homogeneous instability regions is plotted as the blue shadowed region. We also show the instability footprint explicitly for wave numbers $k = 10^2$ and $k = 10^3$, all in units of the vacuum oscillation frequency. The $k > 0$ modes, i.e., the small scale instabilities fill the space between the vertical axes and the homogeneous regions (gray shadowed region), but never exceeding it.

study is that multi-matter effects "shift" the instability regions far from the SN density profile. Indeed, the higher the order of k, the deeper the instabilities are shifted. It is not that the matter effects erases the unstable regions; they are simply shifted to harmless regions of the parameter space. Therefore, the largest-scale mode $k = 0$, which corresponds to the homogeneous scenario, is the most interesting one from the point of view of stability analysis: if this mode is stable, the higher-k modes are stable as well.

6.7 Summary

Using the EOM developed in Chapter 4 and in Chapter 5, we have adopted it to the bulb geometry. We have assumed a stationary system and restricted our analysis to the spatial evolution. Moreover, we have assumed that the system is inhomogeneous in the perpendicular direction.

Because of the mathematical complexity of the eigenvalue equation, we could not solve the whole problem at once. Instead, we have started from a very simple setup which consists on a 1D model. We have started studying the system without matter or k modes, and we have included these effects progressively in the course of the chapter. After we have added both matter and the inhomogeneities, we have arrived to the butterfly diagram displayed in Figure 6.5. The conclusion of the study was the effect of the k modes is shift of the unstable modes analogous to the shift produced by multi-matter effects.

Once we have understood the role of the k modes in the 1D scenario, we have performed the same steps for a 2D setup and we have arrived at a butterfly diagram for the 2D scenario. In this case, the results where analogous to the 1D scenario, where again the k modes shift the instability curves is an similar way the matter does.

The last step of our study consisted on plotting the 2D results in a footprint diagram, where we have included as well a SN profile of a 1D simulation of a 15 $M_\odot$ progenitor 200 ms after core-bounce. The conclusion of the analysis is that the multi-angle matter effects present in the SN-type environments shifts unstable modes created by the small scales inhomogeneities (k modes) to regions of the parameter space that are not met by the SN's matter profile. Therefore, the most "dangerous" or prone-to-instabilities case is the homogeneous one. Therefore, assuming homogeneity in the perpendicular direction not only will simplify the equations but also corresponds to the most interesting case from the perspective of linearized stability analysis.

Nonetheless, we have to be very careful when we interpret these results. There have been many assumptions made for this analysis. We have assumed that the system is stationary and restricted the study to the spatial evolution. Furthermore, the angular distributions for both neutrino species are taken to be the same, which is not the case in a realistic SN. Because of the numerous assumptions and simplifications applied, this mathematical model might not capture important aspects of a realistic SN environment. This will be precisely the task of our next chapter, where some of these assumptions will be dropped and we will investigate the consequences.

Chapter 7

Dispersion relation formalism applied to SN scenarios

In this chapter, we will continue to study SN-type scenarios, but we will drop some of the previous assumptions. The starting point is the equation of motion (EOM) adapted to the bulb geometry. We will restrict our study to the homogeneous scenario for the reasons argued in the last chapter. Moreover, the whole analysis will be done considering the massless neutrino case. This chapter is based in the results contained in References [2, 4].

As a first step, we will continue to assume stationarity. However, we will drop the assumption that the angular distributions for neutrinos and antineutrinos are the same. In other words, neutrinos are carrying non-zero electron lepton number (ELN) out from the SN. This will prove to have huge impact in the solutions and we will find a completely new phenomenology in core-collapse SN-type scenarios. More precisely, the solutions will include fast oscillating modes, where the instability growth rate is proportional to the neutrino number density n_ν instead of proportional to the vacuum oscillation frequency ϖ. Because these kind of solutions appear under the assumption of massless neutrinos, we will have flavor conversion without flavor mixing. This is the first time that such a phenomenon appears when considering realistic SN scenarios.

The next step will be to dismiss the stationarity. By doing so, we can apply the full dispersion relation (DR) machinery to an ELN angular distribution obtained from a 1D core-collapse SN simulation. We then study the types of "forbidden" regions that arise from the DR equation. The next step will be to study a collection of angular distributions obtained from 1D SN models using different masses for the stellar progenitors. From these angular distributions we can study the implications for the DR diagram. Finally, we will briefly study a particular type of astrophysical objects which is particularly interesting. These objects are compact binary-merger remnants. We will discuss their characteristic angular neutrino emission, and study their temporal and spatial evolution.

7.1 The two-bulb neutrino scenario

7.1.1 Description of the system

The previous chapter was devoted to the study of the EOM derived in Chapter 5 adapted to the bulb geometry in a stationary scenario where the perpendicular direction was inhomogeneous. Moreover, the angular distribution for both neutrinos and antineutrinos were assumed to be equal. For the present chapter, we will continue to use the bulb geometry, but we will assume homogeneity in the perpendicular direction ($k_x = 0$), which corresponds to the most "dangerous" case, as we have already discussed. Moreover, we will maintain the stationarity assumption.

Under these assumptions, neutrinos emerge from a spherical surface and the neutrino field at some observation point over the neutrino sphere is fully described by the azimuth angle φ and the variable $u = \sin^2(\theta)$, where θ is the zenith angle. The range of occupied zenith angles for the ν_e and $\bar{\nu}_e$ distributions are normalized to some reference radius, so that the range of occupied u is independent of the test radius used for the stability analysis.

The key feature is that we will now assume different angular distributions for ν_e and $\bar{\nu}_e$, or, in other words, we will consider that neutrinos are carrying an effective ELN out from the SN. This assumption, when working in the SN-type scenario, corresponds to assuming a different neutrino sphere for each neutrino species. Because we are considering only ν_e and $\bar{\nu}_e$, we will work with two neutrino spheres, i.e., "two-bulbs".

This model was first introduced in Reference [67]. The angular distributions are pictorially displayed in Figure 7.1. As mentioned in Chapter 2 and Chapter 3, this assumption is physically motivated due to the weaker interaction strength with matter of $\bar{\nu}_e$ with respect to ν_e. This translates into a smaller neutrino sphere for $\bar{\nu}_e$, which induces a broader angular velocity distribution for the emitted spectra of ν_e.

The eigenfunctions for the homogeneous case were already derived in Chapter 5, but we will write them down here again for clarity. These are

$$I_1^2 - (I_0 - 1)(I_2 + 1) = 0, \tag{7.1.1}$$

$$I_2 - I_0 = 2, \tag{7.1.2}$$

where the I_n are

$$I_n = \mu \int d\varpi \; du \frac{u^n G(\varpi, u)}{\varpi + u\bar{\lambda} - \Omega}, \tag{7.1.3}$$

where the matter potential is $\bar{\lambda} = \lambda + \mu\epsilon$, ϵ is the neutrino-antineutrino asymmetry, $\lambda = \sqrt{2} G_{\rm F} n_e$ is the matter effect, $\mu = \sqrt{2} G_{\rm F} n_\nu$ is the typical neutrino-neutrino interaction energy, and Ω is the eigenvalue of the flavor modes.

For convenience can introduce the ϖ-integrated zenith-angle distributions

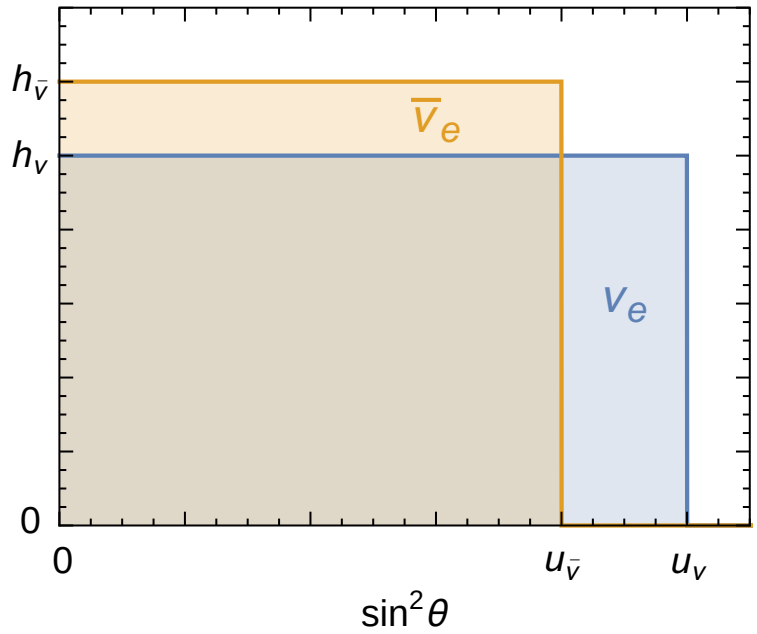

Figure 7.1: Zenith-angle distribution for neutrinos (blue) and antineutrinos (orange) in the two-bulb neutrino model [2]. Note the wider range of emission for the neutrino distribution.

for ν_e and $\bar{\nu}_e$

$$h_{\nu_e}(u) = + \int_0^{\infty} d\varpi G(\varpi, u), \tag{7.1.4}$$

$$h_{\bar{\nu}_e}(u) = - \int_{-\infty}^{0} d\varpi G(\varpi, u). \tag{7.1.5}$$

We adopt now the limit of massless neutrinos, i.e., $\varpi = \Delta^2/(2E) = 0$. Under this assumption, the contributions to $G(\varpi, u)$ from ν_x and $\bar{\nu}_x$ drop if their angular distributions are the same. For this reason we can simply consider that the emission of ν_x and $\bar{\nu}_x$ are zero. Note however that they play a role in the system because they are present in the definitions of μ and ϵ. Moreover, we can particularize ϵ to this specific setup, obtaining

$$\epsilon = \int du \left(h_{\nu_e} - h_{\bar{\nu}_e}\right). \tag{7.1.6}$$

Using these definitions and after performing the ϖ integration, we can express the integrals terms give by Equation 7.1.3 as

$$I_n = \int du \frac{u^n}{u(\epsilon + m) - w} \left[h_{\nu_e}(u) - h_{\bar{\nu}_e}(u)\right], \tag{7.1.7}$$

where the parameter m is defined $m = \lambda/\mu$ and $w = \Omega/\mu$ is the normalized eigenvalue.

We can now particularize these equations to the two-bulb model. This model implies the top-hat angular distributions given in Figure 7.1. The u-ranges occupied by the neutrino and antineutrino distributions are $u_{\nu_e} = 1+b$ and $u_{\bar{\nu}_e} = 1-b$, respectively. In this language, the "traditional" one bulb model corresponds to $b = 0$. However, for the SN motivated scenario, where neutrinos decouple at larger distances, we find $b > 0$. On the other hand, the number densities for the neutrino and antineutrino distributions are defined as $n_{\nu_e} = 1 + a$ and $n_{\bar{\nu}_e} = 1 - a$, respectively. The quantity a parameterizes the neutrino-antineutrino asymmetry of the system and is constrained in the range $-1 < a < +1$. Inside SNe, due to deleptonization, there is an excess of ν_e over $\bar{\nu}_e$. In other words, in such environments we find $a > 0$. To sum up, the conditions inside a SN impose that a and b must be greater than zero. The angular distributions as a function of the parameters a and b are

$$h(u) = \frac{1 \pm a}{1 \pm b} \times \begin{cases} 1, & \text{for } 0 \leq u \leq 1 \pm b, \\ 0, & \text{otherwise,} \end{cases} \tag{7.1.8}$$

where the positive sign corresponds to ν_e and the negative one to $\bar{\nu}$. After inserting these angular distributions in Equation 7.1.7, we arrive at

$$I_n = \frac{1+a}{1+b} \int_0^{1+b} du \frac{u^n}{u(2a+m) - w} - \frac{1-a}{1-b} \int_0^{1-b} du \frac{u^n}{u(2a+m) - w}, \tag{7.1.9}$$

where we we have used $\epsilon = 2a$. The simplicity of these integrals makes them analytically solvable.

The case where $b = 0$ is especially interesting. In this case, both distributions have the same width, although their number densities are different ($a \neq 0$). For this situation, the integrals reduce to

$$I_n = 2a \int_0^1 du \frac{u^n}{u(2a+m) - w}. \tag{7.1.10}$$

The interesting feature of this particular case is that, when solving the equations, the eingenvalues obtained do not have an imaginary part. In other words, the system is stable. This interesting behavior illustrates how imposing an unphysical condition, i.e., the angular distributions for ν_e and $\bar{\nu}_e$ having the same width, can lead to unphysical results.

7.1.2 Solutions without matter effect

In order to get a first glimpse of the consequences of the non-zero ELN carried by neutrinos, we can set the matter effects to zero by setting the parameter $m = 0$ in the denominator of the integral terms of Equation 7.1.9. As in other previously discussed cases, the eigenvalue equations are too complicated from the algebraic point of view to extract information from the analytical result. Therefore, it is more illustrative to solve the equations numerically and

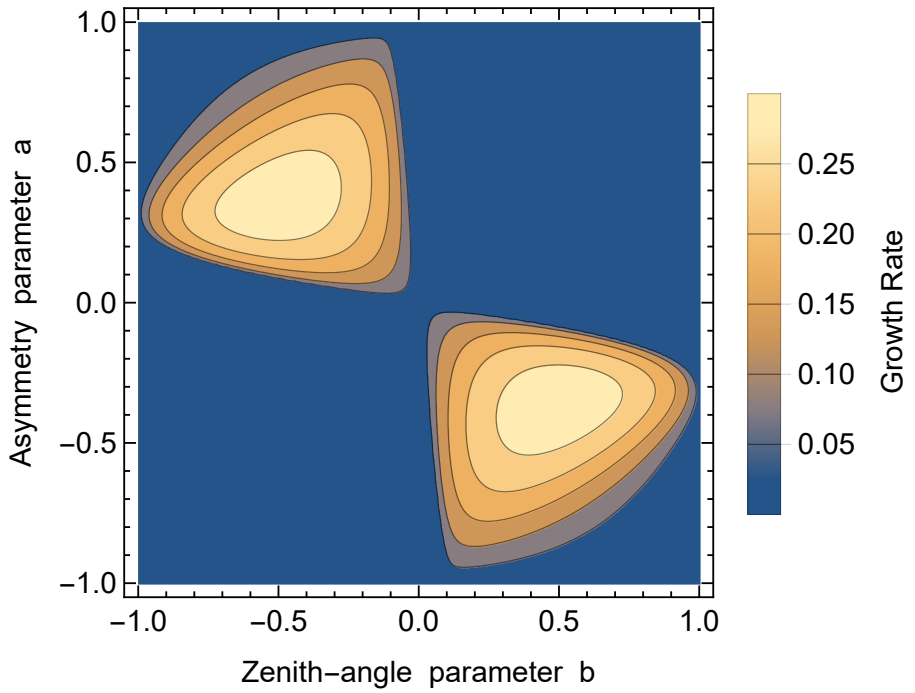

Figure 7.2: Growth rate for the axially breaking solutions in units of μ for the matter-free toy model [2]. The contour plot is displayed with respect to the normalized ν_e and $\bar{\nu}_e$ densities. The angular distributions used are the ones displayed in Figure 7.1. The figure shows no instability for the SN region, i.e., for $a > 0$ and $b > 0$.

extract the physical consequences from the results. The results are displayed in Figure 7.2.

First of all, we must highlight that in our numerical study, the axially symmetric equation shows no instabilities in the region $-1 < a < 1$ and $-1 < b < 1$, so we have not plotted it. The plot shown in Figure 7.1 corresponds to the axially breaking solution. The growth rates of the figure are proportional to μ, and therefore correspond to fast modes. There are only instabilities in the second and fourth quadrants, whereas the first and third quadrant are stable. In other words, whenever a and b have the same sign, the system is stable. Nonetheless, as we have already discussed, only the first quadrant of the parameter space corresponds to the SN-type scenario.

We can conclude that, for the toy model we have used, the triggering of fast flavor conversion requires that the species with the broader angular distribution (regardless of which one it is) must be the one with the smaller flux[1]. Although this is out of the range of the traditional SN parameter space, the LESA effect that we have discussed in Chapter 3 could lead to situations where a or b are negative. Moreover, in the accretion disk arising from compact binary merger

[1]This conclusion seems to be in contradiction with the results of Reference [67]. Up to date, there is no clear explanation behind this contradiction.

remnants it is possible to have a higher ν_e than $\bar{\nu}_e$ flux, i.e., $a < 0$. Indeed, fast oscillations in the spatial evolution of this type of scenarios have been reported in Reference [68]. We will discuss more about these objects in Section 7.2.3.

Fast Oscillations

Assuming different angular distributions for the different neutrino species has a huge impact on the results of the linearized stability analysis. As we have already mentioned, the growth rate of the flavor instabilities is not proportional to the vacuum oscillation frequency ϖ but instead is proportional to the neutrino number density μ. In other words, the system undergoes fast flavor conversion. Under these circumstances, ϖ loses its central role. Although we already founded this phenomenon when we studied the neutrino colliding beam model, this is the first time where flavor conversion without flavor oscillation appears in a SN-type scenario.

7.1.3 Solutions including the matter effect

We have already seen in the previous chapter how matter effects can change the results drastically. Therefore, as a next step we will include matter effects in our toy model. However, as we are about to discuss, the way the matter effect inhibit the instabilities is qualitative different in this case.

The key element is that, for this specific system, the matter effect is not only proportional to the matter density λ but instead it is proportional to the ratio of λ to the neutrino density μ, which is encoded in the parameter $m = \lambda/\mu$. We have adopted $m = 1$ for the results plotted in Figure 7.3. The top panel corresponds to the axially symmetric solution, whereas the bottom corresponds to the axially breaking solution. The bottom panel corresponds to the axially breaking solution. We observe that the instability regions are very similar to the previous matter-free case. Again, the range of values for a physical SN scenario shows no instabilities. However, the axially breaking solution will now provide imaginary solutions for Ω. Moreover, this solution shows a completely different shape. In this case, there is fast flavor conversion in the case where ν_e have a broader distribution ($b > 0$) and there are highest flux of ν_e with respect to $\bar{\nu}_e$ ($a > 0$). This quadrant, where the parameters a and b are greater than zero, corresponds to the SN motivated region. In case the matter density is very large ($\lambda \gg \mu$ or $m \gg 1$) or very small $m \ll 1$, the axially symmetric solution disappears, leaving us with the bottom panel of Figure 7.3 alone.

The matter suppression is very different from the one traditionally observed for the bulb model, i.e., the case studied in Chapter 6. In that scenario where the matter potential "shifted" the instabilities to a region of the parameter space far away from the SN matter profile. However, in this case, the fast flavor conversion in the SN motivated region is induced by the matter potential whenever we reach the region $m \sim 1$, and is zero everywhere else. We

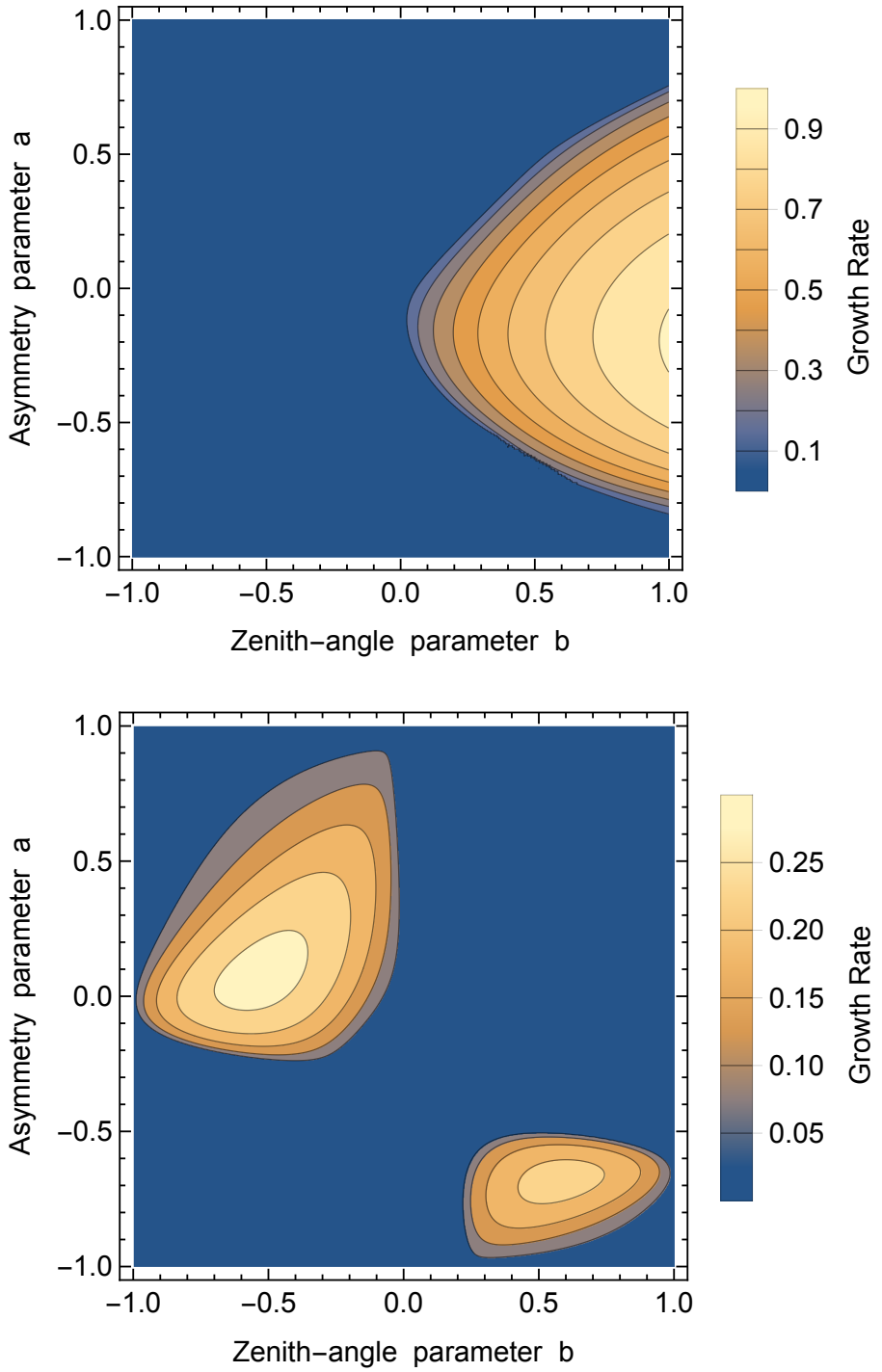

Figure 7.3: Growth rate of the instability in units of μ [2]. These figures correspond to the case $m = 1$. The upper panel is the axially conserving solution, whereas the bottom panel shows the axially breaking one. The parameters a and b are the same ones used in Figure 7.2. Note that the axially conserving solution shows instabilities in the first quadrant, which corresponds to SN motivated region of the parameter space.

can now connect these result with the SN scenario. The large matter potential would inhibit fast oscillations during the accretion phase, in a similar way slow instabilities are suppressed. In any case, we need to be careful with the interpretation of these results. This discussion has been done under the stationarity assumption. In the next section we will indeed drop this assumption and study the consequences.

Previous studies

Besides the works of R. Sawyer [67,69], fast instabilities were never found in the context of SN-type scenarios. This is puzzling because several studies had been conducted for systems where different neutrino species had different angular distributions. Therefore, it is worth going through these previous works in order to understand why this phenomenon remained unnoticed.

First of all, the work performed by Mirizzi and Serpico [58,70] used different forward-peaked distributions for different neutrino species. The key element of this work is that they focused their study on the difference between the angular distributions of ν_e and ν_x, but they assumed equal distributions for $(\nu_e,\bar{\nu}_e)$ and for $(\nu_x,\bar{\nu}_x)$, respectively. In other words, the difference in the fluxes was between the e and x flavors, but ν_e and $\bar{\nu}_e$ had the exact same distributions. This assumption implies, as we have already discussed, that the instabilities are zero as soon we set ϖ to zero. Therefore in these cases fast oscillations could not appear.

On the other hand, Saviano et al. [71,72] conducted stability analyses using realistic energy and zenith angle distributions from numerical SN simulations. In both cases, the growth rates were always of the order of magnitude of ϖ. In these studies, the matter effect λ was almost an order of magnitude than μ, and therefore the fast oscillations cannot appear. Moreover, for the specific models used, the angular distributions were too similar to trigger fast flavor conversion.

To sum up, although many studies were performed using different angular distributions for different species, the particular assumptions were chosen in such a way that the fast flavor conversion never showed up. Therefore, this interesting phenomenon remained inadverted. As we have already mentioned, R. Sawyer was the first one to become aware of fast flavor conversion, but his findings remained overlooked for almost a decade.

7.2 Temporal and spatial SN evolution

Hitherto, the results discussed in the present chapter have been obtained under the stationarity assumption. Nonetheless, our ultimate goal is to discuss the most general scenario, with the minimal amount of assumptions. Therefore, the next step consists of considering a more generic case, where we drop out the stationarity assumption. The generality of the DR formalism developed in

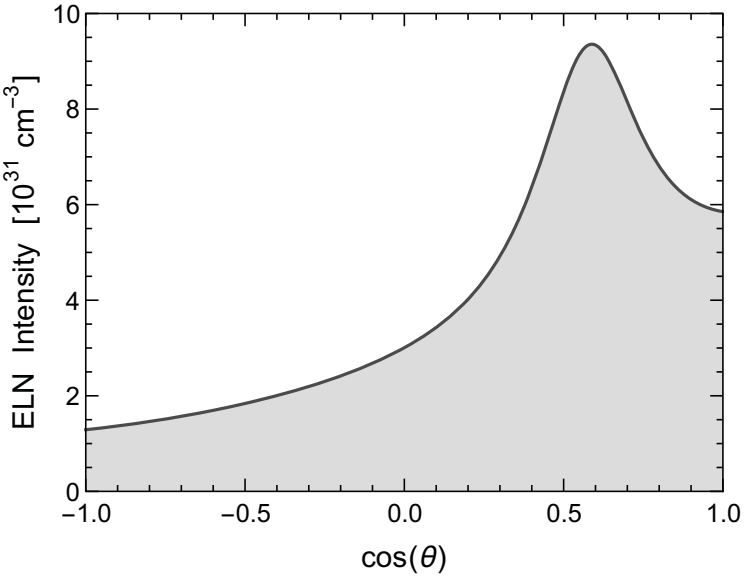

Figure 7.4: ELN angle distribution from a 1D, 15 $M_\odot$ progenitor SN simulation. The figure shows the ELN values at a distance of 37 km from the star's center at 280 ms after the shock bounce [4]

Chapter 5 shows now its full capability. Using the machinery already derived, including the time variation turns out to be a straightforward task. The eigenvalue equations are the same ones given by Equation 7.1.1 and Equation 7.1.2, i.e., the same ones we have used for the two-bulb model. However, the integral equations are the ones we have derived in Equation 5.5.7 of Chapter 5. We adapt them to this particular setup, arriving at

$$I_n = \int_{-\infty}^{+\infty} dv g_v \frac{v^n}{w+q}, \tag{7.2.1}$$

where $w = (k_z - \phi)/\mu$ and $q = (\omega - \lambda - \epsilon)/\mu$. Now that we have the most generic equations, we will proceed to apply them to a concrete example, and explore the consequences in terms of the flavor stability analysis. The way to proceed is already familiar to us, since we have performed this in a large number of cases already.

7.2.1 Realistic 1D core-collapse SN angular distribution

In order to study the neutrino time and spatial evolution in a SN-type scenario, we will use the angular emission information of a SN simulation to solve the EOM. Unfortunately, up to date, there are no flavor-dependent neutrino angle distributions from SN simulations available. Nevertheless, in order to gain intuition, we have extracted the ELN distributions from a 1D simulation of the Garching group of a 15 $M_\odot$ progenitor [66, 73, 74]. The results are plotted in Figure 7.4.

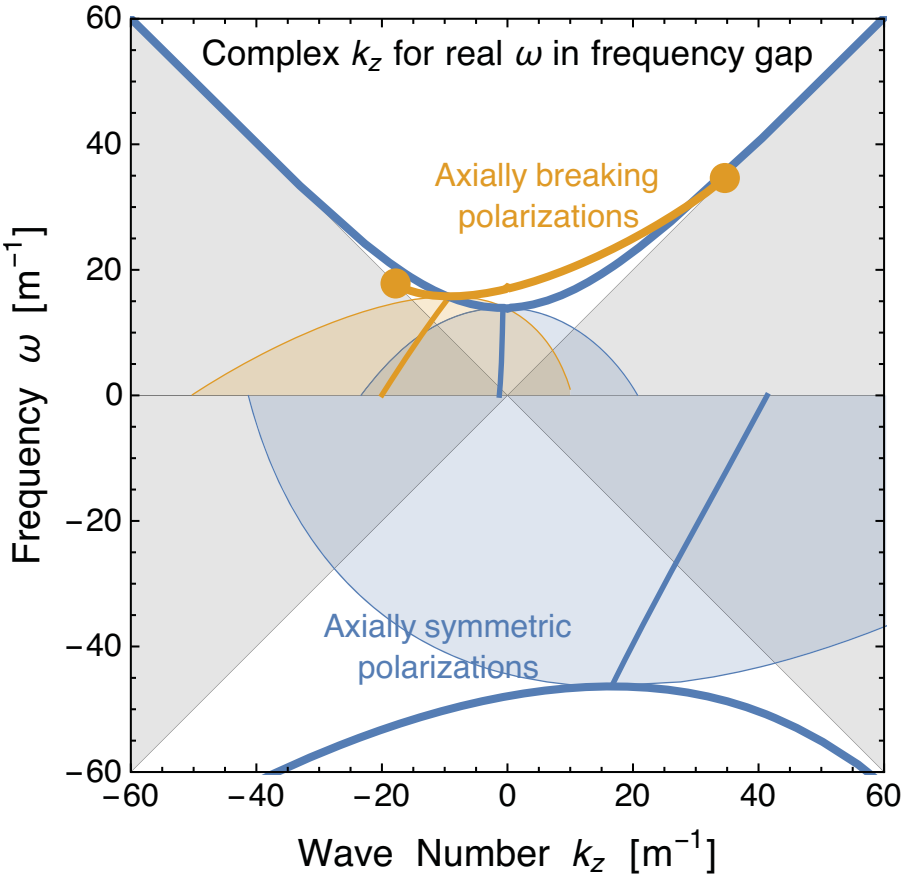

Figure 7.5: Dispersion relation for an ELN given in Figure 7.4 in the massless limit [4]. The gray regions are the zone of avoidance for real (ω, k_z). The blue thick lines correspond to the axially symmetric polarization, whereas the yellow thick lines are the two degenerate solutions of the axially breaking polarization. The yellow points are the end points of the branch. The edge yellow and blue shadowed regions represents the modulus of $\mathrm{Im}(k_z)$ for the axially symmetric and axially breaking solutions, respectively. Furthermore, the semi-thick lines represent the $\mathrm{Re}(k_z)$ in each case.

This figure shows a typical case not far from the decoupling region, at a distance of 37 km the the star's center. For larger distances, the ELN profile is horizontally compressed near the forward direction ($\cos\theta = 1$), although backward modes ($\cos\theta < 1$) are never empty. One key feature is the forward dip due to the $\bar{\nu}_e$ distribution being more forward peaked than ν_e. We have also analyzed the same figure for different times. More precisely for 150, 280, and 500 ms after core-bounce. However, we have not found any place or time in this model where this dip would go negative

We now plug in the angular distribution provided by Figure 7.4 in the integrals given by Equation 7.2.1 and we study the DP properties of this particular setup. What comes out is displayed in Figure 7.5. There is a lot of informa-

tion in this figure, so we will now analyze it carefully. We start with the gray, shadowed region. This corresponds to the region of the parameter space where there are no propagating solutions for the flavor waves. In other words, in this region the DP is only fulfilled if k_z and ω are simultaneously imaginary. The blue thick lines are the axially symmetric solutions, i.e., the solutions obtained when solving the eigenvalue equation given by Equation 7.1.1. The thick, orange line corresponds to the two degenerate axially breaking solutions obtained from Equation 7.1.2. It must be highlighted that the solutions are not continuous parabolas as in the case of the axially breaking solution but instead the branches have end points, which are displayed by the thick orange points. In the zone of avoidance, that is, in the region or frequency gap between the solutions, the wave vector k_z that satisfies the DP is complex. We display the imaginary part of k_z for the axially symmetric and axially breaking solutions with the shadowed blue and orange regions, respectively. Furthermore, the semi-thick lines represent the real part of k_z. This DR corresponds to the top-right panel of the Figure 5.5 studied in Chapter 5.

Therefore, for G_v provided by the numerical 1D SN numerical simulation, the DR obtained presents a frequency gap. In other words, for an initial value of the frequency chosen in this gap, the system will undergo a spatial run away. On the other hand, the system is always stable on its temporal evolution. The DR obtained is similar to the DR of an electromagnetic wave in a plasma: for every k_z there is a real value for the frequency ω that satisfies the DR. However, there is a region or gap for ω for which the DR requires k_z to be complex. The DR shown in Figure 7.5 is analogous to the DR of an electromagnetic (EM) wave in a plasma: for every k_z there is real ω, but there is a region or gap for ω for where the DR demands a complex $\mathbf{k}$. However, we must be careful when we use this analogy. When an EM wave enters a forbidden region, the plasma frequency inhibits propagation and therefore the wave gets reflected. For flavor waves, entering a forbidden region produces exponential spatial growth the and therefore leads to flavor decoherence. If we analyze the EOM of EM waves, it corresponds to second-order differential equation, whereas flavor waves obey a first-order one. This could be the reason behind this different behavior.

7.2.2 Neutrino angular distributions for different progenitor masses

The DR obtained in the previous section has only a gap for the frequency, but no gap for the wave number. Nonetheless, this study of the DR for the 1D numerical simulation is based on the data of only one SN numerical simulation. Therefore, it could be argued that the absence of a crossing in the ELN spectrum is a characteristic of this particular set of data, but for other simulations this condition no longer holds. In order to investigate this possibility, a recent study, contained in Reference [75], has analyzed a set of angular emission distributions from 1D SN simulations using different progenitor masses. More

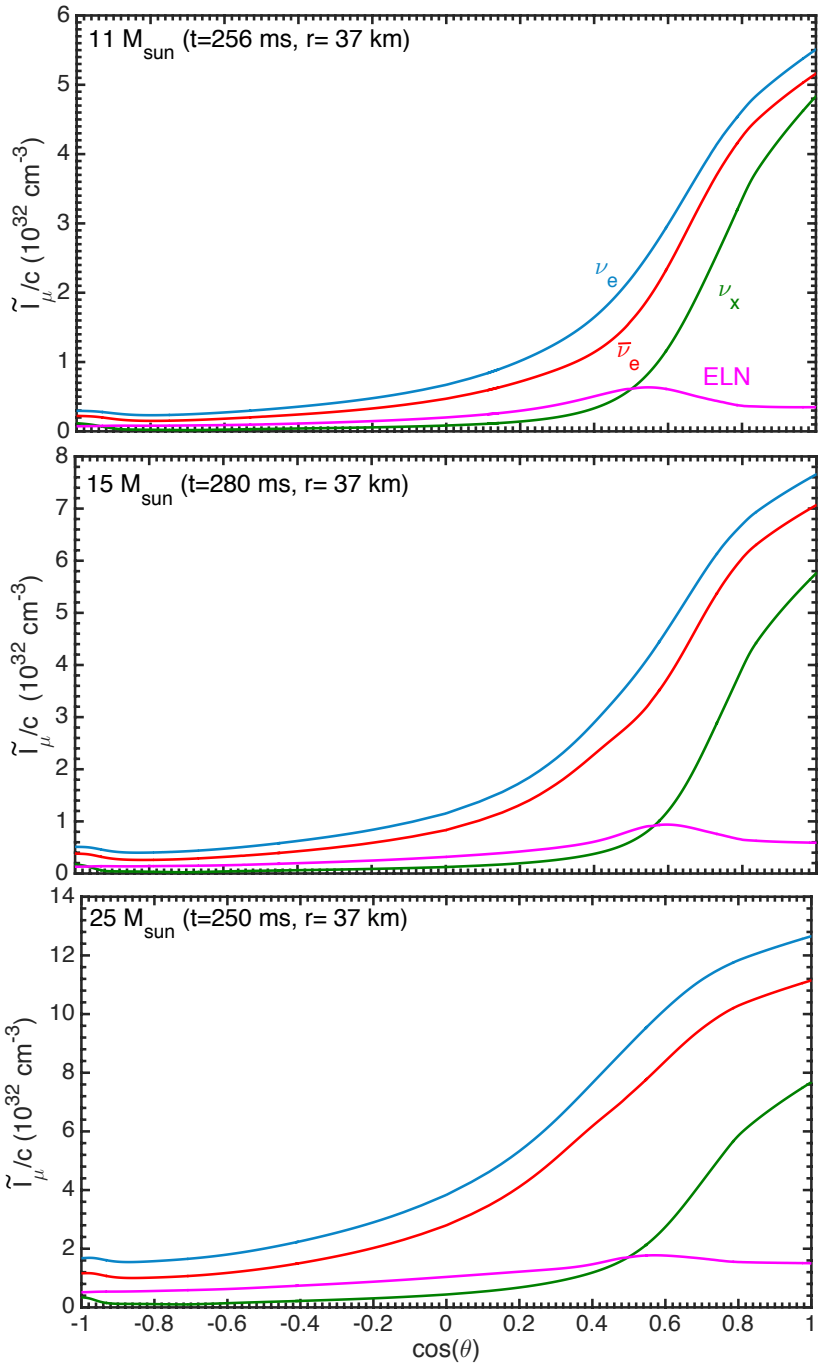

Figure 7.6: Neutrino number intensity as a function of $\cos\theta$ at a distance of 37 km from the star's center [75]. The blue line stands for ν_e, the red line for $\bar{\nu}_e$, and the green line for ν_x. The magenta line shows the ELN carried by electron neutrinos, i.e., $\nu_e - \bar{\nu}_e$. On each panel's top is displayed the time of the snapshot and the mass of the progenitor.

precisely, this work focuses on progenitor masses of 11.2, 15 and 25 $M_\odot$.

In the models analyzed, the ELN has several different spectral features. However, in any of the analyzed cases there is a crossing in the neutrino ELN spectrum. In the light of this study, it seems that for the 1D models, there are no possible instabilities in the temporal evolution of the neutrino field.

However, we have to be very cautious with these conclusions. All these models are obtained assuming spherical symmetry. It is still uncertain what happens in the 3D SN numerical models. Up to date, there are no ray-by-ray analyses for these simulations. Due to the LESA effect, it seems plausible that for certain directions the G_v goes to negative values. In such cases, the system would exhibit wave number gaps, i.e., the system would be unstable in the temporal evolution. Moreover, it is also uncertain what happens in case the instability occurs only locally, and how this will affect the evolution of the neutrino field as a whole.

7.2.3 Compact binary merger remnants

The DR formalism can be applied to other astrophysical objects with high neutrino density. There is a particular astrophysical environment that can be very interesting from the point of view of neutrino self-induced flavor conversion. This corresponds to the binary system formed by one neutron star (NS) with another NS or a black hole (BH). Analogously to the interior of core-collapse SNe, the accretion disk of these objects are density rich environments, which has motivated a large number of neutrino self-induced flavor conversion studies [76–80]. On the other hand, neutrino flavor evolution plays an important role in the evolution of these objects. For instance, neutrinos can have an impact in the nucleosynthesis which occurs in the accretion disk [81, 82].

Similarly to the case of core-collapse SN, the decoupling region of $\bar{\nu}_e$ resides inside of the one corresponding to ν_e. The difference is that, due to the protonization taking place in the system, the $\bar{\nu}_e$ flux is higher than the ν_e flux [81, 83].

Reference [68] contains recent a study has derived the ELN of an example for these environments and applied the DR formalism to it. In this case, the ELN distribution has a "crossing", meaning that it starts from a negative value and evolves to a positive one as a function of the radius. This implies that the system is generically unstable when studying its temporal evolution [68]. Moreover, the authors of Reference [68] have reported instabilities under certain conditions in the spatial evolution, which is in consonance with the results discussed in Section 7.1. Nonetheless, the spatial instabilities does not seem to be as generic as the temporal ones.

7.3 Summary

In the course of this chapter, we have used the EOM developed in Chapter 5 adapted to the bulb geometry. The first example analyzed corresponded to

a stationary system with a homogeneous perpendicular direction ($k_x = 0$). The system was studied under the assumption in the massless neutrinos, i.e., $\varpi = \Delta m^2/(2E) = 0$. Moreover, we have used the "two bulb" emission model, where ν_e and $\bar{\nu}_e$ have different angular emission distribution. In other words, we assume that neutrinos are carrying non-zero ELN out of the star.

We have started the analysis without considering matter effects. In this case, only the axially breaking solution provides instabilities. These instabilities are proportional to the neutrino-neutrino interaction strength μ, i.e., they correspond to fast flavor conversion. Without the multi-angle matter effect, the instabilities appear in regions of the parameter space that are not compatible with the traditionally SN motivated parameters. In the next step of our analysis, we have multi-angle matter effects in our system. The particularity of this system is that the matter effects enter the equations as $m = \lambda/\mu$. In other words, it is the ratio between the matter potential and the neutrino-neutrino interaction energy that drives matter effects. For values of $m \sim 1$, the axially symmetric solution gives solutions with imaginary eigenvalues for ω. In other words, it also provides unstable solutions. Furthermore, this solution for range compatible with a SN scenario. However, in case the matter potential is very large ($m \gg 1$) or very small $m \ll 1$ compared to μ, this solutions disappears. The bottom line of this analysis is that assuming different neutrino spheres for the different neutrino species can trigger fast flavor oscillations.

We have also commented briefly on all the previous works that have used different angular emission functions for different neutrino species. Our conclusion is that, with the exception of the works performed by R. Sawyer, all studies were performed under assumptions that inhibited the appearance of fast flavor conversion.

For the next example, we have again analyzed the EOM using the bulb geometry, but for this time we have dropped the stationarity, and we have studied the full DR. In order to explore the evolution of the spatial and temporal evolution of the neutrino field in a realistic SN scenario, we have used the angle distribution of the ELN angle distribution extracted from a 1D SN numerical simulation. This angle distribution has no crossings, which means that the DR obtained shows a gap in the frequency, but not in the wave vector. Therefore, the system is stable on its time evolution.

In order to investigate if these conclusions were an exclusive feature of the dataset used or a generic feature of the 1D SN numerical models, we have briefly discussed the results of a recent work which explores several 1D simulations with different progenitor masses. The results of this study show that the non-crossing feature seems to be a constant in this type of simulations.

We have also discussed the limitations of our results. First of all, it is still uncertain what happens in the 3D simulations. Furthermore, the LESA effect seems to point in the directions that at least in some directions this crossing can indeed take place. These conclusions are however merely speculative until a deeper analysis is performed. Finally, we must remark that for the study of

the DR of SN-type scenarios, we face the same problem as we did with the two neutrino beam toy model: the DR does not provide the answer on how the system behaves and once again we have to face the boundary conditions of the system.

Finally, we have briefly studied the neutrino emission characteristics of a very interesting subset of astrophysical objects, which are compact binary-merger remnants. These objects show a crossing in the ELN spectrum. This crucial feature translates to a generic instability in the spatial evolution prescribed by the DR. However, the actual condition for the development of such instabilities goes beyond the DR description.

Chapter 8

Conclusions

The study of the dynamics of neutrinos in the presence of self-interactions continues to reveal new effects. Moreover, some of the progress in this field consist of revisiting some aspects that were thought to be understood, but were only the result of the symmetries assumed.

In Chapter 4 we have discussed the mathematical framework to study neutrino interactions in dense media. Moreover, we have arrived at the multi-dimensional partial differential equations which describe collective oscillations. However, as we have pointed out, current computers are unable to directly solve these multi-dimensional partial differential equations. Therefore, we will have to rely on our physical intuition to find the right simplifications to deepen our understanding of these self-refraction dominated systems. At the same time we have to make sure that the assumptions are physically motivated.

As in all other natural sciences, experimental data is the ultimate judge to determine the validity for the theoretical models. At the present time, there is a large number of detectors that are capable of detecting the neutrino signature of a SN. In the future, the deployment of large water, scintillator and argon detectors might allow us to collect individual neutrino events from the Local Group of galaxies. Nonetheless, with current detectors, there is a probability slightly above 3 % of an SN event per year. Moreover, the only signal that has been recorded up to this day corresponds to SN 1987A. Unfortunately, the statistics are rather poor so we can only infer information from the range of energies of the measured neutrinos and of the duration of the signal.

Despite the lack of experimental data, much theoretical work has been done to try to understand and predict the neutrino signal that these experiments some day will detect. The basic theoretical framework was developed more than two decades ago. However, the impossibility of solving the equations neither analytically nor numerically has encouraged the adoption of simplifications to solve the equations. Simplifications can be very useful to understand the dynamics of the neutrino field, but they must be taken with caution: too simplistic system can produce artificial results and lead to incorrect conclusions. The field of self-induced neutrino oscillations has overcome on the course

of its relatively short life a handful of radical turns, changing our understanding of the field in a dramatic way. One illustrating example is the spontaneous symmetry breaking, where the solutions of the equations need not inherit the symmetries of initial conditions.

The main goal persuaded in this thesis was precisely to develop a general framework, where many of the previously assumed simplification are dropped. To this end, we have used the linearized EOM and assumed a general plane wave ansatz with both temporal and spatial dependencies. This has led us to a relation of the frequency with the wave number of the flavor modes, or, in other words, a dispersion relation (DR).

We have applied this formalism to the two colliding beam example. As a first step, we have focused on the temporal evolution of the system, assuming that the system is stable in its spatial evolution. One of the most striking results is the appearance of fast flavor conversion. For this type of instabilities, the growth rates are proportional to the neutrino-neutrino interaction energy μ instead of the vacuum oscillation frequency ϖ. Because in dense environments $\mu \gg \varpi$, these conversions are referred to as "fast". Fast flavor conversion occur even in the limit of massless neutrinos $\varpi = \Delta m^2/2E = 0$, which means that they do not depend on the energy, but only on the angular distributions. Because they do not require neutrino masses or mixing, they correspond to flavor conversion without flavor mixing, where the only role of M^2 is for providing seed disturbances.

We have then dropped spatial stability and assumed a more general DR. In other words, we have studied the temporal and spatial evolution of the two neutrino colliding beam model. After solving the system, we have realized that there can be gaps or "forbidden" regions for the frequency or the wave number. This implies that, if the initial conditions impose a frequency in the gap, the system will undergo spatial exponential growth. Analogously, if the initial conditions impose a wave number in the gap, the system will undergo a temporal run away. If there is a gap for the frequency and the wave number, and the initial conditions impose both an imaginary frequency and wave number, there are no propagating solutions. Finally, the absence of gaps in the DR means that the system is stable.

Once we have understood the behavior of the DR in the colliding neutrino beam model, we have turned our attention to the SN motivated environments. Under the bulb geometry, we have studied the spatial evolution of the system, but considering inhomogeneities in the perpendicular direction. The first thing to highlight is that the growth rate is proportional to ϖ, i.e., it corresponds to "slow" flavor conversion. The result of this study is that small scales shift the instabilities to regions of the parameter space which are far away from the the typical SN matter profile. In other words, the most interesting is the homogeneous scenario, so that inhomogeneous can be safely neglected.

We have further investigated the stationary SN-type scenario. We have assumed that each neutrino species has a different neutrino sphere, i.e., different

angular distribution. This has led to the appearance of fast flavor conversions in a SN scenario for the first time. Moreover, we have concluded that fast flavor conversion in the spatial evolution is only triggered by an asymmetry in the angular distributions, i.e., by considering different angular distributions for the different neutrino species.

We have then applied the DR formalism to study the temporal and spatial evolution of a SN scenario. For this purpose, we have used the angular distribution of a 1D SN numerical simulation to the EOM, and we have performed a general stability analysis. From the results follows that a gap in the frequency but not in the wave number seems to be a generic feature for SN environments. The reason behind is the absence of "crossings" in the angular distribution. Moreover, we have also discussed the angular emission of different numerical simulations, where the absence of crossings seems to be a constant for 1D numerical models.

We have stressed that the DR only can tell us the solutions that are compatible with the EOM, but not which one indeed occurs. This later requires dealing with the boundary conditions. Furthermore, we have studied that under certain circumstances, the DR shows ω gaps. In such a case, the spatial boundary conditions and their time variation are needed to understand the generic behavior of the flavor field. It is also possible that the collision term has to be included in the EOM to see which modes of the flavor field are actually excited, which would go beyond the forward-scattering description used in this work.

Moreover, during the study of the DR, we concluded that the existence of backward modes produces very interesting effects in the DR. The idea of having such modes in a SN-type scenario introduces further difficulties. The existence of a backward flux implies the necessity of defining different boundary conditions in different spatial regions of the SN. Moreover, the inward moving neutrino flux comes from NC scattering from the outward moving ones. This implies a flavor correlation between the inward and outward flow of neutrinos in a SN, which goes beyond the prescription of the present EOM.

8.1 Outlook

Despite all the interesting results and insights for the field contained in this thesis, the critical spirit present in every scientist obliges us to point out the limitations of this work and discuss the future prospects.

This whole work is based in the linearized stability analysis approach. In other words, we make the assumptions that locally, the neutrinos modes do not couple to the other modes. However, there is the possibility that, when studying the full EOM, effects enhanced by the non-linearities appear. Moreover, there is work required from the SN numerical simulation point of view. First of all, it is still uncertain what happens in 3D simulations. In 3D models, the LESA effect suggests that at least in some directions, crossings in angular

distributions can take place.

As has been already mentioned, the DR approach has brought up the necessity of dealing with the boundary conditions. This is an unavoidable requirement if we want to understand neutrino flavor conversion inside a SN. For the time being, we must leave this question unanswered, hoping that in the near future this issues will be further investigated.

After all, we have been awaiting the next galactic SN for the last thirty years, and it would be very useful to have a consolidated theoretical framework of neutrino self-induced collective oscillations before this happens.

Appendix A

Polarization Vectors

As we discussed in Chapter 4, the two flavor scheme is quite appropriate to describe self-induced neutrino oscillations because simplifies the equations significantly but still retains the essential physics of the problem. One collateral benefit of the two flavor scheme is that we can directly translate the 2×2 Hermitian matrices ρ and $\bar{\rho}$ into Euclidean, three dimensional vectors, which are much more intuitive. Although this principle also works for the three flavor scheme, the resulting vectors have eight components and therefore the pictorial properties are lost.

As explained in chapter 4, we can decompose the density matrix as

$$\rho = \frac{f_{\nu_e} + f_{\nu_x}}{2}\mathbb{1} + \frac{f_{\nu_e} - f_{\nu_x}}{2} \begin{pmatrix} s & S \\ S^* & -s \end{pmatrix}. \tag{A.0.1}$$

Now, for the reasons discussed above, we express the density matrix as

$$\rho = (1 + \mathbf{P} \cdot \boldsymbol{\sigma}), \tag{A.0.2}$$

where $\mathbf{P}$ is a three-dimensional unit vector called polarization vector, and σ are the Pauli matrices. We use boldface letters such as $\mathbf{P}$ for vectors in flavor space. The Pauli matrices are traceless, and therefore the trace of the density matrix is not contained in the polarization vector. The $\mathbf{P}$ pointing in the z direction denotes that the neutrino beam has a maximal electron flavor. If $\mathbf{P}$ points down, we have maximal μ flavor, and intermediate positions denote mixed states. To illustrate the advantage of the polarization vector description, we write down the EOM for the density matrix in vacuum

$$\frac{\partial \mathbf{P}}{\partial x} = \varpi \mathbf{B} \times \mathbf{P}, \tag{A.0.3}$$

where the components of the mass basis $\mathbf{B}$ are defined as

$$\mathbf{B} = (\sin 2\theta_{12}, 0, \cos 2\theta_{12}) \tag{A.0.4}$$

and ϖ is the usual vacuum oscillation frequency. The misalignment of the mass basis with respect to the flavor space is contained in the vacuum mixing

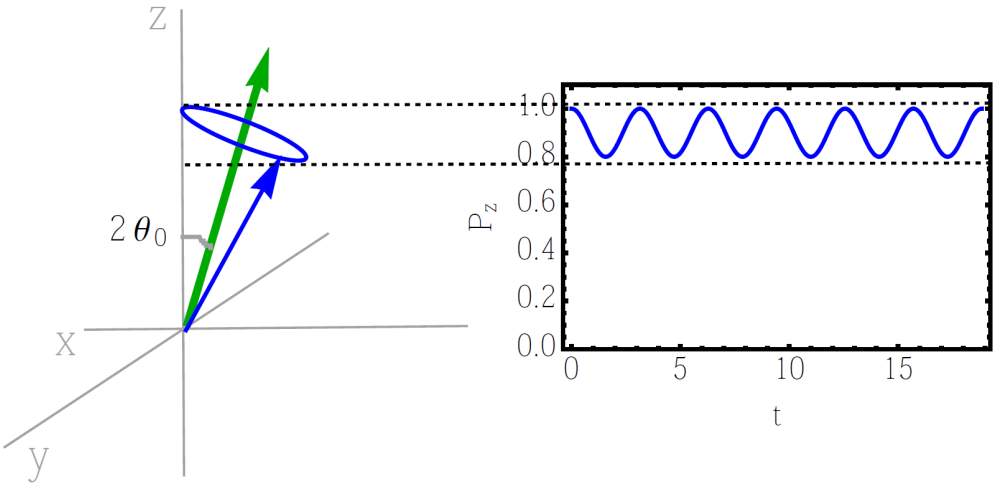

Figure A.1: Graphic representation of neutrino vacuum oscillations for the two flavor ensemble using polarization vectors [84].

angle θ_{12}. With this newly introduced language, it seems now clear that Equation A.0.3 describes the precession of the polarization vector around the vector **B** at a frequency given by the vacuum oscillation frequency. This behaviour is shown in Figure A.1.

The MSW effect can also be understood like a spin precession in the presence of an external magnetic field. In both cases, the polarization vectors provide a very intuitive visualization of these processes and reduce the dynamics of the system to the mechanics of classical spins. For these reasons, polarization vectors have been used in a large number of works for discussing neutrino self-induced flavor conversions.

Appendix B

Analytical functions

In the course of Chapter 6 we will encounter, when solving eigenvalue equations, various integrals that can be solved easily with Wolfram's MATHEMATICA. There can be issues about the validity of the analytic expressions in the complex plane, so we here give the integrals explicitly. These results can also be found in Reference [1].

B.1 Analytical expression for the 1D scenario

In the 1D case, for $k \neq 0$ and in the absence of matter effects ($\bar{\lambda} = 0$), we face integrals of the form

$$f_n(w) = \int_{-1}^{+1} dv \, \frac{v^n}{v + w} \,, \tag{B.1.1}$$

where w is a complex number. Before moving on, we define two auxiliary functions as

$$L(w) = \log\left(\frac{w+1}{w-1}\right) , \tag{B.1.2a}$$

$$A(w) = 2 + w\left[i\,\pi \text{ sign Im}(w) - 2\,\text{arctanh}(w)\right] . \tag{B.1.2b}$$

Using these functions, the solutions for the the ingegrals given by B.1.1 are given by

$$f_0(w) = L(w) \,, \tag{B.1.3a}$$

$$f_1(w) = A(w) \,, \tag{B.1.3b}$$

$$f_2(w) = -2w + w^2 L(w) \,, \tag{B.1.3c}$$

$$f_3(w) = \tfrac{2}{3} + w^2 A(w) \,, \tag{B.1.3d}$$

$$f_4(w) = -\tfrac{2}{3}\left(w + 3w^3\right) + w^4 L(w) \,. \tag{B.1.3e}$$

The actual argument will be of the form $w = (\varpi - \Omega)/k$.

For non-vanishing matter effects ($\bar{\lambda} \neq 0$) and a non-homogeneous perpendicular direction $k \neq 0$ we encounter integrals of the form

$$g_n(p,w) = \int_{-1}^{+1} dv \, \frac{v^n}{v^2 + p\,v + w}\,, \tag{B.1.4}$$

where w is a complex number and p is real. As in the previous case, we define two auxiliary functions

$$\begin{aligned}
K_{q,w} &= \frac{1}{2}\log\left(\frac{w+1+p}{w+1-p}\right)\,, && \text{(B.1.5a)}\\
B_{q,w} &= \frac{1}{\sqrt{4w-p^2}}\left[\arctan\left(A^-\right) + \arctan\left(A^+\right)\right]\,, && \text{(B.1.5b)}\\
C_{q,w} &= p^4 - 4p^2w + 2w^2\,, && \text{(B.1.5c)}
\end{aligned}$$

where $A^{\pm}\frac{2\pm p}{\sqrt{4w-p^2}}$. The solutions to Equation B.1.4 are found to be

$$\begin{aligned}
g_0(p,w) &= 2\,B_{q,w}\,, && \text{(B.1.6a)}\\
g_1(p,w) &= -p\,B_{q,w} + K_{q,w}\,, && \text{(B.1.6b)}\\
g_2(p,w) &= 2 + \left(p^2 - 2w\right)B_{q,w} - p\,K_{q,w}\,, && \text{(B.1.6c)}\\
g_3(p,w) &= -2p - p\left(p^2 - 3w\right)B_{q,w} + \left(p^2 - w\right)K_{q,w}\,, && \text{(B.1.6d)}\\
g_4(p,w) &= \tfrac{2}{3}\left(1 + 3p^2 - 3w\right) + C_{q,w}B_{q,w} - \left(p^3 - 2pw\right)K_{q,w}\,. && \text{(B.1.6e)}
\end{aligned}$$

The actual arguments are going to be $p = 2k/\bar{\lambda}$ and $w = 2(\varpi - \Omega)/\bar{\lambda}$.

B.2 Analytical expression for the 2D scenario

In the 2D case to solve Equation 6.5.14 we need the solve integrals of the form

$$K_n^a = \int_{-\pi}^{+\pi} \frac{d\varphi}{2\pi} \int_0^1 dv \, \frac{v^n\, f_a(\varphi)}{v^2/2 + q\,v\,c_\varphi + w}\,, \tag{B.2.1}$$

where $f_1(\varphi) = 1$, $f_{\rm c}(\varphi) = \cos\varphi$, $f_{\rm cc}(\varphi) = \cos^2\varphi$, and $f_{\rm ss}(\varphi) = \sin^2\varphi$. These integrals can be found analytically with the help of MATHEMATICA. We first define the following auxiliary functions

$$\begin{aligned}
A_{q,w} &= \arctan\left(\frac{q^2 - w}{\sqrt{-w^2}}\right) + \arctan\left(\frac{1 - 2q^2 + 2w}{\sqrt{4q^2 - (1+2w)^2}}\right)\,, && \text{(B.2.2a)}\\
B_{q,w} &= 2\sqrt{-w^2} - \sqrt{4q^2 - (1+2w)^2}\,, && \text{(B.2.2b)}\\
C_{q,w} &= 6q^2 + 2w + 1\,, && \text{(B.2.2c)}\\
D_{q,w} &= 4q^2\left(3q^2 - 2w\right) && \text{(B.2.2d)}\\
E_{q,w} &= 4\left(3q^4 - 6q^2w + 2w^2\right)\,. && \text{(B.2.2e)}
\end{aligned}$$

Our desired integrals are then found to be

$$K_1^1 = A_{q,w}\, S_w\,, \tag{B.2.3a}$$

$$K_3^1 = \left[B_{q,w} + 2\left(q^2 - w\right) A_{q,w}\right]\, S_w\,, \tag{B.2.3b}$$

$$K_5^1 = \left[-2\sqrt{-w^2} + C_{q,w}B_{q,w} + E_{q,w}A_{q,w}\right] \frac{S_w}{2}\,, \tag{B.2.3c}$$

$$K_2^{\mathrm{c}} = \frac{1 - \left(B_{q,w} + 2q^2 A_{q,w}\right) S_w}{2q}\,, \tag{B.2.3d}$$

$$K_4^{\mathrm{c}} = \frac{1 + \left[2\sqrt{-w^2} - C_{q,w}B_{q,w} - D_{q,w}A_{q,w}\right] S_w}{4q}\,, \tag{B.2.3e}$$

$$K_3^{\mathrm{cc}} = \frac{-1 - 4w - \left[2\sqrt{-w^2} - C_{q,w}B_{q,w} - D_{q,w}A_{q,w}\right] S_w}{8q^2}\,, \tag{B.2.3f}$$

where $S_w = -i\,\mathrm{sign}(\mathrm{Im}\, w)$.

Appendix C

Asymptotic solutions

In this appendix we provide analytic asymptotic solutions used in Chapter 6. These results can also be found in Reference [1].

C.1 Asymptotic behavior for the 1D case

We can derive asymptotic solutions for the 1D case with matter, i.e., the large-$\bar{\lambda}$ continuation of the contour plot of Figure 6.4. We begin with the bimodal and MZA instability for $\bar{\lambda} > 0$ and consider the eigenvalue Equation 6.4.13. It is of the form $1 + C_1\mu + C_2\mu^2 = 0$, where the coefficients C_1 and C_2 depend on α, ϖ_0, Ω and $\bar{\lambda}$. We have evaluated the integrals according to the explicit transcendental functions given in Equation B.1.6. We assume that both the real and imaginary parts of the solutions Ω remain of order ϖ_0 and do not become large as $\bar{\lambda} \to \infty$, an assumption that later bears out to be consistent with the solutions. Therefore, we may expand C_1 and C_2 in powers of $\bar{\lambda}^{-1}$ and find that the dominant terms are $C_1 \propto \bar{\lambda}^{-1}$ and $C_2 \propto \bar{\lambda}^{-3/2}$. For convenience, we introduce dimensionless interaction strength $\hat{\mu}$ of order unity, so that we can write

$$\mu = \frac{\hat{\mu}}{1-\alpha}\,(6/\pi)^{1/2}\,(2\varpi_0)^{1/4}\,\bar{\lambda}^{3/4}\,, \tag{C.1.1}$$

where the exact coefficient was chosen for later convenience. The lowest-order term in $C_2\mu^2$ no longer depends on $\bar{\lambda}$, whereas the lowest-order term in $C_1\mu \propto \bar{\lambda}^{-1/4}$ and slowly becomes small as $\bar{\lambda} \to \infty$. To lowest order in $\bar{\lambda}^{-1}$, the eigenvalue equation is found to be

$$\sqrt{\frac{\varpi_0}{\varpi_0 - \Omega}} - \alpha\sqrt{\frac{\varpi_0}{-\varpi_0 - \Omega}} = \frac{1-\alpha}{\hat{\mu}^2}\,. \tag{C.1.2}$$

The asymptotic solution derives from the term quadratic in μ and thus is invariant under $\mu \to -\mu$, i.e., it applies to both mass orderings. We show the asymptotic solution as a blue curve in Figure C.1 on a linear and logarithmic scale. We also show the growth rates for $\bar{\lambda} = 10^2$, 10^4 and 10^6 where the

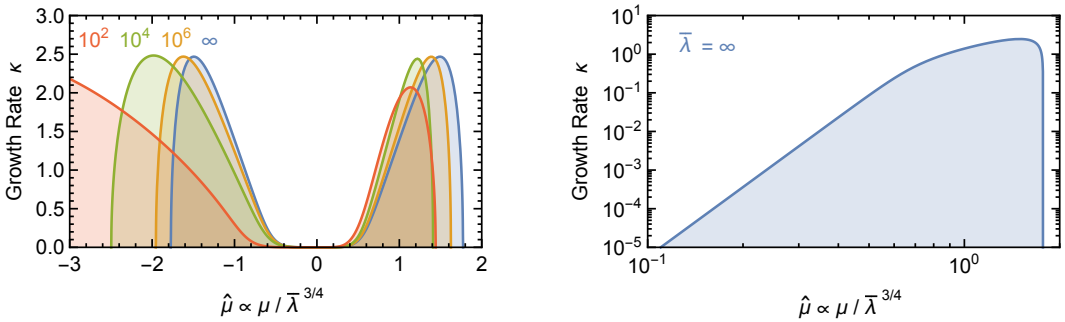

Figure C.1: Growth rate κ of the bimodal and MAA instabilities for $\alpha = 1/2$. The blue curves show the asymptotic behavior for $\bar{\lambda} \to \infty$, whereas the other curves are for the indicated $\bar{\lambda}$ values.

solution is not symmetric under $\mu \to -\mu$ because the linear term in μ kicks in. We have already noted that one needs very large $\bar{\lambda}$ values to obtain the asymptotic solution because the second-largest term only scales with $\bar{\lambda}^{-1/4}$ relative to the dominant term. The asymptotic behavior is achieved for much smaller $\bar{\lambda}$ values if $\mu > 0$. The growth rate vanishes completely above a certain $|\mu|$ value, but obtains nonzero values otherwise, i.e., there is no lower $\hat{\mu}$ threshold. However, for $\hat{\mu} \lesssim 0.5$, the growth rate is a steep power-law of $\hat{\mu}$ and can be taken to be effectively zero.

For our usual example $\alpha = 1/2$ we find that the maximum growth rate occurs for $\hat{\mu} = 1.494$. Therefore, we find that

$$\mu = \pm 4.911\, \varpi_0^{1/4}\, \bar{\lambda}^{3/4} \tag{C.1.3}$$

gives us the locus of the maximum growth rate in the μ-$\bar{\lambda}$ plane for the bimodal and MAA solutions. The maximum value of $\hat{\mu}$ before the growth rate becomes zero is 1.7724. On the small-$\hat{\mu}$ side, the growth rate drops below $\kappa < 1/100$, our usual criterion, at $\hat{\mu} = 0.3478$. Therefore, the footprint of the instability is the region between the lines $\mu = 1.143\, \lambda^{3/4}$ and $5.826\, \lambda^{3/4}$, where both μ and λ are given in units of the vacuum oscillation frequency ϖ_0. This footprint is shown in the first quadrant (upper right) of Figure C.3. The corresponding footprint in the second quadrant (upper left) is also shown.

We next turn to the MZA solution which exists only in inverted ordering ($\mu < 0$) and we consider Equation 6.4.13. If we use $\mu = -\bar{\lambda}/[2(1-\alpha)]$ the leading terms cancel, leaving us with a leading term of order $\bar{\lambda}^{-1/2}$. To obtain the lowest-order equation, we introduce another dimensionless parameter $\hat{\mu}$ and write

$$\mu = \frac{-\bar{\lambda}}{2\,(1-\alpha)} - \hat{\mu}\, \frac{\pi\sqrt{1-\alpha^2}}{2\,(1-\alpha)^2}\, \sqrt{\varpi_0 \bar{\lambda}}\,, \tag{C.1.4}$$

where, of course, the detailed coefficients in the second term are chosen for later convenience. One then finds a quadratic equation with solutions

$$\frac{\Omega}{\varpi_0} = \frac{1+\alpha^2-2\hat{\mu}^2\,(1+\alpha^2)}{1-\alpha^2} \pm i\, \frac{4\alpha}{1-\alpha^2}\, \sqrt{\hat{\mu}^2(1-\hat{\mu}^2)}\,. \tag{C.1.5}$$

Notice that these solutions require $0 \leq \hat{\mu} \leq 1$ and we have always assumed $0 \leq \alpha \leq 1$. The imaginary part, as a function of $\hat{\mu}^2$, has the familiar semi-circular shape. In Figure C.2 we show it as a function of $\hat{\mu}$ (blue curve) and we also show the full solution for $\bar{\lambda} = 10^3$ and 10^2. The asymptotic solution is quite good for relatively small $\bar{\lambda}$ values. In contrast to the other solutions, on a logarithmic scale the unstable range becomes very narrow as $\bar{\lambda} \to \infty$.

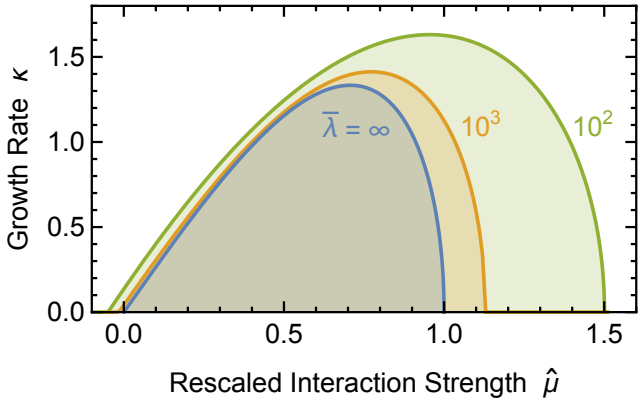

Figure C.2: Asymptotic growth rate κ for the MZA instability for $\alpha = 1/2$. The interaction strength is scaled according to Equation C.1.4. The blue curve shows the asymptotic behavior for $\bar{\lambda} \to \infty$ according to Equation C.1.5, whereas the other curves correspond to the labeled $\bar{\lambda}$ values.

The maximum growth rate obtains for $\hat{\mu} = 1/\sqrt{2}$. Therefore, for our usual example $\alpha = 1/2$ we find that for the MZA solution,

$$\mu = -\bar{\lambda} - \pi\sqrt{3\varpi_0\bar{\lambda}/2} \tag{C.1.6}$$

gives us the locus of the maximum growth rate in the μ-$\bar{\lambda}$ plane. The growth rate becomes exactly zero for $\hat{\mu} \leq 0$ and $\hat{\mu} \geq 1$, so the footprint (see upper-left quadrant in Figure C.2) is delimited by the curves $\mu = -\bar{\lambda}$ and $\mu = -\bar{\lambda} - \pi\sqrt{3\bar{\lambda}\varpi_0}$. The width of the footprint scales with $\sqrt{\bar{\lambda}}$, i.e., on a logarithmic scale it becomes very narrow for large $\bar{\lambda}$.

For $\bar{\lambda} < 0$, the above approach does not lead to unstable solutions. Numerically we observe that for $\bar{\lambda} \to -\infty$, the real part of the solutions approaches $\mathrm{Re}(\Omega) \to \bar{\lambda}/2$, i.e., a large negative number. Therefore, to be able to expand the equation, we express $\Omega = \bar{\lambda}/2 + w\,\varpi_0$ and seek self-consistent solutions with the dimensionless eigenvalue w of order unity. After expansion for $\bar{\lambda} \to -\infty$, the asymptotic eigenvalue equations are

$$\frac{\log(1-w) - \alpha\log(-1-w)}{1-\alpha} = a \tag{C.1.7}$$

where

$$a = \log\left(-\frac{2\bar{\lambda}}{e^2\varpi_0}\right) - \frac{1}{\hat{\mu}} \qquad \text{or} \qquad a = \log\left(-\frac{2\bar{\lambda}}{e^2\varpi_0}\right) + \frac{3+\hat{\mu}^2}{(3-\hat{\mu})\hat{\mu}}\,, \tag{C.1.8}$$

where e is Euler's number and as always the logarithm is with base e.

For our usual example $\alpha = 1/2$, we can solve this equation analytically with the explicit result

$$w_{\alpha=1/2} = \frac{2 - e^a \pm i\sqrt{e^a(8 - e^a)}}{2}\,. \tag{C.1.9}$$

It has a nonzero imaginary part for $-\infty < a < \log(8) = 2.0794$, although it becomes exponentially small for $a \ll -1$. The maximum imaginary part obtains for $a = \log(4) = 1.3863$ and the maximum is 2. Therefore, the maximum growth rate obtains for

$$A = \frac{1}{\hat{\mu}} \qquad \text{or} \qquad A = -\frac{3 + \hat{\mu}^2}{(3 - \hat{\mu})\hat{\mu}}\,, \tag{C.1.10}$$

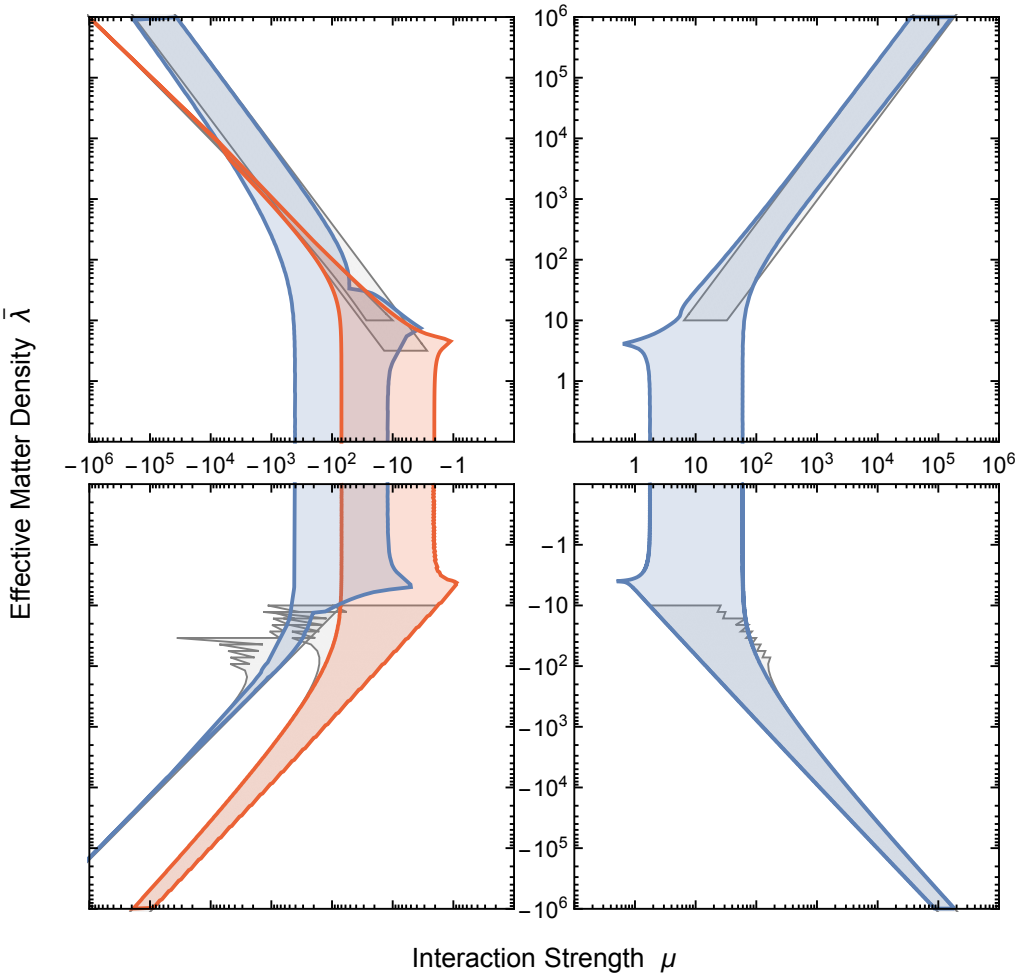

Figure C.3: Footprint of the 1D instabilities in the μ-$\bar{\lambda}$ plane for $k = 0$ (homogeneous mode) and $\alpha = 1/2$. The colored regions derive from a numerical solution, where the blue footprints correspond to Equation 6.4.13, the red solutions to the 1×1 block given by Equation 6.4.12. The grey regions show the asymptotic solutions in the large-$\bar{\lambda}$ limit derived in this appendix.

where

$$A = -\log(4) - 2 + \log\left(-\frac{2\bar{\lambda}}{\varpi_0}\right) = \log\left(\frac{-\bar{\lambda}}{2e^2\varpi_0}\right). \tag{C.1.11}$$

Therefore, we have altogether three solutions, corresponding to the three instabilities, with maximum growth rates on the locus in the μ-$\bar{\lambda}$ plane given by

$$\mu = -2\bar{\lambda}\,\frac{6}{3A + \sqrt{3(A+2)(3A-2)}} \to -2\bar{\lambda}\,\frac{1}{A}, \tag{C.1.12a}$$

$$\mu = +2\bar{\lambda}\,\frac{1}{A}, \tag{C.1.12b}$$

$$\mu = +2\bar{\lambda}\,\frac{3A + \sqrt{3(A+2)(3A-2)}}{2\,(A-1)} \to 6\bar{\lambda}, \tag{C.1.12c}$$

where the limiting behavior is understood for $A \to \infty$. Because $\bar{\lambda} \to -\infty$, the first solution corresponds to positive μ and thus to the bimodal solution, the second and third solutions are the MAA and MZA instabilities, respectively.

To draw the footprints in the lower quadrants of Figure C.3, we notice that $\kappa = 0$ for $a > \log(8)$ and on the other side $\kappa < 1/100$ for $a < \log(4 - \sqrt{39999}/50) = -9.90348$. Therefore, the asymptotic footprints are limited by

$$a_1 = \log(8) \quad \text{and} \quad a_2 = \log(4 - \sqrt{39999}/50) \tag{C.1.13}$$

from which the limiting curves are extracted by solving Equation C.1.8 for $\hat{\mu}$. Once more we note that two of the footprints are "wide" and nearly symmetric between $\mu \to -\mu$, whereas the third instability has a very narrow footprint.

C.2 Asymptotic behavior for the 2D case

C.2.1 Asymptotic solutions for 2D with $\bar{\lambda} = 0$ and $k \to \infty$

We are looking for the large-k solutions of the 2D case without matter ($\bar{\lambda} = 0$). We need to find the zeroes of the determinant of the matrix in Equation 6.5.13. We first look at the 3×3 block and calculate it according to the explicit integrals that we have found. Next we substitute the variables as $\varpi = 1$, $\alpha = 1/2$, $\Omega = -k + x$, and

$$\mu = a\,(k + m\sqrt{k}), \tag{C.2.1}$$

where a is a coefficient to be determined and overall the substitution for μ is an educated guess. Except for the choice $\alpha = 1/2$, everything is still completely general. The unknown frequency to be found is x. Its imaginary part is the growth rate which we are looking for. The parameter m is an effective interaction strength because it gives us μ in this parameterised form.

Next we expand the determinant as a power series for large k and find to lowest nontrivial order

$$\det(3\times 3 \text{ block}) = \frac{2880 - 480\,a - 424\,a^2 - 11\,a^3}{2880}$$
$$-\frac{3\,i}{320}\left[\sqrt{2}a^2(32+a)\left(2\sqrt{x-1}-\sqrt{x+1}\right)\right]\frac{1}{\sqrt{k}} + \mathcal{O}(1/k)\,. \qquad \text{(C.2.2)}$$

For the term proportional to $1/\sqrt{k}$ to dominate we demand the first term to vanish, giving us three possible values for a from the requirement $2880 - 480\,a - 424\,a^2 - 11\,a^3 = 0$. The explicit results are quite complicated expressions. Numerically one finds

$$a_1 = -37.1825\,, \qquad \text{(C.2.3)}$$
$$a_2 = -3.42115\,, \qquad \text{(C.2.4)}$$
$$a_3 = +2.05821\,. \qquad \text{(C.2.5)}$$

In other words, we have three asymptotic solutions, where one is for positive μ and two for negative μ as expected.

If we now imagine that a is one of these solutions, the first term in the determinant vanishes and in the second term we can substitute $a^3 = (2880 - 480\,a - 424\,a^2)/11$ to remove the a^3 term. In anticipation of the result we further introduce the quantity

$$m_{\max} = \frac{162\sqrt{3}\,[120 - a\,(20+3a)]}{11\,[1080 - a\,(120+53a)]}\,, \qquad \text{(C.2.6)}$$

which for our three possible a values are numerically

$$m_{\max,1} = 1.23675\,, \qquad \text{(C.2.7)}$$
$$m_{\max,2} = 4.49396\,, \qquad \text{(C.2.8)}$$
$$m_{\max,3} = 2.77208\,. \qquad \text{(C.2.9)}$$

Then we are left with the equivalent of the determinant equation

$$\sqrt{6}\,m = i\,m_{\max}\left(2\sqrt{x-1}-\sqrt{x+1}\right)\,. \qquad \text{(C.2.10)}$$

It has the explicit solutions

$$x = \frac{5}{3} - \frac{10\,m^2}{3m_{\max}^2} \pm \frac{8\sqrt{m^2(m^2-m_{\max}^2)}}{3m_{\max}^2}\,. \qquad \text{(C.2.11)}$$

The solution has an imaginary part for $0 < m < m_{\max}$. Therefore, the large-k footprint of the three instabilities is limited by the lines

$$\mu = a_i\,k \quad \text{and} \quad \mu = a_i\left(k + m_{\max,i}\sqrt{k}\right)\,. \qquad \text{(C.2.12)}$$

For μ-values between these lines, the system is unstable.

Finally we turn to the 1×1 block in Equation 6.5.13. We proceed with the same substitutions except for

$$\mu = a\,(k+b)\,, \tag{C.2.13}$$

where for the moment we leave open what b is supposed to mean. Expanding the 1×1 block determinant in powers of large k, we here find

$$\begin{aligned}\det(1{\times}1 \text{ block}) &= \frac{6+a}{6} + \frac{a}{6}\,(-9+b+3x)\,\frac{1}{k} \\ +i\,\frac{2\sqrt{2}\,a}{3}\,&\left[2(x-1)^{3/2} - (x+1)^{3/2}\right]\frac{1}{k^{3/2}} + \mathcal{O}(1/k^2)\,.\end{aligned} \tag{C.2.14}$$

Again we can get rid of the first term, this time by setting $a = -6$, i.e., the footprint of this instability is for negative μ. The remaining equation is

$$\begin{aligned}\det(1{\times}1 \text{ block}) &= (9-b-3x)\,\frac{1}{k} \\ -i\,4\sqrt{2}\,&\left[2(x-1)^{3/2} - (x+1)^{3/2}\right]\frac{1}{k^{3/2}} + \mathcal{O}(1/k^2)\,.\end{aligned} \tag{C.2.15}$$

The leading term does not provide an imaginary solution. In other words, for very large k we do not have an instability. If we keep both the leading and next to leading term, we finally need to solve the equation

$$(9-b-3x)\,\sqrt{k} = i\,4\sqrt{2}\,\left[2(x-1)^{3/2} - (x+1)^{3/2}\right]\,. \tag{C.2.16}$$

Solving this equation actually leads to an asymptotic solution where the growth rate exists for a range of b-values. However, the maximum growth rate decreases with $1/\sqrt{k}$. Therefore, we have overall four instabilities, but for $k \to \infty$ the one from the single block disappears.

C.2.2 Asymptotic solutions for 2D with $k = 0$ and $\bar{\lambda} \to \infty$

We can derive asymptotic solutions for the 2D case with matter, i.e., the large-$\bar{\lambda}$ solutions of the eigenvalue Equation 6.5.15, corresponding to Equation 6.5.16 and Equation 6.5.17. We begin with the 2×2 block and $\bar{\lambda} \to +\infty$. As in the 1D case, we assume that Ω remains of order ϖ_0, an assumption which is confirmed by the results. We express the interaction strength in terms of a dimensionless parameter $\hat{\mu}$ in the form

$$\mu = \frac{\hat{\mu}}{1-\alpha}\,\bar{\lambda}\,. \tag{C.2.17}$$

To lowest order in $\bar{\lambda}^{-1}$ the eigenvalue equation is, using $w = \Omega/\varpi_0$,

$$\frac{\log(1-w) - \alpha\log(-1-w)}{1-\alpha} = a\,, \quad \text{where} \quad a = \log\left(\frac{\bar{\lambda}}{2\varpi_0}\right) - \frac{2(\hat{\mu}-1)^2}{\hat{\mu}^2}\,. \tag{C.2.18}$$

This result is identical with Equation C.1.7, but with a different expression for a. To draw the asymptotic footprints we simply need to solve for $\hat{\mu}$ using the limiting a-values given in Equation C.1.13. The result is shown in Figure C.4 as grey shaded regions in the upper panels, to be compared with the blue regions which derive from a numerical solution of the full eigenvalue equations.

For the 1×1 block in the limit $\bar{\lambda} \to +\infty$, we express the interaction strength in the form

$$\mu = -\frac{\bar{\lambda} + \hat{\mu}\varpi_0 \log(\bar{\lambda}/2\varpi_0)}{1-\alpha}\,. \tag{C.2.19}$$

With $\hat{\mu} = 0$ the eigenvalue equation is identically fulfilled to lowest order in $\bar{\lambda}^{-1}$, i.e., to lowest order unstable solutions require $\mu = -\lambda/(1-\alpha)$. This simple behavior indeed corresponds to the very "thin" footprint shown in red in the upper left panel of Figure C.4. Including $\hat{\mu} \neq 0$ leads to an approximate eigenvalue equation which is not very simple and does not lead to simple asymptotic solutions.

For the next cases we turn to the limit $\bar{\lambda} \to -\infty$. In this limit, we write $\Omega = \bar{\lambda}/2 + w\,\varpi_0$ in analogy to the 1D case. In the $\bar{\lambda} \to -\infty$ limit, the eigenvalue is characterized by w values of order unity. We also write the interaction strength again in the form of Equation C.2.17. The limiting eigenvalue equation is the same as in Equation C.2.18, but now with

$$a = \log\left(-\frac{\bar{\lambda}}{2\varpi_0}\right) - \frac{2(\hat{\mu}-1)^2}{(\hat{\mu}-4)\,\hat{\mu}} \qquad \text{or} \qquad a = \log\left(-\frac{\bar{\lambda}}{2\varpi_0}\right) - \frac{\hat{\mu}+1}{\hat{\mu}}\,, \tag{C.2.20}$$

where the first expression applies to the 2×2 block, the second to the 1×1 block of the eigenvalue matrix. As before, to draw the asymptotic footprints we solve for $\hat{\mu}$ using the limiting a-values given in Equation C.1.13. The result is shown in Figure C.4 as grey shaded regions in the lower panels, to be compared with the blue and red regions which derive from a numerical solution of the full equations.

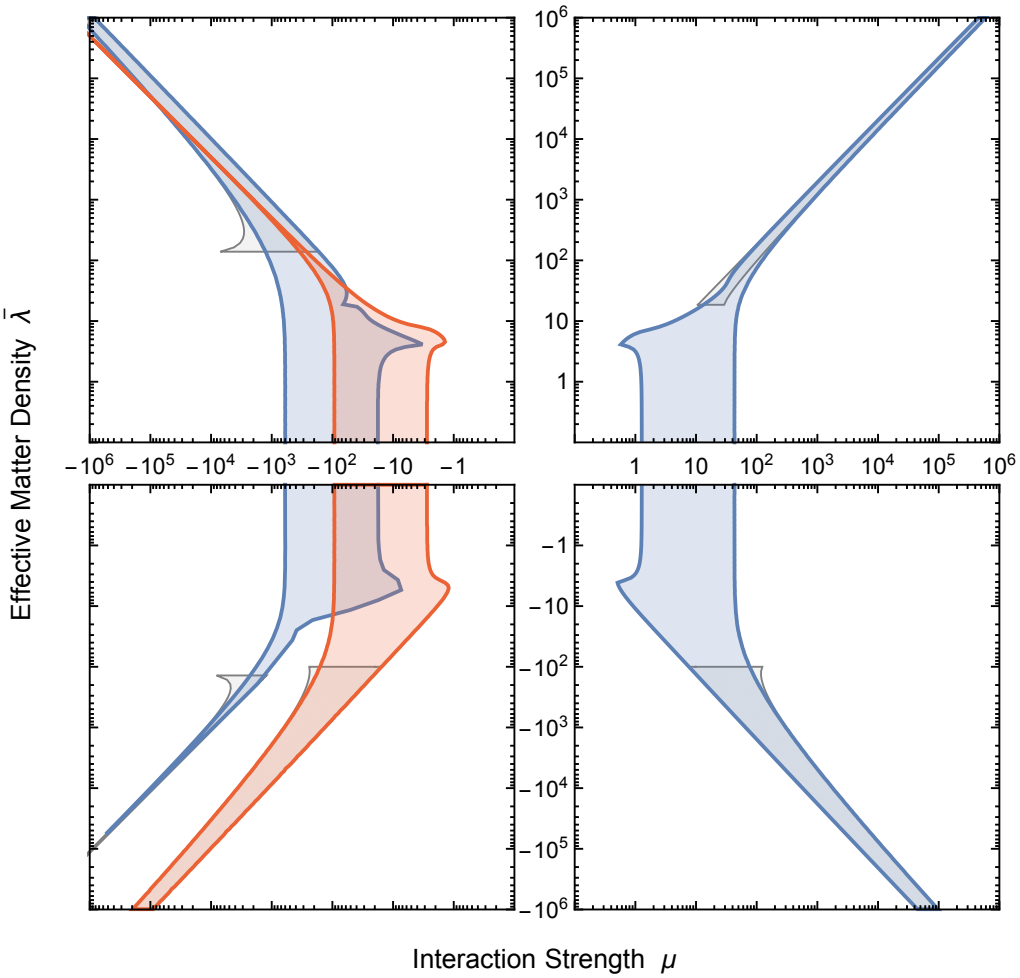

Figure C.4: Footprint of the 2D instabilities in the μ-$\bar{\lambda}$ plane for $k = 0$ (homogeneous mode) and $\alpha = 1/2$. The colored regions derive from the numerical solution, where the blue footprints correspond to the 2×2 block in Equation 6.5.16, the red solutions to Equation 6.5.17. The grey regions show the asymptotic solutions in the large-$\bar{\lambda}$ limit derived in this appendix.

Appendix D

Supernovae footprint diagram

SN environments are the best suited laboratories for the study of neutrino self-induced oscillations. In this thesis, we have introduced the concept of flavor instability, and discussed that, under certain circumstances, the collective flavor modes undergo exponential flavor conversion, i.e., unstable behavior which can lead to flavor decoherence. In order to study if these circumstances are reached in a stationary SN environment we use the so-called footprint diagrams.

Footprint diagrams show a snapshot of a SN matter profile for a given time as function of the radius. In order to explain how to interpret the results provided by these diagrams, we have included Figure D.1, obtained from Reference [65]. For this particular example, the SN matter profile corresponds to a SN numerical simulation of a 15 $M_\odot$ progenitor at 150 ms after shock bounce. The sudden drop in the SN profile corresponds to the shock front. Of course, the exact shape of the spectrum depends on the mass of the progenitor and is also time dependent, with the shock wave being further away from the core at later times. The x axis shows the neutrino-neutrino interaction strength defined in Chapter 6, $\mu = \sqrt{2} G_{\rm F} n_\nu (R/r)^2$, where R is the radius of the neutrino sphere. The y axis displays the matter density defined as $\lambda = \sqrt{2} G_{\rm F} n_e (R/r)^2$.

After performing the stability analysis, there are certain regions of the λ-μ parameter space where the equations are unstable. For this example shown in Figure D.1, the blue region corresponds to the bimodal instability for inverted ordering (IO), and the red region corresponds to the Bimodal instability for the normal ordering (NO). The crucial point is that, if the region of instability does not intersect the SN matter profile, we can conclude that the system is stable. On the other hand, if the matter profile crosses an instability region, the system is prone to undergo exponential flavor conversion. In the example of Figure D.1, the blue curve does not intersect the SN matter profile. We can therefore assess that this instability is harmless for the SN under study. On the other hand, the blue region, corresponding to the normal ordering, intersects the matter profile of the SN short after the shock front. Therefore, with this specific SN matter profile, this instability can be triggered .

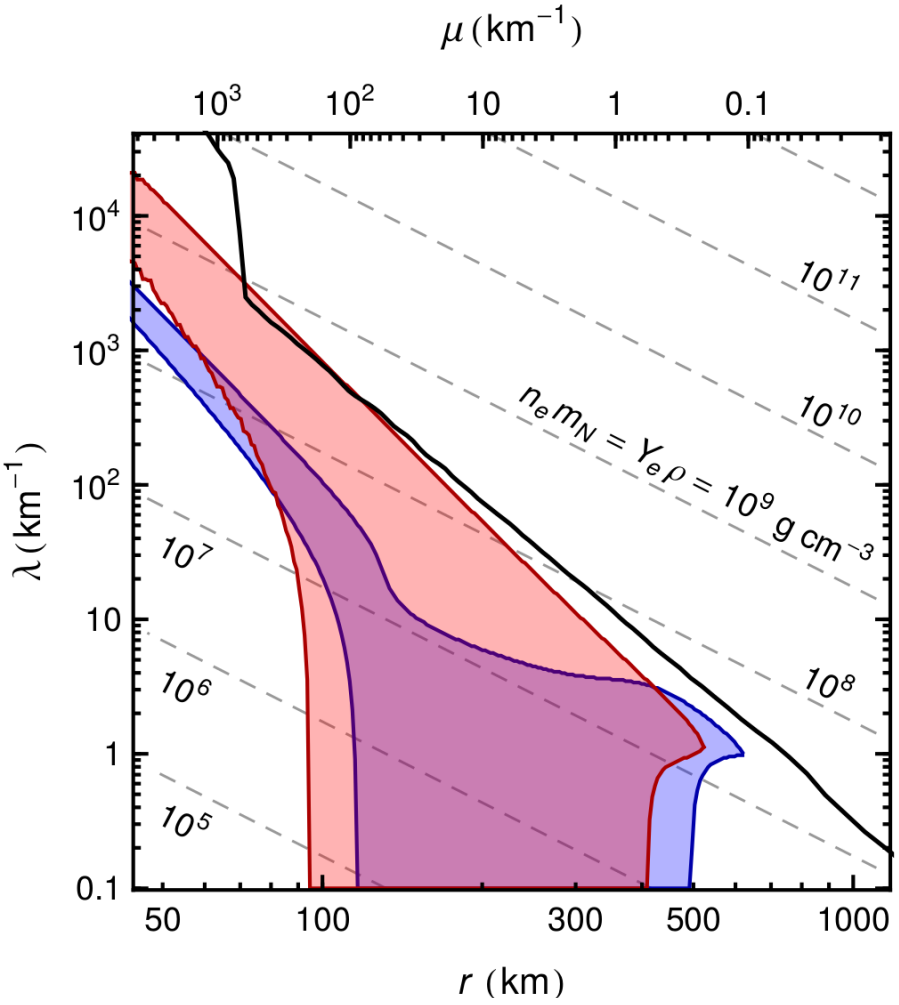

Figure D.1: Regions of exponentially growing solutions corresponding to the IO (blue) and NO (red) scenarios, depending on radius r and the multi-angle matter potential [65]. Thick black line: SN density profile.

Bibliography

[1] S. Chakraborty, R. S. Hansen, I. Izaguirre and G. Raffelt, *Self-induced flavor conversion of supernova neutrinos on small scales*, *JCAP* **1601** (2016) 028 [1507.07569].

[2] S. Chakraborty, R. S. Hansen, I. Izaguirre and G. Raffelt, *Self-induced neutrino flavor conversion without flavor mixing*, *JCAP* **1603** (2016) 042 [1602.00698].

[3] S. Chakraborty, R. Hansen, I. Izaguirre and G. Raffelt, *Collective neutrino flavor conversion: Recent developments*, *Nucl. Phys.* **B908** (2016) 366–381 [1602.02766].

[4] I. Izaguirre, G. Raffelt and I. Tamborra, *Fast Pairwise Conversion of Supernova Neutrinos: A Dispersion-Relation Approach*, *Phys. Rev. Lett.* **118** (2017) 021101 [1610.01612].

[5] B. Garbrecht and I. Izaguirre, *Phenomenology of Baryogenesis from Lepton-Doublet Mixing*, *Nucl. Phys.* **B896** (2015) 412–439 [1411.2834].

[6] S. Chakraborty and I. Izaguirre, *Diffuse neutrinos from extragalactic supernova remnants: Dominating the 100 TeV IceCube flux*, *Phys. Lett.* **B745** (2015) 35–39 [1501.02615].

[7] S. Chakraborty and I. Izaguirre, *Star-forming galaxies as the origin of IceCube neutrinos: Reconciliation with Fermi-LAT gamma rays*, 1607.03361.

[8] C. Patrignani and the Particle Data Group, *Review of particle physics*, *Chinese Physics C* **40** (2016) 100001.

[9] P. W. Higgs, *Broken symmetries and the masses of gauge bosons*, *Phys. Rev. Lett.* **13** (Oct, 1964) 508–509.

[10] S. F. King, *Neutrino mass models*, *Rept. Prog. Phys.* **67** (2004) 107–158 [hep-ph/0310204].

[11] G. Dvali and L. Funcke, *Small neutrino masses from gravitational -term*, *Phys. Rev.* **D93** (2016) 113002 [1602.03191].

[12] Z. Maki, M. Nakagawa and S. Sakata, *Remarks on the unified model of elementary particles*, *Prog. Theor. Phys.* **28** (1962) 870–880.

[13] J. J. Gomez-Cadenas, J. Martin-Albo, M. Mezzetto, F. Monrabal and M. Sorel, *The Search for neutrinoless double beta decay*, *Riv. Nuovo Cim.* **35** (2012) 29–98 [1109.5515].

[14] F. Capozzi, G. L. Fogli, E. Lisi, A. Marrone, D. Montanino and A. Palazzo, *Status of three-neutrino oscillation parameters, circa 2013*, *Phys. Rev.* **D89** (2014) 093018 [1312.2878].

[15] M. C. Gonzalez-Garcia, M. Maltoni and T. Schwetz, *Updated fit to three neutrino mixing: status of leptonic CP violation*, *JHEP* **11** (2014) 052 [1409.5439].

[16] D. V. Forero, M. Tortola and J. W. F. Valle, *Neutrino oscillations refitted*, *Phys. Rev.* **D90** (2014) 093006 [1405.7540].

[17] **Planck** Collaboration, P. A. R. Ade *et. al.*, *Planck 2013 results. XVI. Cosmological parameters*, *Astron. Astrophys.* **571** (2014) A16 [1303.5076].

[18] L. Wolfenstein, *Neutrino Oscillations in Matter*, *Phys. Rev.* **D17** (1978) 2369–2374.

[19] S. P. Mikheev and A. Yu. Smirnov, *Resonance Amplification of Oscillations in Matter and Spectroscopy of Solar Neutrinos*, *Sov. J. Nucl. Phys.* **42** (1985) 913–917. [Yad. Fiz.42,1441(1985)].

[20] N. Cabibbo, *Time Reversal Violation in Neutrino Oscillation*, *Phys. Lett.* **72B** (1978) 333–335.

[21] J. Lesgourgues and S. Pastor, *Massive neutrinos and cosmology*, *Phys. Rept.* **429** (2006) 307–379 [astro-ph/0603494].

[22] **KATRIN** Collaboration, A. Osipowicz *et. al.*, *KATRIN: A Next generation tritium beta decay experiment with sub-eV sensitivity for the electron neutrino mass. Letter of intent*, hep-ex/0109033.

[23] G. Mention, M. Fechner, T. Lasserre, T. A. Müller, D. Lhuillier, M. Cribier and A. Letourneau, *The Reactor Antineutrino Anomaly*, *Phys. Rev.* **D83** (2011) 073006 [1101.2755].

[24] T. A. Müller *et. al.*, *Improved Predictions of Reactor Antineutrino Spectra*, *Phys. Rev.* **C83** (2011) 054615 [1101.2663].

[25] G. G. Raffelt, *Stars as laboratories for fundamental physics*. 1996.

[26] H. T. Janka, *Neutrino Emission from Supernovae*, 1702.08713.

[27] H.-T. Janka, K. Langanke, A. Marek, G. Martinez-Pinedo and B. Müller, *Theory of Core-Collapse Supernovae*, *Phys. Rept.* **442** (2007) 38–74 [astro-ph/0612072].

[28] A. Mirizzi, I. Tamborra, H.-T. Janka, N. Saviano, K. Scholberg, R. Bollig, L. Hudepohl and S. Chakraborty, *Supernova Neutrinos: Production, Oscillations and Detection*, *Riv. Nuovo Cim.* **39** (2016) 1–112 [1508.00785].

[29] B. Dasgupta, A. Dighe, A. Mirizzi and G. G. Raffelt, *Spectral split in prompt supernova neutrino burst: Analytic three-flavor treatment*, *Phys. Rev.* **D77** (2008) 113007 [0801.1660].

[30] I. Tamborra, F. Hanke, H.-T. Janka, B. Müller, G. G. Raffelt and A. Marek, *Self-sustained asymmetry of lepton-number emission: A new phenomenon during the supernova shock-accretion phase in three dimensions*, *Astrophys. J.* **792** (2014) 96 [1402.5418].

[31] F. Hanke, B. Müller, A. Wongwathanarat, A. Marek and H.-T. Janka, *SASI Activity in Three-Dimensional Neutrino-Hydrodynamics Simulations of Supernova Cores*, *Astrophys. J.* **770** (2013) 66 [1303.6269].

[32] H.-T. Janka, L. Scheck, K. Kifonidis, E. Müller and T. Plewa, *Supernova asymmetries and pulsar kicks - Views on controversial issues*, *ASP Conf. Ser.* **332** (2005) 363 [astro-ph/0408439].

[33] J. M. Blondin and A. Mezzacappa, *The spherical accretion shock instability in the linear regime*, *Astrophys. J.* **642** (2006) 401–409 [astro-ph/0507181].

[34] T. Lund, A. Marek, C. Lunardini, H.-T. Janka and G. Raffelt, *Fast time variations of supernova neutrino fluxes and their detectability*, *Phys. Rev.* **D82** (2010) 063007 [1006.1889].

[35] I. Tamborra, F. Hanke, B. Müller, H.-T. Janka and G. Raffelt, *Neutrino signature of supernova hydrodynamical instabilities in three dimensions*, *Phys. Rev. Lett.* **111** (2013) 121104 [1307.7936].

[36] **Kamiokande-II** Collaboration, K. Hirata *et. al.*, *Observation of a Neutrino Burst from the Supernova SN 1987a*, *Phys. Rev. Lett.* **58** (1987) 1490–1493. [,727(1987)].

[37] R. M. Bionta *et. al.*, *Observation of a Neutrino Burst in Coincidence with Supernova SN 1987a in the Large Magellanic Cloud*, *Phys. Rev. Lett.* **58** (1987) 1494.

[38] E. N. Alekseev, L. N. Alekseeva, I. V. Krivosheina and V. I. Volchenko, *Detection of the Neutrino Signal From SN1987A in the LMC Using the Inr Baksan Underground Scintillation Telescope*, *Phys. Lett.* **B205** (1988) 209–214.

[39] S. M. Adams, C. S. Kochanek, J. F. Beacom, M. R. Vagins and K. Z. Stanek, *Observing the Next Galactic Supernova*, *Astrophys. J.* **778** (2013) 164 [1306.0559].

[40] C. W. Walter, *The Super-Kamiokande Experiment*, 0802.1041.

[41] K. Scholberg, *Supernova Neutrino Detection*, *Ann. Rev. Nucl. Part. Sci.* **62** (2012) 81–103 [1205.6003].

[42] G. Sigl and G. Raffelt, *General kinetic description of relativistic mixed neutrinos*, *Nucl. Phys.* **B406** (1993) 423–451.

[43] A. Vlasenko, G. M. Fuller and V. Cirigliano, *Neutrino Quantum Kinetics*, *Phys. Rev.* **D89** (2014) 105004 [1309.2628].

[44] A. Vlasenko, G. M. Fuller and V. Cirigliano, *Prospects for Neutrino-Antineutrino Transformation in Astrophysical Environments*, 1406.6724.

[45] C. Volpe, D. Väänänen and C. Espinoza, *Extended evolution equations for neutrino propagation in astrophysical and cosmological environments*, *Phys. Rev.* **D87** (2013) 113010 [1302.2374].

[46] D. Väänänen and C. Volpe, *Linearizing neutrino evolution equations including neutrino-antineutrino pairing correlations*, *Phys. Rev.* **D88** (2013) 065003 [1306.6372].

[47] J. Serreau and C. Volpe, *Neutrino-antineutrino correlations in dense anisotropic media*, *Phys. Rev.* **D90** (2014) 125040 [1409.3591].

[48] A. Kartavtsev, G. Raffelt and H. Vogel, *Neutrino propagation in media: Flavor-, helicity-, and pair correlations*, *Phys. Rev.* **D91** (2015) 125020 [1504.03230].

[49] A. Banerjee, A. Dighe and G. Raffelt, *Linearized flavor-stability analysis of dense neutrino streams*, *Phys. Rev.* **D84** (2011) 053013 [1107.2308].

[50] F. Capozzi, B. Dasgupta and A. Mirizzi, *Self-induced temporal instability from a neutrino antenna*, *JCAP* **1604** (2016) 043 [1603.03288].

[51] B. Dasgupta, A. Mirizzi and M. Sen, *Fast neutrino flavor conversions near the supernova core with realistic flavor-dependent angular distributions*, 1609.00528.

[52] G. Raffelt and D. d. S. Seixas, *Neutrino flavor pendulum in both mass hierarchies*, *Phys. Rev.* **D88** (2013) 045031 [1307.7625].

[53] G. Mangano, A. Mirizzi and N. Saviano, *Damping the neutrino flavor pendulum by breaking homogeneity*, *Phys. Rev.* **D89** (2014) 073017 [1403.1892].

[54] H. Duan and S. Shalgar, *Flavor instabilities in the neutrino line model*, *Phys. Lett.* **B747** (2015) 139–143 [1412.7097].

[55] A. Mirizzi, G. Mangano and N. Saviano, *Self-induced flavor instabilities of a dense neutrino stream in a two-dimensional model*, *Phys. Rev.* **D92** (2015) 021702 [1503.03485].

[56] E. L. L.P. Pitaevskii, *Course of theoretical physics, Volume 10*. 1981.

[57] G. Fogli, E. Lisi, A. Marrone and I. Tamborra, *Supernova neutrinos and antineutrinos: Ternary luminosity diagram and spectral split patterns*, *JCAP* **0910** (2009) 002 [0907.5115].

[58] A. Mirizzi and P. D. Serpico, *Flavor Stability Analysis of Dense Supernova Neutrinos with Flavor-Dependent Angular Distributions*, *Phys. Rev.* **D86** (2012) 085010 [1208.0157].

[59] J. F. Cherry, J. Carlson, A. Friedland, G. M. Fuller and A. Vlasenko, *Neutrino scattering and flavor transformation in supernovae*, *Phys. Rev. Lett.* **108** (2012) 261104 [1203.1607].

[60] J. F. Cherry, J. Carlson, A. Friedland, G. M. Fuller and A. Vlasenko, *Halo Modification of a Supernova Neutronization Neutrino Burst*, *Phys. Rev.* **D87** (2013) 085037 [1302.1159].

[61] H. Duan, G. M. Fuller, J. Carlson and Y.-Z. Qian, *Simulation of Coherent Non-Linear Neutrino Flavor Transformation in the Supernova Environment. 1. Correlated Neutrino Trajectories*, *Phys. Rev.* **D74** (2006) 105014 [astro-ph/0606616].

[62] S. Hannestad, G. G. Raffelt, G. Sigl and Y. Y. Y. Wong, *Self-induced conversion in dense neutrino gases: Pendulum in flavour space*, *Phys. Rev.* **D74** (2006) 105010 [astro-ph/0608695]. [Erratum: Phys. Rev.D76,029901(2007)].

[63] G. L. Fogli, E. Lisi, A. Marrone and A. Mirizzi, *Collective neutrino flavor transitions in supernovae and the role of trajectory averaging*, *JCAP* **0712** (2007) 010 [0707.1998].

[64] S. Chakraborty, G. Raffelt, H.-T. Janka and B. Müller, *Supernova deleptonization asymmetry: Impact on self-induced flavor conversion*, *Phys. Rev.* **D92** (2015) 105002 [1412.0670].

[65] G. Raffelt, S. Sarikas and D. de Sousa Seixas, *Axial Symmetry Breaking in Self-Induced Flavor Conversionof Supernova Neutrino Fluxes*, *Phys. Rev. Lett.* **111** (2013) 091101 [1305.7140]. [Erratum: Phys. Rev. Lett.113,239903(2014)].

[66] S. Sarikas, I. Tamborra, G. Raffelt, L. Hudepohl and H.-T. Janka, *Supernova neutrino halo and the suppression of self-induced flavor conversion*, *Phys. Rev.* **D85** (2012) 113007 [1204.0971].

[67] R. F. Sawyer, *Neutrino cloud instabilities just above the neutrino sphere of a supernova*, *Phys. Rev. Lett.* **116** (2016) 081101 [1509.03323].

[68] M.-R. Wu and I. Tamborra, *Fast neutrino conversions: Ubiquitous in compact binary merger remnants*, 1701.06580.

[69] R. F. Sawyer, *Speed-up of neutrino transformations in a supernova environment*, *Phys. Rev.* **D72** (2005) 045003 [hep-ph/0503013].

[70] A. Mirizzi and P. D. Serpico, *Instability in the Dense Supernova Neutrino Gas with Flavor-Dependent Angular Distributions*, *Phys. Rev. Lett.* **108** (2012) 231102 [1110.0022].

[71] N. Saviano, S. Chakraborty, T. Fischer and A. Mirizzi, *Stability analysis of collective neutrino oscillations in the supernova accretion phase with realistic energy and angle distributions*, *Phys. Rev.* **D85** (2012) 113002 [1203.1484].

[72] S. Chakraborty, A. Mirizzi, N. Saviano and D. d. S. Seixas, *Suppression of the multi-azimuthal-angle instability in dense neutrino gas during supernova accretion phase*, *Phys. Rev.* **D89** (2014) 093001 [1402.1767].

[73] S. Sarikas, G. G. Raffelt, L. Hudepohl and H.-T. Janka, *Suppression of Self-Induced Flavor Conversion in the Supernova Accretion Phase*, *Phys. Rev. Lett.* **108** (2012) 061101 [1109.3601].

[74] The neutrino data for the 15 $M_\odot$ 1D Garching model are available at http://wwwmpa.mpa-garching.mpg.de/ccsnarchive/index.html.

[75] I. Tamborra, L. Huedepohl, G. Raffelt and H.-T. Janka, *Flavor-dependent neutrino angular distribution in core-collapse supernovae*, 1702.00060.

[76] A. Malkus, J. P. Kneller, G. C. McLaughlin and R. Surman, *Neutrino oscillations above black hole accretion disks: disks with electron-flavor emission*, *Phys. Rev.* **D86** (2012) 085015 [1207.6648].

[77] A. Malkus, A. Friedland and G. C. McLaughlin, *Matter-Neutrino Resonance Above Merging Compact Objects*, 1403.5797.

[78] Y.-L. Zhu, A. Perego and G. C. McLaughlin, *Matter Neutrino Resonance Transitions above a Neutron Star Merger Remnant*, *Phys. Rev.* **D94** (2016) 105006 [1607.04671].

[79] M. Frensel, M.-R. Wu, C. Volpe and A. Perego, *Neutrino Flavor Evolution in Binary Neutron Star Merger Remnants*, *Phys. Rev.* **D95** (2017), no. 2 023011 [1607.05938].

[80] A. Chatelain and C. Volpe, *Helicity coherence in binary neutron star mergers and non-linear feedback*, *Phys. Rev.* **D95** (2017) 043005 [1611.01862].

[81] A. Perego, S. Rosswog, R. M. Cabezón, O. Korobkin, R. Käppeli, A. Arcones and M. Liebendörfer, *Neutrino-driven winds from neutron star merger remnants*, *Mon. Not. Roy. Astron. Soc.* **443** (2014), no. 4 3134–3156 [1405.6730].

[82] B. D. Metzger and R. Fernández, *Red or blue? A potential kilonova imprint of the delay until black hole formation following a neutron star merger*, *Mon. Not. Roy. Astron. Soc.* **441** (2014) 3444–3453 [1402.4803].

[83] M. Ruffert, H. T. Janka, K. Takahashi and G. Schaefer, *Coalescing neutron stars: A Step towards physical models. 2. Neutrino emission, neutron tori, and gamma-ray bursts*, *Astron. Astrophys.* **319** (1997) 122–153 [astro-ph/9606181].

[84] D. d. Sousa Seixas, *Spontaneous symmetry breaking in collective neutrino oscillations*. PhD thesis, Munich U., 2014.

Acknowledgments

The last three years of my life have been a very enjoyable experience. I cannot fully express my gratitude in words towards my supervisor, Georg Raffelt. To begin with, he has given me the opportunity of doing a Ph.D. in particle astrophysics, a field which fascinates me. Moreover, Georg has always been extremely patient; I cannot recall a single time I knocked at his office's door when he did not have time for me. During the course of our numerous meetings, I have learned a lot from him. Not only from his physics knowledge, but also in other aspects of life. Above all things, I was touched by the passion he professes to physics. His influence will remain with me for the rest of my life.

The completion of this work has only been possible thanks to the contributions of other people. I feel very fortunate for having encountered extraordinary colleagues that have helped me along the way. David was my mentor at the very beginning. Hendrik, Sebastian, and Hans were the first to give me some hints about the Ph.D. life. Additionally, I would like to thank the people that have made my everyday at the Max Planck Institute for Physics a very joyful experience: Javi, Marcel, David, Antonio, Irene, Rasmus, Jayden, Alexandra, Frank, Stephan, Henning, Viktor, Rosita, Monika, Annette, Florian, Edoardo, Max, Cyril, and to the triple A: Alexander Kartavtsev, Alexander Merle, and Alexander Miller. I would like to separately thank Tanja and Max, my office mates for the last two years. During our countless hours together they have always been extremely helpful and caring. A special mention must be done to Sovan Chakraborty, with whom I have spent many long evenings, and from whom I have learned a lot, both as a physicist and as a human being.

Ich möchte Karoline Dammel von ganzem Herzen danken. Ihre endlose Geduld, ihre fröhliche Art und ihre immer gute Stimmung machen mich jeden Tag glücklich, und haben mich durch schwierige Momente getragen. Dafür bin ich ihr unendlich dankbar. *Gracias.* Ich bin auch Kurt und Else Dammel sehr dankbar dafür, dass sie mich so herzlich in die Dammel Familie aufgenommen haben. Dadurch ist Nauheim in den letzten zwei Jahren wie ein zweites Zuhause für mich geworden. Ein besonderes Dankeschön geht an Hilde Dammel, deren Herzlichkeit und Kochkünste mein Leben bereichern. Darüber hinaus,

möchte ich der gesamten Familie Dammel für die schöne gemeinsame Zeit danken. Meinen Freunden in Wiesbaden - Monie, Andreas, Ausi, Nico und Caro - möchte ich für die entspannten Urlaube danken.

Desde luego, no puede faltar en mis agradecimientos lo más importante que tengo en mi vida: mi familia. Sin mis padres, José y Gracia, y mis hermanos, Borja y Guillermo, yo no estaría hoy donde estoy. Siempre me han apoyado incondicionalmente y siempre he sentido su afecto y cariño. Sin lugar a dudas, de ellos he heredado las pocas virtudes que pueda tener. I would also like to thank Christine Chang for being the best host one could desire and for making all my holidays with her unforgettable.

A mis tíos y primos les estoy también muy agradecido, ya que cada vez que vuelvo a España me hacen sentir como en casa. A pesar de que son muchos, dado que una tesis doctoral se escribe solo una vez en la vida, voy a mencionar todos sus nombres: Gonzalo y Belén, junto con mis primos Íñigo, Silvia y Yago. También mi tía Beatriz y sus tres hijos: Sofía, Carlos y Gabriela, así como a mi tío Juanjo. Mi tío Eduardo y mi tía Isabel, a los que les estoy muy agradecido por haberme enseñado a esquiar, y mis primas Patricia y Carlota. Por supuesto, no puedo dejar fuera a mi tía la Bella, con Edu y Ainhoa, además de mi tío Aurelio, que nos dejó hace dos años, pero que sigue presente en mi memoria. También quisiera dar las gracias a la otra parte de la familia. Mi tía Eloisa junto con mis *primos de Zumosol* Daniel y Jorge. También a mi tío Carlos, que siempre consigue arrancar una sonrisa a los demás, y a mi tía Teresa.

Me gustaría también dar las gracias a aquellos amigos que me llevan aguantando desde que estábamos en el instituto: Rubén y Vero, Joaquín y Carmen, Juanjo y María, Alvaro y Maite, y finalmente, Juan Diego y Amelia. A Juan Diego le dedico un agradecimiento especial por aguantarme (junto con el bueno de Sergio) durante el verano del año 2013. Por otra parte, me gustaría dar las gracias a esos miembros de la RSA que siguen sacando tiempo para verme en mis visitas: Eduardo, Pablo, Roberto y Miguel, así como a Iñigo Sagan.

Antes de meterme en el mundo de la astrofísica, pasé tres años de mi vida en la Escuela Técnica Superior de Ingenieros de telecomunicación de la UPM. A pesar de que la vida me ha llevado finalmente por otro derroteros, de aquella experiencia me han quedado algunos de los mejores amigos que he tenido la suerte de conocer. Estos no son otros que Sergio (y por supuesto, Ana), Nicolás, Jorge, Antonio, Miguel Ángel y Dieguito. También han sido muy importantes Javier, Iker, Víctor, Juan Luis, Jaime, Fernando Pipa, Pablo y Fernan. ¡Gracias, amigos!

Cómo no, me gustaría dar las gracias a mi amigo David y a su novia Cristina, que junto con la pequeña Vega, siempre tienen un ratito que dedicarme cuando visito la patria. Del mismo modo, quisiera dar las gracias a la persona que me acompaña desde que tengo el uso de razón, Javier, así cómo al pequeño León, a la encantadora Claudia y al recién llegado Mateo (o Pablo

o Romo).

Mención especial requieren mis apoyos morales en el exilio, ordenados cronológicamente por su orden de entrada en mi pequeño mundo. En primer lugar Nicolás, que desde que puse pie en Alemania, ha sido una persona con la que siempre he podido contar, siempre dispuesto a venir al rescate cuando más lo he necesitado. Marc, con quién he pasado más horas de las que puedo recordar, que hace de cada fin de semana una experiencia especial, además de estar siempre disponible cuando se le necesita. Mario, en el que muchas veces me veo reflejado, que me acompaña tanto en la mas extravagante de las aventuras como en los días más grises. També vull agraïr a l'Ana la seva paciència i els seus consells. Por supuesto, Hugo, un madrileño de los que no quedan, al que se le echa mucho de menos desde su regreso a la patria.

Obwohl München circa zweitausend Kilometer von meiner Heimat entfernt ist, habe ich mich dank meiner Münchner Freunde - Bernie, Selecta, Mario, Kathrin, Marc und Hilke, Marco, Beni und Max - im Laufe der letzten drei Jahre sehr wohl gefühlt.

Ich möchte auch Christof Massner herzlich danken. Einen guten Freund wie ihn findet man selten im Leben, und ich bin ihm für unsere stundenlangen Gespräche sehr dankbar. També m'agradaria donar les gràcies a la Mariona per aquests anys d'amistat. Auch danke ich Freddy und Mira, die ein Teil meiner deutschen Familie geworden sind. I would also like to thank Ahmed, with whom I enjoyed two wonderful years of daily coexistence, and whose hospitality in his homeland I will never forget.

I am also very thankful to my friends overseas: Kuni, Gonzalo, Jon, Andy, Jaime and Jamie. They make my visits truly enjoyable, and is it always difficult to come back to the old continent.

To each and everyone of them goes my sincerest gratitude. *Gracias.*

Por último, quisiera recordar a mi abuela, Gracia Blanco Caballero, que falleció pocos meses antes de que acabara esta tesis, a la que echo mucho de menos.

Munich, 19th May 2017.